Improving Parameterization of Scalar Transport through Vegetation in a Coupled Ecosystem-Atmosphere Model

By

Percy Anne Link

B.A. Cultural and Social Anthropology, 2005
Stanford University

Submitted to the Department of Civil and Environmental Engineering in Partial Fulfillment of the Requirements of the Degree of

Master of Engineering
in Civil and Environmental Engineering
at the

MASSACHUSETTS INSTITUTE OF TECHNOLOGY

June 2008

Signature of Author _____

Percy Anne Link
Department of Civil and Environmental Engineering
May 14, 2008

Certified By _____

Peter Shanahan
Senior Lecturer of Civil and Environmental Engineering
Thesis Supervisor

Certified By _____

Rafael Bras
Professor of Civil and Environmental Engineering
Thesis Supervisor

Accepted By _____

Daniele Veneziano
Chairman, Departmental Committee for Graduate Students

Improving Parameterization of Scalar Transport through Vegetation in a Coupled Ecosystem-Atmosphere Model

by
Percy Anne Link

Submitted to the Department of Civil and Environmental Engineering
on May 16, 2008
in Partial Fulfillment of the Requirements of the Degree of
Master of Engineering in Civil and Environmental Engineering

Abstract

Several regional-scale ecosystem models currently parameterize subcanopy scalar transport using a rough-wall boundary eddy diffusivity formulation. This formulation predicts unreasonably high soil evaporation beneath tall, dense forests and low soil evaporation beneath short, sparse grass. This study investigates alternative formulations by reviewing literature on flow and scalar transport in canopies, taking field measurements of subcanopy latent heat flux, and testing alternative model formulations in constrained numerical experiments. A field campaign was conducted in a dense rainforest in Luquillo National Forest, Puerto Rico, to measure wind and fluxes with eddy covariance devices. Wind velocities and fluxes of latent heat, sensible heat, and momentum were found to be much smaller below the canopy than above it. Modeling experiments tested a mixing-layer-based formulation of eddy diffusivity and a soil evaporation cutoff based on vortex penetration depth. The vortex penetration cutoff was found to be the most physically accurate and computationally simple option, and this study recommends that ecosystem and land-surface models adopt this formulation for subcanopy scalar transport.

Thesis Supervisor: Peter Shanahan
Title: Senior Lecturer of Civil and Environmental Engineering

Acknowledgements

I owe a huge debt of gratitude to Ryan Knox, my research partner. He has tutored me in everything from coding to meteorology to stripping wires, and he has contributed a tremendous amount of time and effort to this project. It was a pleasure to spend a week in the Puerto Rican jungle with him, and without his trouble-shooting skill, electronic expertise and hauling-fifty-pound-batteries-up-a-muddy-slope prowess, the fieldwork could never have happened. He is an enthusiastic and encouraging mentor, and I could not have asked for a better partner in this project.

I am grateful to my thesis advisors, Pete Shanahan and Rafael Bras. Pete has carefully edited many drafts of this document, and his advice and guidance has made this work much stronger. Rafael welcomed me into his research group and supported me in my pursuit of a thesis topic that interested me. I thank them both for challenging me to achieve new things.

Gaby Katul, of Duke University, provided us with invaluable support for our fieldwork. I also thank Kim Novick and Mario Siqueira, members of the Katul research group, for sharing their expertise with us. The generosity of the Katul group made the fieldwork portion of this project possible.

I am grateful to Heidi Nepf for insightful advice on both theoretical and experimental questions.

Fred Scatena, of the University of Pennsylvania and the USDA Forest Service, provided support both in preparation for and during fieldwork, and he gladly answered my seemingly endless follow-up questions. I also thank Carlos Estrada, also of the USDA Forest Service, for help while we were in the field.

Steve Rudolph, technical instructor in the Civil and Environmental Engineering Department at MIT, almost single-handedly designed and built the booms to affix the eddy covariance devices to the tower in the field, with only minimally competent assistance from Ryan and me. I am grateful to him for his patience and generosity.

To my family at home:

Thank you, Mom, Dad, Maggie and Josie, for being my foundation. Thank you for supporting me while I go on my journeys and for welcoming me back when I return home. Everything I have, I owe to you.

To my family in Cambridge:

Our friendship has enriched my life and carried me through this year. Thank you for keeping me on track when I needed it and for distracting me when I needed it. Thank you, Kristin and Kim, for being my home here, and thank you, Kat, for being my buddy on so many levels.

Table of Contents

List of Figures

Chapter 1:

Introduction

Deforestation in the Amazon basin affects not only the biodiversity of the region, but also the fluxes of energy, moisture and momentum at the surface. As such, deforestation has the potential to change the climate on a regional and even global scale. A dynamic equilibrium exists between vegetation and climate, and work by researchers at MIT (e.g. Wang et al. 2000, Chagnon et al. 2004, Chagnon and Bras 2005) and others has established a correlation between deforestation and the occurrence of shallow clouds in the Amazon. Researchers at MIT and Harvard are also developing a coupled biosphere-atmosphere model, called the Ecosystem Demography – Brazilian Regional Atmospheric Modeling System (ED-BRAMS), which simulates the interdependent changes in vegetation and climate associated with deforestation. This model will be used to explore the physical reasons for the observed correlation between deforestation and shallow clouds and to make predictions of future deforestation-related changes in climate.

In its current form, however, the model inaccurately parameterizes flow through vegetation and the resulting transport of momentum and scalars at the land surface. In particular, the model currently predicts unrealistically high rates of soil evaporation below the tall, dense rainforest canopy and relatively lower rates of soil evaporation from short, sparse pasture. This high rate of soil evaporation suppresses transpiration by damping the vapor pressure deficit. Because much of the climatic impact of vegetation change depends on the transpiration and energy-balance characteristics of different types of vegetation, this inaccurate representation of evaporation-transpiration partitioning undermines the model's ability to predict ecosystem-climate interactions.

This study reviews empirical and theoretical literature on transport of momentum and scalars through canopies in general, with special attention to the case of subcanopy evaporation. It then describes a field study conducted with eddy

covariance devices to quantify momentum and scalar fluxes in a dense rainforest canopy in Puerto Rico. The results of this experiment inform a discussion of various parameterizations of canopy flow and transport, enabling us to make recommendations for improvement of evapotranspiration parameterization in the ED-BRAMS model.

Chapter 2:

Land-Atmosphere Interactions in the Amazon Basin

Previous work has investigated the complex relationships between deforestation, the hydrologic cycle, and climate. This chapter discusses the hydrology of the Amazon Basin and characteristics of deforestation there. It then reviews theoretical and experimental work on land-atmosphere interactions in the Amazon, including the development of a coupled ecosystem-atmosphere model. This model's formulation of subcanopy scalar transport is described, and problems with this formulation are outlined.

2.1 Hydrology of the Amazon Basin

The Amazon Basin is the largest source of freshwater runoff on earth and contains 15-20% of the world's river flow (Chagnon & Bras 2005). As such, it has a significant impact on the global hydrologic cycle. Intense seasonal rain and warm temperatures characterize the climate of the Amazon. The rainy season in the Amazon extends from December to April, while the dry season lasts from May to August, and the break period lasts from September to November, during which synoptic forcings are weak relative to those in the rainy and dry seasons (Wang et al. 2000). Large areas of tropical South America receive annual precipitation of 3000 mm or more (Nobre et al. 1991), and between 25 and 35 percent of precipitation in the Amazon basin comes from local evapotranspiration (Eltahir & Bras 1994a).

2.2 Characteristics of Deforestation

Over the past 50 years, land in the Amazon has been converted from native forest to pasture and cropland at a rapid rate. The Brazilian government estimated in 2001 that 15 percent of the Amazon's surface area had been deforested (INPE 2003), and Achard et al. (2002) found that an additional 1.3×10^4 km^2/yr are

deforested for agricultural use. The deforestation follows roads that give access to new parts of the forest, and the result is that deforestation occurs in a fishbone pattern, shown in Figure 2-1, on a spatial scale of tens of kilometers.

Deforestation brings changes in important ecological and physical characteristics of the land surface. Native forest in the Amazon basin consists of dense evergreen vegetation with a canopy reaching approximately 40 meters and a thick understory (Nobre et al. 1991). Pasture, in contrast, consists overwhelmingly of grass and has "higher albedo, lower surface roughness length, higher stomatal resistance, [and] a shallower and sparser root system" (Shukla et al. 1990). Conversion of native forest to pasture also causes changes in soil properties, such as a decrease in hydraulic conductivity and water storage capacity available for transpiration (Shukla et al. 1990).

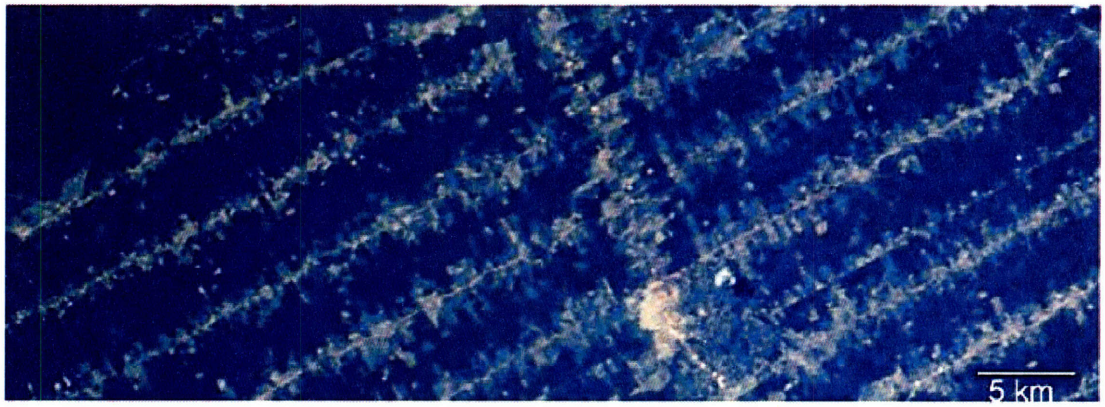

Figure 2-1: Fishbone pattern of deforestation in Rondônia, Brazil. Picture taken from the International Space Station in June 1985; ref# STS51G-34-0060.

2.3 Previous Work Relating Deforestation to Climate/Weather Change

Many studies have examined the impact of large-scale deforestation on global climate using model simulations, and the results indicate that such deforestation would decrease both evaporation and precipitation in the Amazon basin (e.g., Eltahir & Bras 1993, Werth & Avissar 2002). Studies on regional scale deforestation (~250 km) found decreased net surface radiation, evaporation and rainfall, and increased surface temperature (Eltahir & Bras 1994b).

However, deforestation is occurring not on such large scales, but rather on the scale of tens of kilometers, in the fishbone pattern described above. Several theoretical studies have examined the effects of these smaller-scale (tens of km) land surface heterogeneities on atmospheric circulations. For instance, Wang et al. (2000) found that mesoscale circulations induced by land surface heterogeneities are suppressed in stable atmospheric conditions and by larger synoptic systems, but can contribute to triggering moist convection in conditionally unstable atmospheric conditions with weak synoptic forcing. It is also known that differences in land surface heating and moisture between differently vegetated areas can lead to convection (e.g. Wang et al. 2000, Weaver & Avissar 2001).

There is also significant empirical evidence for a correlation between deforestation and local climate change in the Amazon. Chagnon et al. (2004) found a statistically significant increase in shallow cumulus clouds over deforested areas. Figure 2-2, which compares the spatial pattern of deforestation in Rondonia, Brazil, to a computed cloud density index, shows this relationship between deforestation and frequency of shallow clouds. Additionally, Chagnon and Bras (2005) found significantly more rainfall events over deforested areas.

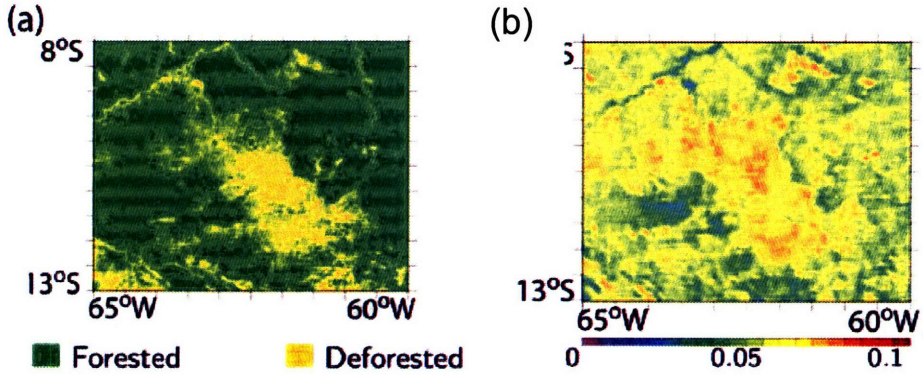

Figure 2-2: (a) Forested and deforested areas in Rondonia, Brazil. (b) Incidence of shallow clouds over the same location (scale reflects fractional cloud cover). (from Chagnon et al. 2004)

2.4 Theoretical Explanation of Observed Differences

Vegetation and climate exist in a dynamic equilibrium, and major perturbations in one can cause changes in the other. The land surface controls fluxes of energy and mass (such as carbon and water) between the land, biosphere and atmosphere, and vegetation greatly influences these fluxes.

Heat energy acts as fuel for convection, in which air and moisture are transported from the lower to the upper regions of the atmospheric boundary layer. This heat energy comes from solar radiation, which the land surface absorbs and releases as either sensible heat or water vapor, known as latent heat. When such heat makes air warmer than the air around it, the air accelerates upward and can form a cloud (Pielke 2001).

The land surface controls energy exchanges that determine the possibility of convection, and deforestation causes important changes in the land surface. Chagnon et al. (2004) note that deforestation causes increased surface albedo, decreased root-zone depth, decreased surface roughness and decreased leaf-area index. These changes affect the amount of energy available for sensible and latent heat, the potential for transpiration, and the characteristics of turbulent flows that transport sensible and latent heat from the land surface to the atmosphere.

At equilibrium (where no accumulation occurs), the energy and moisture budgets at the surface are:

$$R_N = Q_G + H + \lambda(E + T) \tag{2-1}$$

and

$$P = E + T + RO + I \tag{2-2}$$

where R_N is net radiation, Q_G is heat flux into the ground, H is sensible heat, $\lambda(E + T)$ is latent heat (where λ is the latent heat of vaporization), P is precipitation, E is evaporation, T is transpiration, RO is runoff, and I is infiltration (Pielke 2001).

Deforestation influences many of the terms in the energy and moisture budgets. For instance, the higher albedo associated with pasture decreases R_N, so less energy is available to be partitioned among sensible, latent, and ground heat

fluxes. Also, clear-cutting of native forest can increase runoff and thus decrease the amount of water stored in the soil and available for evaporation and transpiration (Pielke 2001). Moreover, the decreased leaf area index and root zone depth associated with deforestation significantly reduce transpiration, so that, assuming no ponded water or saturation at the surface, a larger proportion of the net radiative energy is released as sensible heat rather than latent heat.

The combined effect of these changes is difficult to predict, because they are related in a nonlinear fashion. Some meteorological terms describing energetic processes in convection help to illustrate these complex interactions. The level of free convection (LFC) is the altitude in the atmosphere at which a parcel will begin to rise under its own buoyancy; in order to reach this point, though, parcels must be lifted to the LFC. Convective inhibition (CIN) is a measure of the energetic barrier to lifting a parcel to the LFC, and convective available potential energy (CAPE) is a measure of the amount of energy available for convection above the LFC once a parcel has been lifted there (Stull 2000). While forested areas have greater CAPE than deforested areas due to greater latent heat flux, they have less of a triggering mechanism, in the form of sensible heat, to overcome the CIN and lift the air to the LFC (Pielke 2001).

Recent research by Jingfeng Wang and colleagues (unpublished; Wang, personal communication) found that the atmosphere over forested areas was more unstable and had more CAPE, making possible occasional deep convection when a triggering mechanism overcame the CIN. In contrast, they found that the hotter but drier air over deforested areas was weaker energetically, so that while it could more easily overcome the CIN due to its initial buoyancy but did not have enough energy to engage in deep convections. Thus, clouds over deforested areas were shallow.

2.5 Coupled Ecosystem-Atmosphere Model

In order to investigate the physical mechanisms behind the observed correlation between deforestation and changes in regional climate, a team at MIT

and Harvard is developing a model that simulates the interdependent changes in vegetation and climate in the Amazon basin.

The ED-BRAMS model links a model of the Brazilian atmosphere (BRAMS) to a model of the terrestrial ecosystem (ED). This coupling simulates the coevolution of climate and ecosystems through physical processes. Brazilian scientists adapted BRAMS from the more general Regional Atmospheric Modeling System (RAMS) developed by Pielke and others from Colorado State University (Pielke et al. 1992). BRAMS and RAMS are limited-area models that simulate atmospheric motions and can also incorporate "parameterizations for turbulent diffusion, solar and terrestrial radiation, moist processes including the formation and interaction of clouds and precipitating liquid and ice hydrometeors, sensible and latent heat exchange between the atmosphere, ... and cumulus convection" (RAMS 2007). The grid cells of the coupled model can range in scale from less than 4 km to about 100 km. BRAMS differs from current versions of RAMS mainly in the turbulence closure scheme and its use of the Grell convection scheme (Ryan Knox, personal communication). Additionally, it has been tested and optimized with the goal of simulating the tropical climate and is thus particularly suited to the task of modeling the Amazon. (Marcos Longo, personal communication).

The Ecosystem Demography model, or ED, was developed by the Paul Moorcroft group at Harvard University (Moorcroft et al. 2001). ED uses a size- and age-structured approximation to simulate fine-scale spatial heterogeneity within ecosystems without modeling each individual plant. The model differentiates vegetation types within each grid cell by allocating a patch, or fraction, of the cell area to each type of vegetation present. Updates to the model have enabled it to close the land surface energy budget and thus achieve physical consistency (Medvigy 2006). ED receives downward radiation fluxes, as well as meteorological state variables for a reference height of ~90 m, from the atmospheric model. ED then returns the upward fluxes of energy, mass, and momentum to the atmospheric model, in such a way that total energy and mass are conserved.

2.6 Current Model Formulation of Subcanopy Soil Evaporation

The goal of the ED-BRAMS modeling project is to represent the highly complex and nonlinear feedbacks between vegetation and climate and to predict the effects of perturbations in either ecosystem or climate on the other. Correctly representing the exchanges of energy, momentum, and mass at the interface between the ecosystem and the atmosphere is central to this goal.

The formulation of evapotranspiration (ET) in the ED model significantly influences the overall modeled mass and energy balance between land and atmosphere. Currently, ED partitions ET into evaporation from free water surfaces on wet leaves (interception loss), evaporation from the soil, and transpiration from stomata of dry leaves. A resistance is calculated for each process of water vapor transfer into the canopy air space, and another resistance is calculated for the transfer from the canopy air space to the surface layer above. In general, evaporative flux, E (kg/m^{2}s), is related to resistance as

$$E = \rho_{atm} \frac{(q_{atm} - q_s)}{r_{aw}} \tag{2-3}$$

where ρ_{atm} is the density of air (in kg/m^3) which varies with temperature and moisture content, q_{atm} is specific humidity (in kg water/kg air) at the reference height (z_{atm}), q_s is the specific humidity at $z_o + d$ (roughness length plus displacement height) and r_{aw} is the aerodynamic resistance to water vapor transfer between the atmosphere at height z_{atm} and the canopy airspace at $z_o + d$. Equation 2-3 can be modified to describe water vapor flux between any two levels by substituting the specific humidity of each level in the numerator and the aerodynamic resistance to transfer between the levels in the denominator. Figure 2-3 shows the location of these heights in the canopy. In the figure, the subscript w indicates the roughness length for water vapor.

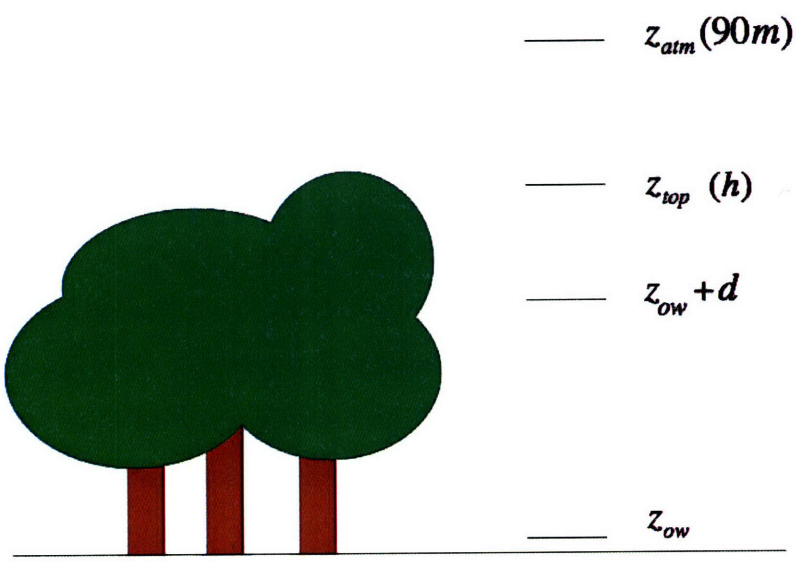

Figure 2-3: Definition figure for heights used in resistance formulation.

In Figure 2-4, the top resistance diagram represents water vapor transfer for unvegetated surfaces, and the bottom diagram represents water vapor transfer for vegetated surfaces. For the vegetated surfaces, the middle position ($z_{ow}+d$) represents the canopy airspace, and vapor is transferred from the soil surface (z_{ow}) and the leaves to the canopy airspace and from there to the atmosphere (z_{atm}).

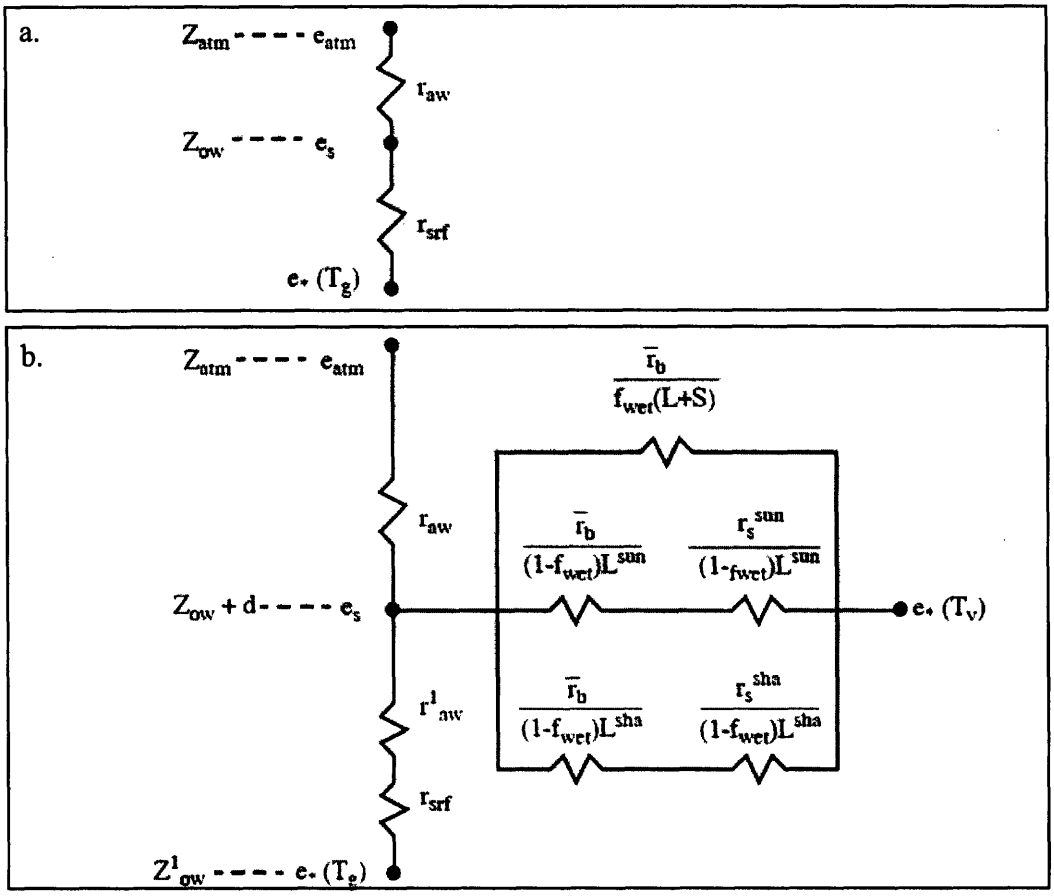

Figure 2-4: Diagram of resistances to transfer of water vapor between positions in the canopy for (a) unvegetated and (b) vegetated surfaces. From Bonan (1996).

The resistances are derived by approximating the turbulent flow over the land surface as a rough wall boundary layer and applying the Monin-Obukhov Similarity Theory, or MOST (Bonan 1996). Moisture and heat fluxes occur both between the ground and the canopy airspace and between the vegetation and the canopy airspace; the canopy airspace then exchanges heat and moisture with the atmosphere above. The formulation of these resistances is the same in the ED and LEAF models as it is in a land surface model developed by the National Center for Atmospheric Research (Ryan Knox, personal communication). The derivation of these resistances in NCAR LSM users' manual (Bonan 1996) is summarized here.

Following MOST, these models define the vertical gradients in momentum, heat and moisture as unique functions of a non-dimensional length scale $\zeta = \frac{z-d}{L}$ such that

$$\frac{k(z-d)}{u_*}\frac{\partial|\vec{u}|}{\partial z} = \Phi_m(\zeta) \tag{2-4}$$

$$\frac{k(z-d)}{\theta_*}\frac{\partial\theta}{\partial z} = \Phi_h(\zeta) \tag{2-5}$$

$$\frac{k(z-d)}{q_*}\frac{\partial q}{\partial z} = \Phi_w(\zeta) \tag{2-6}$$

where $\vec{u} = \sqrt{u^2 + v^2}$, z is height, d is displacement height, k is the von Karman constant, and L is the Monin-Obukhov length scale.

The velocity, temperature, and moisture scales, u_*, θ_*, and q_*, are defined as

$$u_* u_* = \sqrt{(\overline{u'w'})^2 + (\overline{v'w'})^2} = \frac{|\tau|}{\rho_{atm}} \tag{2-7}$$

$$\theta_* u_* = -\overline{\theta' w'} = -\frac{H}{\rho_{atm} C_p} \tag{2-8}$$

$$q_* u_* = -\overline{q' w'} = -\frac{E}{\rho_{atm}} \tag{2-9}$$

where τ is the shear stress (kg/m s^2), H is the sensible heat flux (W/m^2), and C_p is the heat capacity of air (J/kg K).

The Monin-Obukhov length, L, is

$$L = \frac{-u_*^3}{k\left(\frac{g}{T_{v,atm}}\right)\left(\frac{H_v}{\rho_{atm} C_p}\right)} \tag{2-10}$$

where g is gravitational acceleration (m/s^2), $T_{v,atm}$ is the virtual atmospheric temperature (K), which depends on temperature and specific humidity, and H_v is the virtual sensible heat flux (W/m^2), which depends on the virtual temperature. (See Stull (2000) for definitions of virtual temperature and heat flux).

The resistance to transfer from the canopy airspace at $z_o + d$ to the atmospheric level at z_{atm} is then

$$r_{am} = \frac{1}{ku_*}\left[\ln\left(\frac{z_{atm}-d}{z_{0m}}\right) - \psi_m(\zeta)\right]$$

$$= \frac{1}{k^2|u|_{atm}}\left[\ln\left(\frac{z_{atm}-d}{z_{0m}}\right) - \psi_m(\zeta)\right]^2 \qquad (2\text{-}11)$$

$$r_{ah} = \frac{1}{ku_*}\left[\ln\left(\frac{z_{atm}-d}{z_{0h}}\right) - \psi_h(\zeta)\right]$$

$$= \frac{1}{k^2|u|_{atm}}\left[\ln\left(\frac{z_{atm}-d}{z_{0m}}\right) - \psi_m(\zeta)\right]\left[\ln\left(\frac{z_{atm}-d}{z_{0h}}\right) - \psi_h(\zeta)\right] \qquad (2\text{-}12)$$

$$r_{aw} = \frac{1}{ku_*}\left[\ln\left(\frac{z_{atm}-d}{z_{0w}}\right) - \psi_w(\zeta)\right]$$

$$= \frac{1}{k^2|u|_{atm}}\left[\ln\left(\frac{z_{atm}-d}{z_{0m}}\right) - \psi_m(\zeta)\right]\left[\ln\left(\frac{z_{atm}-d}{z_{0w}}\right) - \psi_w(\zeta)\right] \qquad (2\text{-}13)$$

where the subscripts *m*, *h*, and *w* refer to momentum, heat, and water vapor, respectively.

Water vapor flux to the canopy airspace, *E*, comes from both evaporation from the ground and transpiration from the vegetation, i.e. $E = E_v + E_g$, where E_v is transpiration and E_g is ground evaporation. Transpiration is calculated as

$$E_v = -\rho_{atm}[q_s - q_*(T_v)]\left[f_{wet}\left(\frac{L+S}{\bar{r}_b}\right) + (1-f_{wet})\left(\frac{L^{sun}}{\bar{r}_b + r_s^{sun}} + \frac{L^{sha}}{\bar{r}_b + r_s^{sha}}\right)\right] \qquad (2\text{-}14)$$

where $q_*(T_v)$ is the saturated specific humidity (kg/kg) at leaf temperature (T_v (°C)), L^{sun} and L^{sha} are the fractions of leaves that are sunlit and shaded (dimensionless), r_s^{sun} and r_s^{sha} are the sunlit and shaded stomatal resistances (s/m), $\bar{r}_b$ is the leaf boundary layer resistance (s/m), and f_{wet} is the wetted fraction of the canopy. The ground evaporation is

$$E_g = -\rho_{atm} \frac{[q_s - q_*(T_g)]}{r'_{aw} + r_{srf}} \tag{2-15}$$

where $q_*(T_g)$ is the saturated specific humidity (kg/kg) at ground temperature (T_g (°C)), r'_{aw} is the aerodynamic resistance (s/m) between the ground (z_0) and the canopy airspace (z_0+d), and r_{srf} accounts for water vapor transfer from the soil and depends on soil moisture as described in Bonan (1996, p. 59).

Resistance to transfer from ground to canopy airspace equals the integral of the inverse of eddy diffusivity over the height of the canopy:

$$r'_{aw} = \int_{z_0}^{z_0+d} \frac{dz}{K_w(z)} \tag{2-16}$$

Above the canopy, eddy diffusivity is assumed to relate linearly to height:

$$K_w(z) = ku_*(z - d - z_{0w})\phi_w^{-1} \tag{2-17}$$

for $z > z_{top}$. Below the canopy, eddy diffusivity is assumed to decay exponentially with depth below the canopy according to an empirical parameter a:

$$K_w(z) = K_w(z_{top})e^{-a(1-z/z_{top})} \tag{2-18}$$

for $z < z_{top}$. Thus,

$$r'_{aw} = \int_{z_{0w}}^{z_{0w}+d} \frac{dz}{K_w(z)} = \frac{z_{top}}{aK_w(z_{top})}\left[e^{a(1-z_{0w}/z_{top})} - e^{a(1-(z_{0w}+d)/z_{top})}\right] \tag{2-19}$$

Currently in the ED model, $a = 2.5$, and $d = 0.63z_{top}$. The linear relationship between d and z_{top} means that $K_w(z_{top})$ grows with increasing canopy height, while the terms in the exponentials are normalized by the canopy height and thus are the same for all canopy heights. Figure 2-5 shows vertical profiles of eddy diffusivity in canopies of different heights, calculated using equations 2-17 and 2-18. The figure demonstrates this formulation's prediction that taller canopies have higher diffusivities at both the canopy top and bottom than do shorter canopies.

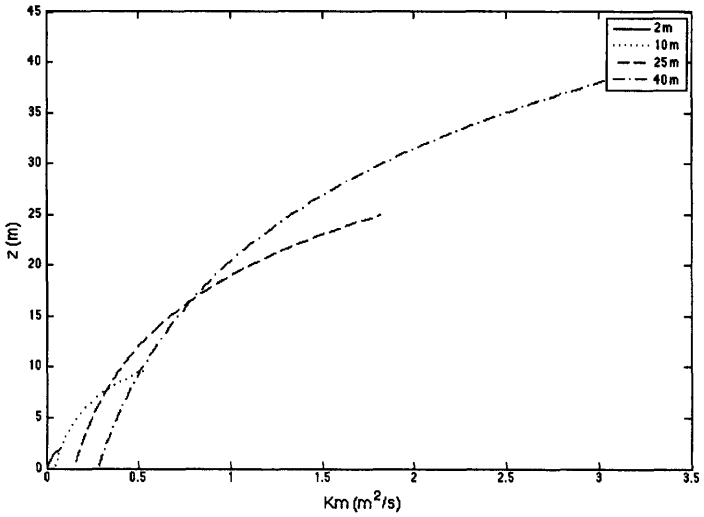

Figure 2-5: The exponential decay of eddy diffusivity in canopies of four different heights (2, 10, 25 and 40 m), calculated using the current ED model formulation.

When integrated over the canopy height (as in Equation 2-19), this formulation of eddy diffusivity gives a resistance that decreases with increasing canopy height. Figure 2-6 shows r'_{aw} versus canopy height using a wind speed of 4 m/s at the 90 m reference height. With this formulation, higher canopies give lower resistances. Figure 2-7 shows the latent heat flux from the soil associated with this resistance; using the resistance formulation given in equation 2-17, soil latent heat flux increases with increasing canopy height.

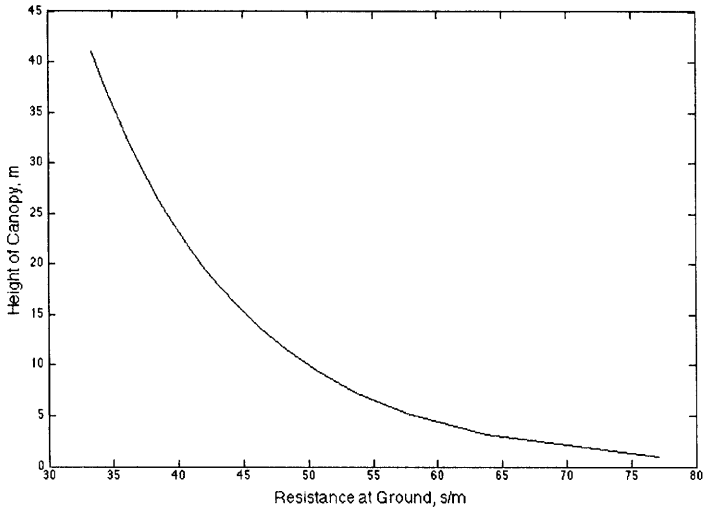

Figure 2-6: In the current ED model formulation of soil evaporation resistance, increasing canopy height gives lower resistance.

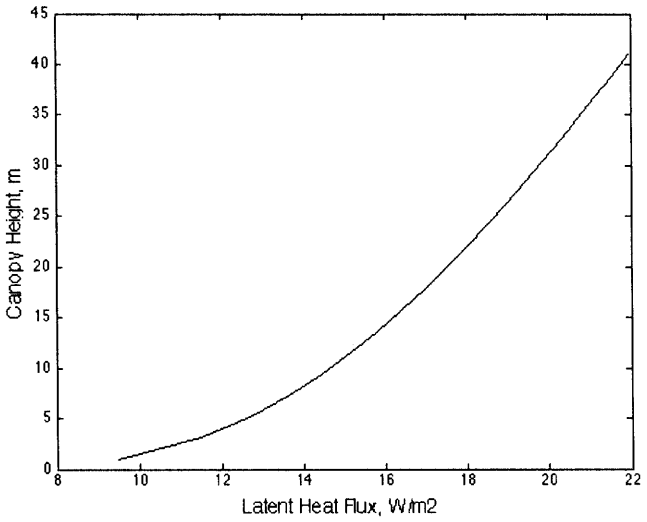

Figure 2-7: Latent heat flux from soil as a function of canopy height, calculated using the current ED model formulation.

With this formulation, the ED model currently predicts a higher ratio of soil evaporation to transpiration from a dense, tall rainforest than from a short, sparse pasture. The following section reviews empirical evidence to the contrary, showing that the ratio of soil evaporation to transpiration is smaller under tall dense forests

than under grass, and indeed that soil evaporation under tall dense forests is negligible.

2.7 Field Observations of Evapotranspiration from Tropical Rainforests

Shuttleworth (1988) conducted a two-year study of the micrometeorology and hydrology of central Amazonia in order to calculate dry canopy evapotranspiration and rainfall interception loss. Shuttleworth's approach was "to synthesize net evaporation loss by measuring and modeling, and then integrating, the rate of water vapor transfer into the atmosphere." The Rutter interception model (Rutter et al. 1975) was modified to include transpiration from a dry canopy, and the Penman-Monteith equation (Monteith 1965) was used to calculate evaporation, with r_s and r_a calibrated with measurements in dry conditions. The Penman-Monteith equation is

$$\lambda E = \frac{\Delta A + \rho c_p D / r_a}{\Delta + c_p (1 + \frac{r_a}{r_s}) / \lambda} \tag{2-20}$$

where A is the energy available for evaporation, D is the specific humidity deficit at reference height, ρ is the density of air, c_p is the specific heat of air at constant pressure, Δ is the mean rate of change of specific humidity with temperature, λ is the latent heat of vaporization of water, r_s is the bulk stomatal resistance, and r_a is the aerodynamic resistance to transfer to a reference height above the canopy.

Shuttleworth uses the Penman-Monteith equation to describe evaporation in two cases: where the canopy is dry, and thus evaporative flux is due solely to transpiration, and where the canopy is partially or fully wet, so that some fraction (or all) of evaporative flux above the canopy comes from evaporation of free water on plant surfaces, a process known as interception loss. Importantly, Shuttleworth ignores evaporation from the soil in his evaporation budget.

In order to account for interception loss, Shuttleworth employs the Rutter model (Rutter et al. 1975), which takes the form

$$\frac{dC}{dt} = P(1 - p - p_t) - (C/S)\lambda E_c - D_r \tag{2-21}$$

where C is actual stored water at a given time, S is the amount of water the canopy can store when completely wetted and allowed to drain, λE_c is evaporation rate from a totally wet canopy, P is the incoming precipitation rate, p is the proportion of rain falling directly to the ground without hitting the canopy, p_t is flow down trunks, and D_r is canopy drainage rate. This model requires parameterization of canopy storage (S) and throughfall (p). Shuttleworth found that the model results for total evaporation were not very sensitive to the values of S, p, and r_a chosen; instead, their values affect the partitioning of the total evaporation between transpiration and interception losses.

Shuttleworth's two years of field data from Amazonia indicate that evaporation is fairly constant at about 110 mm per month, and that it depends mostly on transpiration but also significantly on the interception process. On average, 25% of total evaporation came from interception loss (with the rest presumed to come from transpiration), but "this changed from over 50% in wet months to less than 10% in dry months." (Shuttleworth 1988, p. 337) Overall, about 50% of precipitation on the site returned to the atmosphere as evaporation, and measured evaporation was close to potential evaporation because of enhanced evaporation from interception during periods of wet canopy. Again, it is important to note that this study assumed from the outset that evaporation from the soil and litter layer under a dense tropical rainforest was negligible. Thus, it provides no empirical evidence of soil evaporation rates, but it does demonstrate the standard assumption in rainforest hydrology that soil evaporation does not contribute significantly to the overall evapotranspiration dynamics.

In a more general overview, Roberts and colleagues (2005) conducted an extensive review of literature on evaporation from lowland tropical rainforests. Like Shuttleworth, Roberts et al. assume that only transpiration and interception loss contribute significantly to evapotranspiration from these forests; thus, they implicitly suggest that soil evaporation does not play a significant role in the evapotranspiration dynamics.

The review examines evaporation data for 22 sites in Latin America, Africa, and South-East Asia and finds that annual evaporation was generally 1200-1700 mm/yr. Potential evaporation at the same sites, determined by available energy, is estimated at 1500-1550 mm/yr. Transpiration ranged from 885 to 1285 mm/yr with an average of 1045 mm/yr, and at many sites it accounted for more than half of the annual rainfall and consumed over 70% of the available energy.

Roberts et al. (2005) discuss factors that control evaporation and transpiration. In order for evaporation to occur, there must be an input of energy, a vapor pressure deficit between the atmosphere and the source, and transfer through conductances associated with stomata, leaf boundary layers and the canopy air space (reciprocals of the resistances found in equation 2-12 and shown in figure 2-5). While the canopy air space conductance controls both transpiration and evaporation from free surfaces, transpiration also depends on stomatal conductance, which in turn depends on external factors such as solar radiation, temperature, air humidity deficit and carbon dioxide concentration. At the rainforest sites studied, stomatal conductance varied in time, peaking in the mid-morning, and in space, peaking at the top of the canopy. Stomatal conductance decreased with increasing vapor pressure deficit. Maximum daily values of stomatal conductance measured at the rainforest sites ranged from 0.32 to 2 mol/m^2s.

In addition to transpiration, interception loss (or evaporation of precipitation from leaf surfaces during and after rain events) plays a major role in the dynamics of evaporation from rainforests. Roberts et al. (2005) note that, in continental rainforests, rainfall generally occurs in short duration, high-intensity storms, so that the percentage of precipitation lost to interception is low. In contrast, in coastal and maritime rainforests, frequent storms of low intensity lead to higher relative loss of precipitation to interception.

Again, as in the Shuttleworth (1988) paper, the studies reviewed by Roberts et al. (2005) assumed that soil evaporation below a tropical rainforest canopy was negligible relative to transpiration and interception losses.

Other experimental methods confirm the assumption by Shuttleworth and Roberts et al. that soil evaporation is unimportant under a dense canopy. Moreira et al. (1997) measured isotope ratios in water vapor over rainforests and pastures in order to determine the relative contributions of soil evaporation and transpiration to total latent heat flux in tropical regions. This method makes use of the isotopic depletion of water vapor from evaporative processes relative to vapor from transpiration. In evaporation from soil or a free surface, heavier isotopes of water are less likely to enter the vapor phase and to diffuse away, so that the vapor has a smaller proportion of heavy isotopes than the source water. In contrast, water in the leaf has the same isotopic composition as water in the soil, and in steady-state transpiration the vapor leaving the leaf has the same composition as well.

Moreira et al. (1997) developed a mixing equation for water vapor in the forest, assuming that the three major sources of vapor were transpiration, evaporation from soil and other free surfaces, and atmospheric vapor. Evaporation from free surfaces was assumed to come entirely from soil, because measurements were collected during the dry season when interception loss could be ignored. Measured ratios were compared to the predicted mixing relationships given by different relative contributions of each source.

Isotopic ratios from rainforest sites were very similar to ratios predicted if transpiration were the only source of water vapor to the forest air. In contrast, measured ratios over grassland indicated that "transpiration contributes little to the ambient vapour at upper elevation in the pasture," (Moreira et al. 1997, p. 448) and soil and atmospheric contributions control the water vapor isotope ratio. While the conclusions of this work were mostly qualitative, they indicate the general trend for transpiration to dominate vapor production in forests and to play a much lesser relative role over grasslands.

Chapter 3:

Background on Canopy Flow and Scalar Transport

The previous chapter outlined the current ED model formulation of flow and transport in the canopy and described the unrealistic results it produces. The current chapter reviews theory of flow through vegetation and surveys models of scalar transport in canopies. An important finding is that, instead of the rough wall boundary layer flow that the current ED model formulation assumes, canopy flow resembles a mixing layer characterized by intermittent, coherent structures of the scale of the canopy height. These coherent structures dominate the transport of momentum and scalars between the canopy and the overlying flow.

Several of the theories of flow and transport discussed here are tested in following chapters as alternative model formulations of scalar transport through vegetation.

3.1 Failure of Eddy Diffusivity (K Theory) in Canopies

In the past twenty years, it has become increasingly clear that gradient-diffusion theory based on the concept of eddy diffusivity, also known as K theory, fails to describe transport of momentum and scalars through canopies accurately. Raupach (1988) provides a convincing argument that K theory is invalid in canopies. Evidence for this problem includes the lack of reproducibility of results for the form of the K(z) profile and its relationship with canopy geometry. Additionally, negative K values (counter-gradient flows) were measured locally within the canopy; such counter-gradient flows contradict the basic assumption of gradient-diffusion theory that the quantity being transported always moves down-gradient. Measurement of turbulence length scales within and above the canopy showed these to be of the order of the canopy height. Thus, "the vertical mixing cannot be considered to be 'fine-grained' with respect to the canopy or to concentration profiles within and just above the canopy" (Raupach 1988, p. 98).

When the mixing length and gradient are of the same scale, as they are in this case, K theory cannot describe vertical transfer. Moreover, from a Lagrangian perspective, dispersion in a horizontal wind increases with distance downwind of the source, and an eddy diffusivity that does not vary with distance from the source cannot describe this phenomenon.

In place of the first-order Eulerian closure of the gradient-diffusion method, Raupach proposes a Lagrangian model to describe scalar transport in the canopy. This type of model assumes "that the transfer of a scalar additive in a turbulent flow is statistically equivalent to the dispersion of an ensemble of marked fluid particles" (Raupach 1988, p. 104). The plume of scalar concentration resulting from each individual source within the canopy (for example, a leaf) is thus determined by the statistics of motion of particles leaving the source, and the plumes due to multiple sources can be superimposed on each other to give the concentration distribution within the canopy.

Using "random-flight" or stochastic theories, which require a numerical solution to a stochastic differential equation, the particle transition probability can be found and thus the concentration distribution given a known source distribution can be derived. In the canopy, however, source strengths often depend on the concentration distribution, so that the equations for source and concentration profiles are coupled. Thus, "the task of a canopy microclimate model is to solve for the coupled $\bar{c}(z)$ and $S(z)$ profiles, given appropriate external conditions, by combining a source-concentration relationship at the individual-leaf level with a description of turbulent transfer through the canopy" (Raupach 1988, p. 114). Raupach (1988) describes a method for solving the coupled physiological source equations and Lagrangian concentration distribution equations.

Raupach's Lagrangian method has several advantages. It resolves aerodynamic resistances at small scales and thus account for differences in diffusivity between small and large scales. It also separates the individual-leaf and turbulent-transfer elements of the coupled source and concentration distribution equations, allowing these processes to be studied independently. Nevertheless, the

Lagrangian method has several major drawbacks for the purpose of regional-scale land surface modeling. It requires turbulence statistics that are not easily derived from meteorological variables received from an atmospheric model, and it involves the numerical solution of stochastic differential equations, which is computationally expensive. As Raupach noted twenty years ago, K theory remained in use because "there was no clear alternative, and there was no direct evidence of its invalidity" (Raupach 1988, p. 97); the lack of a clear alternative, or at least one that is simple enough to use in large-scale modeling, persists today.

Much is understood about flow and transport in vegetation, however, and several types models exist that describe the relationship between flow characteristics, source distribution, and concentration profiles.

3.2 Second-Order Models of Canopy Transport

It is possible to model the vertical profiles of momentum and scalars in the canopy by solving the Eulerian conservation equations for momentum and mass. These equations require parameterized closures; first-order eddy diffusivity closures are computationally simple but, as Raupach (1988) showed, they fail in the canopy environment. On the other hand, second-order Eulerian closures provide more accurate resolution of local gradients, sources, and sinks but are computationally more complex. Second-order approaches can be used to estimate concentrations from a known distribution of sources and sinks. Alternatively, "inverse" second-order approaches can be used to find the distribution of sources and sinks given a measured concentration distribution.

Siqueira et al. (2000) describe an Eulerian model that can be used to estimate sources, sinks and fluxes from concentration distributions (i.e., an inverse model). These models could also be used, in non-inverse form, to predict concentration distribution from known sources, sinks, and fluxes. Siqueira et al.'s Eulerian model is a second-order differential equation representing the time- and horizontally-averaged equation for the vertical scalar flux budget. It employs a closure approximation for the unknown terms in the flux budget (the terms representing

"transport of the turbulent flux" and "destruction by the pressure-scalar interaction" (Siqueira et al. 2000, p. 29,477)). This equation can be solved numerically for the vertical flux and then differentiated with respect to z to find the vertical profile of sources and sinks.

Second-order closure models can also be used in a non-inverse way to estimate concentration profiles from known sources and sinks. Many studies (e.g., Wilson 1988, Katul 1998) describe second-order closure models for momentum fluxes in canopies that estimate the distribution of momentum (velocity profiles) from known sources (above-canopy wind) and sinks (drag), and these theoretically could be adapted to model scalar fluxes in the canopy. However, this is not a feasible approach for modeling latent heat flux in the ED model because solving second-order closures requires iterative numerical methods, which are too computationally demanding over a large spatial grid and many time steps.

3.3 Mixing Layer Analogy for Canopy Turbulence

Several decades ago, flow over a vegetated surface was understood as a rough-wall boundary layer, and the current ED model evaporation formulation (Section 2.6) is based on this theory. However, theory and evidence from the last twenty years depicts the canopy as a plane mixing layer, characterized by an inflected mean velocity profile and coherent, intermittent turbulent structures of the scale of the whole canopy. Finnigan (2000) reviewed this recent literature on the theory and observations of turbulence in plant canopies.

The layer well above the canopy is a constant stress layer, and u_* is measured there; within the canopy, the stress, $-\overline{u'w'}$, decays quickly as aerodynamic drag on the vegetation absorbs momentum. Transport of momentum and scalars at the canopy top ($h < z \leq 3h$, where h is canopy height) is enhanced relative to the standard surface layer above. In this region, the eddy diffusivity for momentum is increased by a factor of 1.1 to 1.5, while the eddy diffusivity for scalars is increased by a factor of 2 to 3.

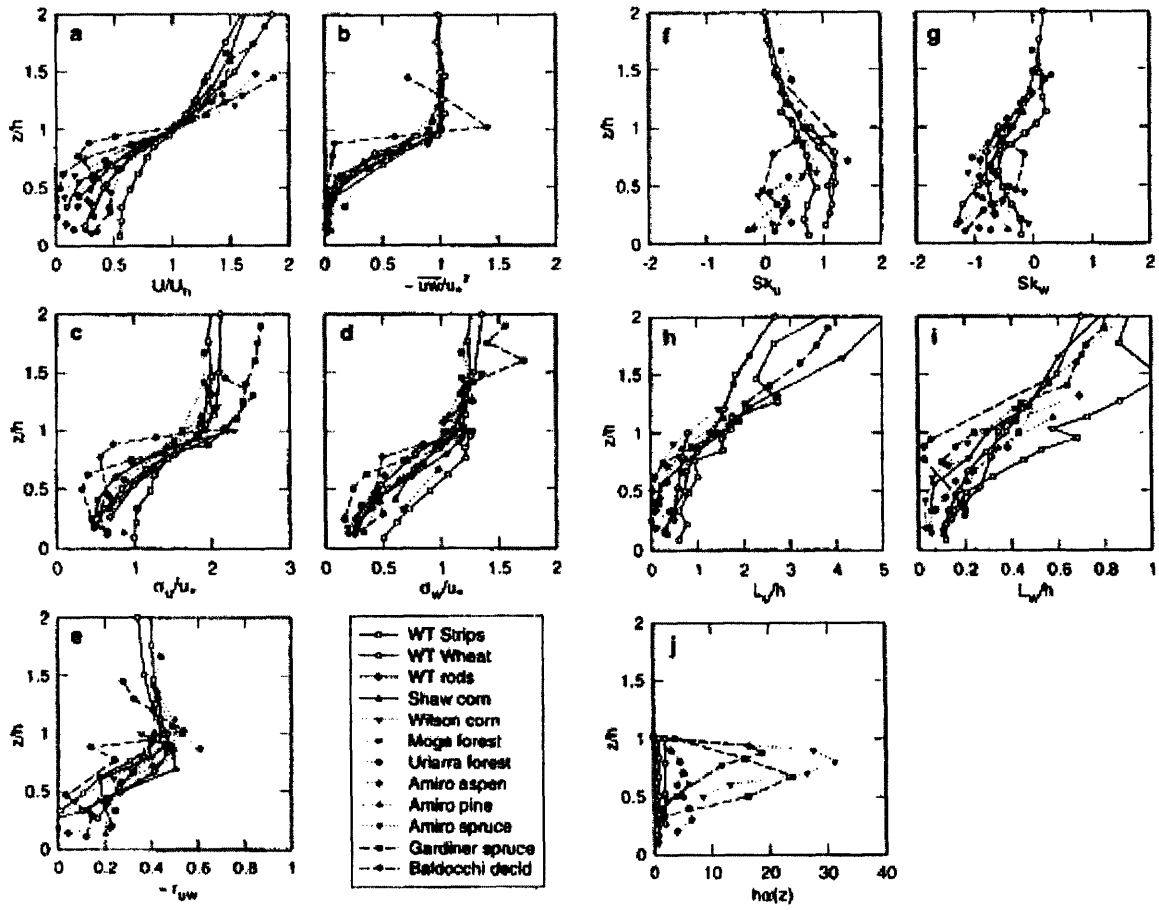

Figure 3-1: Profiles of turbulence statistics normalized with canopy height, from Finnigan 2000, Figure 1. (a) Mean velocity normalized by velocity at canopy top; (b) Momentum flux normalized by friction velocity; (c) Standard deviation of horizontal velocity; (d) Standard deviation of vertical velocity; (e) $-r_{uw} = -\overline{u'w'}/\sigma_u\sigma_w$, correlation coefficient or efficiency of momentum transport; (f) Horizontal velocity skewness; (g) Vertical velocity skewness; (h) Horizontal Eulerian integral length scale; (i) Vertical Eulerian integral length scale; (j) Leaf area density times canopy height.

Figure 3-1, from Finnigan (2000), shows measured profiles of velocity and turbulence statistics from different canopy types. Profiles of mean velocity through the canopy have an inflection point at the canopy top, where the shear is maximal. Above the canopy, the velocity profile approximately follows the logarithmic profile of a standard boundary layer, while within the canopy it is approximately exponential. In the surface layer well above the canopy, shear production and viscous dissipation of turbulent kinetic energy (TKE) are locally balanced; however,

in the canopy, TKE is produced by shear at the canopy top and is transported into the canopy, resulting in a non-local balance.

Canopy flows share several important features with a plane mixing layer and differ significantly from the rough wall boundary layer of the MOST formulation (Section 2.6). Mixing layers and canopy flows both have an inflected mean velocity profile and thus are unstable to perturbations even without viscosity, as opposed to boundary layers, which are only unstable when viscosity is present. The instability leads to the formation of Kelvin-Helmholtz vortices around the inflection point. Thus, mixing layers and canopy flows both have large, coherent vortices that form at the boundary between layers. In both cases, a single length scale and single velocity scale describe the coherent structures. The length scale (L_s) is related to a vorticity thickness (δ_w) in the following way:

$$\delta_w = \frac{\Delta U}{(\partial \bar{u}/\partial z)_{\max}}$$

$$L_s = \frac{\bar{u}(h)}{(\partial \bar{u}/\partial z)_{z=h}} \approx \frac{1}{2}\delta_w = \frac{1}{2}\frac{\Delta U}{(\partial \bar{u}/\partial z)_{\max}} \tag{3-1}$$

where ΔU is the difference in velocity between the two layers (atmospheric surface layer above and canopy below). Experimental evidence reviewed by Finnigan indicates that the length scales of turbulence in the horizontal mean wind direction (L_u) and vertical direction (L_w) are both on the order of the canopy height, h.

$$L_u \cong h; \quad L_w \cong h/3 \tag{3-2}$$

The velocity scale is the friction velocity, u_*, or the mean velocity at canopy top, $\bar{u}(h)$. The turbulent velocity variances peak at the position of maximum shear, which occurs at the inflection point at the canopy top. Finnigan notes that "the mean velocity is a poor estimate of the convection velocity of the eddies that dominate the correlation fields" (Finnigan 2000, p. 533); instead, eddy velocity scales on friction velocity, which depends on the degree of shear.

These coherent, canopy-scale eddies dominate transport of momentum and scalars through the canopy. These eddies appear in measurements as sweeps,

which are "the penetration of the canopy by fast, downward moving gusts" (Finnigan 2000, p. 533). In the canopy mixing layer, sweeps are very intermittent, but each transports a large amount of momentum. In the studies reviewed by Finnigan, 50% of the momentum was transferred in less than 10% of the time, with similar results for scalar transport. Experiments showed that, at least in near-neutral stratification, the same large coherent structures transport both momentum and scalars.

Dissipation of turbulent kinetic energy (TKE) occurs rapidly in the canopy. Aerodynamic drag on the foliage dissipates TKE in part because the vegetation provides many fine-scale shear layers, which dissipate eddies. Additionally, the creation of wakes around plant elements acts as a "spectral shortcut" which transfers energy from large eddies into much smaller eddies in a single step, instead of the many incremental steps of the classic eddy cascade. These smaller eddies are then much closer to the scale of viscous dissipation.

3.4 Depth of Vortex Penetration into Canopy

Unlike in an actual mixing layer, where Kelvin-Helmholtz vortices grow continually downstream, in a canopy shear layer, the vortices reach a fixed scale soon after the canopy's leading edge. Using the principle of conservation of turbulent kinetic energy (TKE), Nepf et al. (2007) derive equations to predict this vortex scale. Their model is only valid for cases where $C_D ah > 0.1$, where a is frontal area density (the conventional measure of canopy density in the aquatic literature) and h is canopy height, when the canopy is dense enough to induce an inflection point and coherent vortices.

The conservation of turbulent kinetic energy, represented by k, takes the form

$$\frac{D}{Dt}\langle \bar{k} \rangle = -\langle \overline{u'w'} \rangle \frac{\partial}{\partial z}\langle \bar{u} \rangle - \frac{\partial}{\partial z}\langle \overline{w'k_s} \rangle - \frac{1}{\rho}\frac{\partial}{\partial z}\langle \overline{w'p'} \rangle - \frac{\partial}{\partial z}\left\langle \overline{\bar{w}''\bar{k}_s''} \right\rangle - e_c - e_v \qquad (3\text{-}3)$$

where p is pressure; u, v, and w are the x, y, and z components, respectively, of velocity; the overbar and single prime denote the mean and deviation from the

mean, respectively, over time; and the angle brackets and double prime denote the mean and deviation from the mean, respectively, over horizontal space (the x-y plane).

The first term in Equation 3-3 represents shear production of TKE. The second and third terms represent the vertical transport of TKE by turbulence and pressure fluctuations and cause no net gain or loss of TKE at the shear layer scale. The fourth term represents dispersive transport, which is negligible for canopies with $ah > 0.1$, where a is frontal area density and h is canopy height. The fifth term is dissipation of TKE by canopy drag, which happens through the conversion of shear-scale turbulence to stem wake turbulence, and takes the form

$$e_c = \frac{1}{2} C_D a \langle \bar{u} \rangle \left(2\langle \overline{u'^2} \rangle + \langle \overline{v'^2} \rangle + \langle \overline{w'^2} \rangle \right) \tag{3-4}$$

The sixth term is viscous dissipation of TKE and is negligible compared to canopy dissipation.

Shear production and canopy dissipation are the only significant terms in the TKE budget equation, so when they sum to zero, the growth of shear scale turbulence stops. When this occurs, the TKE equation can be rearranged to give

$$\frac{\langle \bar{u} \rangle C_D a}{\partial \langle \bar{u} \rangle / \partial z} = -\frac{2\langle \overline{u'w'} \rangle}{2\langle \overline{u'^2} \rangle + \langle \overline{v'^2} \rangle + \langle \overline{w'^2} \rangle} \tag{3-5}$$

Nepf et al. find from a literature review that the ratio of turbulence statistics on the RHS is constant at 0.20 ± 0.03. Nepf et al. define the LHS, evaluated at the position of maximum shear or approximately the canopy top, as the canopy shear layer (CSL) parameter. From a review of canopy flow datasets, they find that CSL = 0.23 ± 0.06. They calculate C_D for each dataset using a momentum balance, and they find that it is usually 0.2 to 0.35 for terrestrial canopies.

Nepf et al. then derive the following equation to relate the CSL to the depth of vortex penetration of the canopy, δ_e:

$$\frac{\delta_e}{h} \approx \frac{CSL}{C_D a h} \tag{3-6}$$

In doing so, they make the assumptions that the velocity below the vortex penetration depth is much less than the velocity at the canopy top, so that $\partial\langle\bar{u}\rangle/\partial z \approx U_h/\delta_e$, and that the inflection point and thus maximal shear occur at the canopy top, so that the CSL is evaluated using the velocity at the canopy top.

The authors confirm this derivation by measuring δ_e for each dataset and plotting δ_e/h versus $(C_D ah)^{-1}$ for the reviewed datasets. They find that lines with slopes within one standard deviation of the mean value of the CSL bound all plotted points, validating Equation 3-6. Thus, canopy morphology, not flow speed, determines the vortex penetration depth. Flow speed only affects penetration through the dependence of C_D and a on Reynolds number.

3.5 Effect of Coherent Vortices on Mean Flow

The coherent canopy shear vortices alter the mean velocity profile from its nonturbulent form. Harman and Finnigan (2007) develop a unified model to describe the effect of vegetation on flow both within and above the canopy. They note that MOST fails in the region that extends several canopy heights above the vegetation because of the influence of canopy turbulence. They call this region the roughness sublayer and aim to derive a formulation for velocity in this region that has a physical basis, incorporates stability and is simple enough to use for modeling applications.

The resulting formulation couples a canopy model with a modified surface-layer model. In deriving it, Harman and Finnigan (2007, p. 341) assume "horizontal, homogeneous, deep and dense canopies". Here, dense means that "almost all of the momentum is absorbed as drag on the foliage rather than as stress at the ground" (Harman and Finnigan 2007, p. 341). Since the ground interacts negligibly with the flow, Harman and Finnigan assume that its location is unimportant and thus define $z = 0$ as the top of the canopy, with displacement depth measured as distance below canopy top (Figure 3-2).

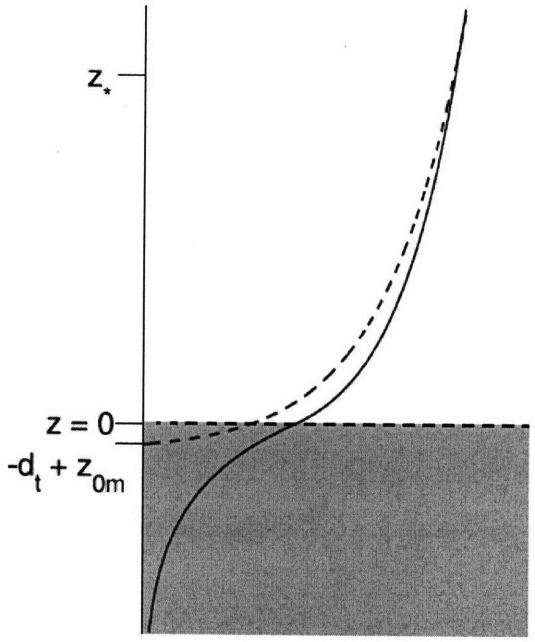

Figure 3-2: Harman and Finnigan (2007) definition sketch (their Figure 1). Canopy top is z=0. Dashed line is extrapolation of surface layer log profile, which goes to zero at the displacement depth, $-d_t+z_{0m}$. Solid line is the actual wind profile, which deviates from the surface layer profile below the height of the roughness sublayer, z^*.

The mixing length hypothesis provides a turbulence closure whose assumptions are not met in canopies but which is used for simplicity. In this hypothesis,

$$\frac{\tau(z)}{\rho} = \left(l_m(z)\right)^2 \left(\frac{dU}{dz}\right)^2 \tag{3-7}$$

where U is the mean wind, $l_m(z)$ is the mixing length, and $\frac{\tau(z)}{\rho}$ is the kinematic shear stress. They note that "the mixing length closure within the canopy should be viewed as a heuristic approximation to a closure that would reflect the role of large eddies in ensuring that the shear stress at a height z in the canopy is determined by momentum absorption over a height range containing z" (Harman and Finnigan 2007, p. 342). This approximation to a non-local closure is valid if canopy geometry does not change too rapidly in the vertical. They also note that problems exist in

extending this theory to scalar transport, because "the mean profile of a general scalar within and just above the canopy is highly dependent on the local distribution of sources and sinks and therefore care should be taken when extending this theory to scalars" (Harman and Finnigan 2007, p. 342).

They define a canopy penetration depth as $L_c = (c_D a)^{-1}$, where c_D is the drag coefficient and, following the convention in the terrestrial literature, a is the leaf area per unit volume (as opposed to frontal area index, as it was in Section 3.3). This penetration depth is the independent length scale for roughness sublayer flow.

The space- and time-averaged momentum equation within the canopy is

$$0 = -\frac{1}{\rho}\frac{\partial \tau}{\partial z} - F_D \equiv \frac{d}{dz}\left[l_m^2 \left(\frac{dU}{dz} \right)^2 \right] - \frac{U^2}{L_c} \tag{3-8}$$

where U is the mean wind speed and $F_D = U^2 / L_c$ is the kinematic canopy drag. If the canopy penetration depth (L_c) and mixing length (l_m) are assumed constant, then Harman and Finnigan argue that

$$U(z) = U_h \exp\left\{ \frac{\beta z}{l_m} \right\} \tag{3-9}$$

and

$$\frac{dU}{dz} = \frac{\beta}{l_m} U \tag{3-10}$$

within the canopy, where $\beta = \frac{u_*}{U_h}$, with U_h being the mean velocity at the top of the canopy and $u_* = (\tau_h / \rho)^{1/2}$ being the friction velocity above the canopy. The mixing length is related to the canopy penetration depth by $l_m = 2\beta^2 L_c$. Stability conditions affect flow through their effect on β and l_m.

Above the roughness sublayer, the MOST formulation still governs flow, but the similarity function is enhanced with a roughness sublayer function. From MOST,

$$\frac{dU}{dz} = \frac{u_*}{\kappa (z + d_t)} \Phi_m \tag{3-11}$$

where κ is the von Karman constant, Φ_m is the similarity function and is the product of the classic MOST similarity function (Equation 2-4, but here indicated by ϕ_m) and an enhancement function representing the influence of canopy-top turbulence (indicated by $\hat{\phi}_m$), and d_t is displacement depth below canopy top (see Figure 3-2, above, for the coordinate system for this derivation). The displacement depth is the centroid of drag on the canopy:

$$d_t = -\frac{\int_{-\infty}^{0} zU(z)^2/L_c dz}{\int_{-\infty}^{0} U(z)^2/L_c dz} = \frac{l_m}{2\beta} = \beta^2 L_c \tag{3-12}$$

and depends on stability through β. The roughness length, z_{0m}, is also a function of stability and canopy penetration depth.

The standard MOST similarity function, ϕ_m, depends on diabatic stability through the Monin-Obukhov length, $L = \frac{u_*^2 \Theta_0}{\kappa g \theta_*}$, where $\theta_* = -H/\rho c_p u_*$, H is sensible heat flux density, and Θ_0 is a background reference temperature. The MOST similarity function is

$$\phi_m(\zeta) = (1-16\zeta)^{-1/4} \quad \text{for } \zeta < 0 \tag{3-13}$$

and

$$\phi_m(\zeta) = 1+5\zeta \qquad \text{for } \zeta \geq 0 \tag{3-14}$$

where $\zeta = z/L$.

The roughness sublayer function, $\hat{\phi}$, scales on the vorticity thickness at the inflection point at canopy top, which is l_m/β.

$$\hat{\phi}_m(z) = 1 - c_1 \exp\{-\beta c_2 (z+d_t)/l_m\} \tag{3-15}$$

where $c_1 = [1-\hat{\phi}_m(z=0)]\exp\left\{\frac{c_2}{2}\right\}$ and c_2 is a constant that the authors find to be ½.

Thus, Φ_m, the product of the MOST similarity function and the roughness sublayer function, is

$$\Phi_m = \phi_m\left(\frac{z+d_t}{L}\right)\hat{\phi}\left(\frac{\beta(z+d_t)}{l_m}\right) \tag{3-16}$$

In order to find the vertical profile of the mean wind, Harman and Finnigan (2007) integrate Equation 3-11 to get

$$\frac{\kappa}{u_*}U(z) = \ln\left(\frac{z+d_t}{z_{0m}}\right) - \psi_m\left(\frac{z+d_t}{L}\right) + \psi_m\left(\frac{z_{0m}}{L}\right) + \hat{\psi}_m(z) \tag{3-17}$$

where ψ_m and $\hat{\psi}_m$ are the integrated forms of the classic MOST and roughness sublayer similarity functions, respectively. The classic MOST function can be integrated analytically, but the roughness sublayer function must be integrated numerically.

Harman and Finnigan (2007) argue that the mixing length just above and just below the canopy top must be constant if it is to be considered a mixing layer, and since vertical fluxes must be continuous at the canopy top, the vertical gradient of mean wind must also be continuous at the canopy top. Setting the above- and below-canopy formulations for the gradient equal at the boundary gives

$$\Phi_m(z=0) = \frac{\kappa d_t}{l_m} = \frac{\kappa}{2\beta} \tag{3-18}$$

With Equations 3-13, 3-14, 3-15, and 3-17, the vertical profile of the mean flow through the canopy can be calculated. Figure 3-3 shows the profile calculated with this formulation compared with measured profiles in three forests. The predicted profile agreed well with these measured profiles.

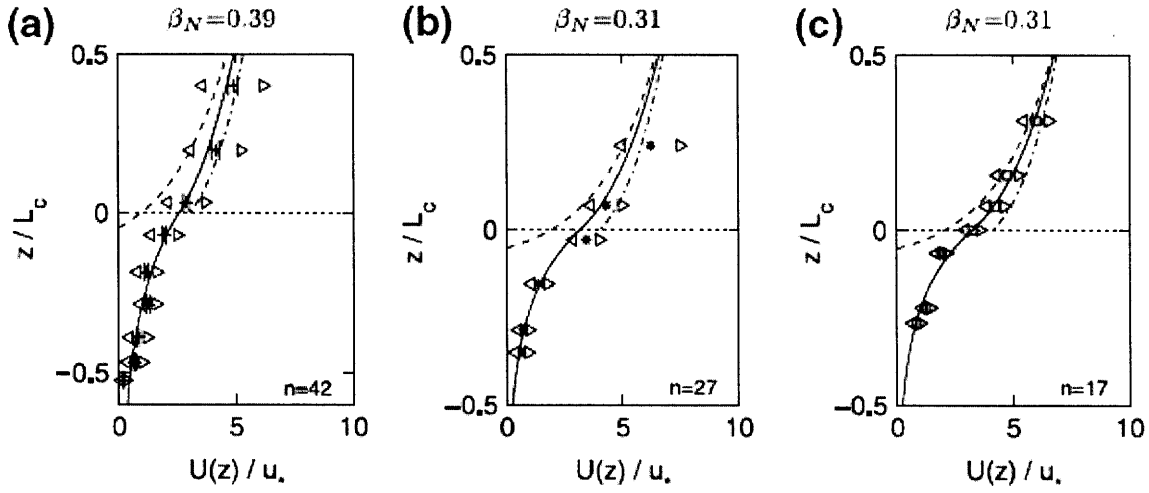

Figure 3-3: (Figure 6 from Harman and Finnigan 2007). Predicted profiles (solid lines) compared with field data (symbols with error bars) from (a) Tumbarumba Forest, Australia, (b) Duke Forest, North Carolina, and (c) Moga Forest, Australia. The dashed line represents the surface layer log profile, and the dash-dotted profile represents the profile predicted by a previous model by Physick and Garratt (1995).

Harman and Finigan (2007) suggest approximations that can be made in cases where only canopy height (h) and cumulative leaf area index (LAI) are known. They suggest taking $c_D = 1/4$ and $a \approx LAI/h$, so that $L_c \approx 4h/LAI$.

3.6 Diabatic and Topography Effects

Diabatic stability affects the profile of flow in the Harman and Finnigan (2007) model, as the mixing length and β both decrease with increasing stability. On the other hand, instability (buoyant mixing) reduces the shear that produces the mixing layer eddies, since "as the boundary layer becomes more unstable the inviscid instability associated with the inflection point will be less efficient at producing extra mixing due to the decreased shear from which it extracts energy" (Harman and Finnigan 2007, p. 350). Thus, while β and the mixing length increase in unstable conditions, this inefficiency in shear production diminishes the increase.

In general, diabatic stability can suppress turbulence in stratified conditions or enhance it through buoyant mixing in unstable conditions. The similarity function in the classic MOST formulation and in the Harman and Finnigan (2007)

model varies with stability conditions and thus incorporates stratification into these models of turbulent transport. Finnigan (2000) notes, though, that buoyancy only affects the flow significantly in strongly non-neutral conditions, and "in general, canopies are very rough surfaces in an aerodynamic sense, so quite large values of h/L are required before a significant influence of buoyancy is discernible" (Finnigan 2000, p.565). Because of the roughness, mechanical forcing of turbulence is strong, so thermal forcing of turbulence must be strong in order to be equally important. At night, low wind speeds frequently coincide with stable stratification, which can suppress vertical turbulent transfer and lead to an accumulation of mass that is then flushed rapidly once conditions become unstable (Baldocchi 2003). Most models are developed for neutral conditions because of the difficulties involved in modeling the effects of stratification.

Topography also affects fluxes and profiles of momentum and scalars. All the models of canopy flow reviewed here assume flat terrain. This assumption is part of the assumption of horizontal homogeneity, which is necessary for horizontal spatial averaging of the momentum and mass transport equations. Complex topography can change the vertical profile of the mean velocity. Finnigan (2000) found that mid-way up a hill, the inflection point disappeared from the velocity profile, while at the crest of the hill, the inflection point was exaggerated, and behind the hill, shielding could eliminate the canopy-top shear. Other studies have shown recirculation regions behind hills (e.g., Katul et al. 2006). Varied topography can induce vertical advection, when winds sweep up a hill, and drainage flows, which occur when denser air flows downhill (Baldocchi 2003). In field studies, multiple towers and instruments distributed in three dimensions are needed in order to quantify such horizontally inhomogeneous flows (Finnigan 2000). The lowland tropical rainforest of the Amazon has relatively flat topography, so models that assume flat terrain generally are valid, but complex topography dominates many locations, such as the mountainous tropical rainforest in Puerto Rico where this study conducted a field campaign. In conditions of varied topography, caution must be taken in applying models that assume horizontal homogeneity and in

generalizing conclusions to other locations.

Chapter 4:

Methods

Both field measurement and modeling techniques were used to investigate the relationship between above-canopy wind, canopy geometry, and subcanopy scalar transport. Field measurements of wind velocities and fluxes were collected with eddy covariance devices, and constrained numerical experiments using theory developed in Chapter 3 were conducted to test the fluxes predicted by different theoretical models of scalar transport.

4.1 Field Work Methods

Field work was conducted in March 2008 in the Luquillo National Forest in Puerto Rico in order to collect data on turbulence and scalar fluxes in a dense rainforest canopy. Measured fluxes were then compared to the predictions of candidate model formulations.

4.1.1 Eddy Covariance Method Theory

Turbulent flow and fluxes were measured with eddy covariance devices. The eddy covariance method determines turbulent transport from the covariance between fluctuations in wind velocity and fluctuations in scalar concentration. Eddy covariance devices sample turbulent fluctuations in wind and scalar concentrations at high frequency, and these high-frequency data are used to calculate turbulent fluxes.

The equation of conservation of mass provides the theoretical foundation for eddy covariance.

$$\frac{\partial c}{\partial t} + \nabla \cdot (\vec{q}c) = D\nabla^2 c + S \tag{4-1}$$

The first term on the LHS represents change in stored mass in a control volume; the second term on the LHS represents mass flux divergence. The first term on the

RHS represents mass flux due to molecular diffusion, which is several orders of magnitude smaller than turbulent diffusion and thus will be ignored here; and the second RHS term represents combined sources and sinks of mass.

Wind velocity ($\vec{q}$) and concentration (c) can be decomposed into their time-averaged value, indicated with an overbar, and the deviation from the time average, indicated with a prime. Thus, after Reynolds' averaging (and because, by continuity, $\nabla \cdot \bar{\vec{q}} = 0$), the $\nabla \cdot (\vec{q}c)$ term becomes

$$\nabla \cdot (\overline{\vec{q}c}) = \bar{\vec{q}} \cdot \nabla \bar{c} + \nabla \cdot (\overline{\vec{q}'c'}) \tag{4-2}$$

Note that Reynolds averaging of the product of two varying quantities, such as the vertical velocity q_z and c, gives a nonzero value of $\overline{q_z c}$ even when $\bar{q}_z$ is zero if the quantities are correlated (i.e., if $\overline{q_z'c'}$ is nonzero). The conservation of mass equation becomes

$$\frac{\partial \bar{c}}{\partial t} + \bar{\vec{q}} \cdot \nabla \bar{c} = -\nabla \cdot (\overline{\vec{q}'c'}) \tag{4-3}$$

If we then assume steady state conditions ($\frac{\partial \bar{c}}{\partial t} = 0$ and S constant in time), horizontal homogeneity in concentration ($\frac{\partial \bar{c}}{\partial x}$ and $\frac{\partial \bar{c}}{\partial y} = 0$, $\overline{u'c'}$ and $\overline{v'c'} = 0$), and no mean wind in the vertical ($\bar{w} = 0$), the mass conservation equation becomes

$$0 = -\frac{\partial}{\partial z}(\overline{w'c'}) + S, \text{ or}$$

$$\frac{\partial}{\partial z}(\overline{w'c'}) = S \tag{4-4}$$

In other words, the divergence of the vertical turbulent flux ($\overline{w'c'}$) equals the sum of sources and sinks. By measuring w and c at high frequencies, the eddy covariance method can resolve this vertical turbulent flux for turbulence of very fine time scales. For each sampling time point, w and c are multiplied to get instantaneous flux, and all instantaneous fluxes are summed over some averaging period. The average flux, $\overline{wc}$, is then subtracted from each instantaneous flux to get

instantaneous deviation from the mean, $w'c'$, which is averaged over the averaging period to get the mean vertical turbulent flux, $\overline{w'c'}$:

$$\overline{wc} = \frac{\sum_{t=1}^{\tau} wc}{\tau} \tag{4-5}$$

where τ is the number of measuring time points in the averaging period;

$$w'c'(t) = wc(t) - \overline{wc}$$

where t is each discrete measuring time point; and

$$\overline{w'c'} = \frac{\sum_{t=1}^{\tau} w'c'}{\tau} \tag{4-6}$$

An eddy covariance device measures these high-frequency instantaneous variables with a three-dimensional sonic anemometer and an open-path infrared gas analyzer. The instruments can generally sample at frequencies of 5-20 Hz. The sonic anemometer records temperature and three components (x, y, z) of the wind vector (or equivalently, wind speed, azimuth, and elevation angle), and the gas analyzer records concentrations of carbon dioxide and water vapor. Data collected with eddy covariance devices can be used to measure flux at a single point, or if using multiple devices, to resolve the profile of fluxes over a vertical or horizontal transect.

4.1.2 Puerto Rico Site Description

In the present study, two eddy covariance devices were used to measure fluxes at the top and bottom of a rainforest canopy in the Luquillo National Forest in Puerto Rico. This section describes the experimental site's hydrology and climate, topography, and canopy geometry.

Hydrology and Climate

The Bisley catchment in the Luquillo National Forest is located at 18°18'N, 65°50'W (Schellekens 2000) in the Luquillo Mountains of northeastern Puerto Rico.

Figure 4-1 shows the location of the field site on the island of Puerto Rico. The catchment covers altitudes from 265 to 456 m above sea level. Within the catchment, there are two scaffolding towers constructed to support micrometeorological measurements. The lower Bisley tower, where this investigation took place, is located at 18° 18' 51.893" N, 65° 44' 41.694" W, at 310 m above sea level (LTER 2008).

Figure 4-1: Green arrow indicates location of Luquillo National Forest in Puerto Rico. Map from maps.google.com.

The Luquillo Mountains have a "maritime tropical" climate, with average annual rainfall of 3530 mm +/- 22.6%. (Schellekens 2000) Precipitation occurs largely in frequent events of low intensity and duration, and northeasterly trade winds bring about 70% of precipitation. There is only mild seasonality in precipitation, but May through November is a relatively wetter season, and January through March is relatively drier. Seasonal variation in temperature is similarly mild, ranging from about 24°C in December-February to about 27.5°C in July-August. Relative humidity remains fairly constant through the year at 84-90%. Wind speeds average less than 2 m/s in lower, more sheltered areas but reach 2-5 m/s on exposed summits. Potential evaporation is approximately 1100 mm/yr.

Schellekens et al. (2000) used hydrologic and meteorological measurements to estimate evaporation from the Bisley catchment. Their results showed that throughfall is low at this site, varying seasonally between 45% in the summer to 70% in the winter and spring. Average annual evaporation for the period studied was ~2300 mm/yr, which was partitioned into transpiration, evaporation from the soil and litter layer, and evaporation of intercepted rainfall from leaves. Evaporation from the soil and litter layer was assumed to be negligible because "only 3.5% of the radiation reach[es] the forest floor" (Schellekens et al. 2000, p. 2185). The authors did not address the importance of wind and turbulent transport at the ground in this assumption. Most evaporation at this site (~60%) occurs as interception loss from a wet canopy, and the authors assumed that the remainder occurs as transpiration. The overall value of evapotranspiration and the value of interception loss were both larger than results of other evaporation studies of tropical sites. The authors attribute this discrepancy to high interception losses due to the frequent low-intensity rainfall.

Soil in the Bisley watershed is clayey for the first 0.8-1.0 m, but roots and invertebrates break it up enough to give it high conductivity in the top ~20 cm, while below 20 cm, it is highly impermeable (F. Scatena, personal communication). Below the clayey layer lies weathered bedrock with very low permeability, followed by unweathered bedrock more than 15 m below the level of the stream channel (Schellekens et al. 2000).

Topography

The topography in the Bisley watershed consists of sharp divides, steep stream gradients, and bowl-shaped valleys. Slopes greater than or equal to 24° (45%) cover more than 50% of the catchment. (Schellekens et al. 2000) Figure 4-2 shows the topography of the area around the watershed.

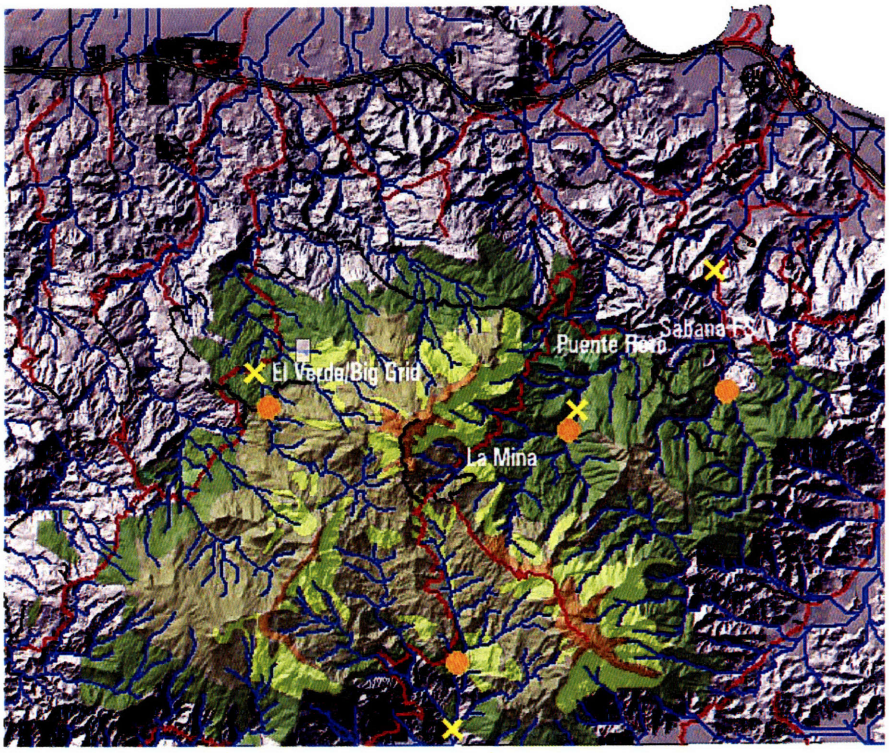

Figure 4-2: The Bisley watershed. The lower Bisley tower is located in the northwest (top right) corner of the green area, which represents the Luquillo National Forest. (Image courtesy of Fred Scatena).

The lower Bisley tower sits on a crest part way up the slope of a major ridge in the mountain chain. As such, the land slopes away from the tower on three sides (north, west, and south). To the north of the tower, the land continues to slope downward to the coast, while to the south of the tower, the land dips before rising again to the highest ridge. Figure 4-3 depicts the topography of the lower Bisley tower area. The prevailing wind tends to blow from the northeast (Schellekens et al. 2000) and thus flows up the slope from the coast in order to reach the tower. The fetch for wind from the north-northeast is infinite because it extends to the Atlantic, while the fetch for winds from the south is short, on the order of hundreds of meters, because of sheltering by the larger ridge of the Luquillo Mountains (F.N. Scatena, personal communication 5/2008). Thus, flow from the north has much more time to become a fully developed canopy roughness sublayer than does flow from the south.

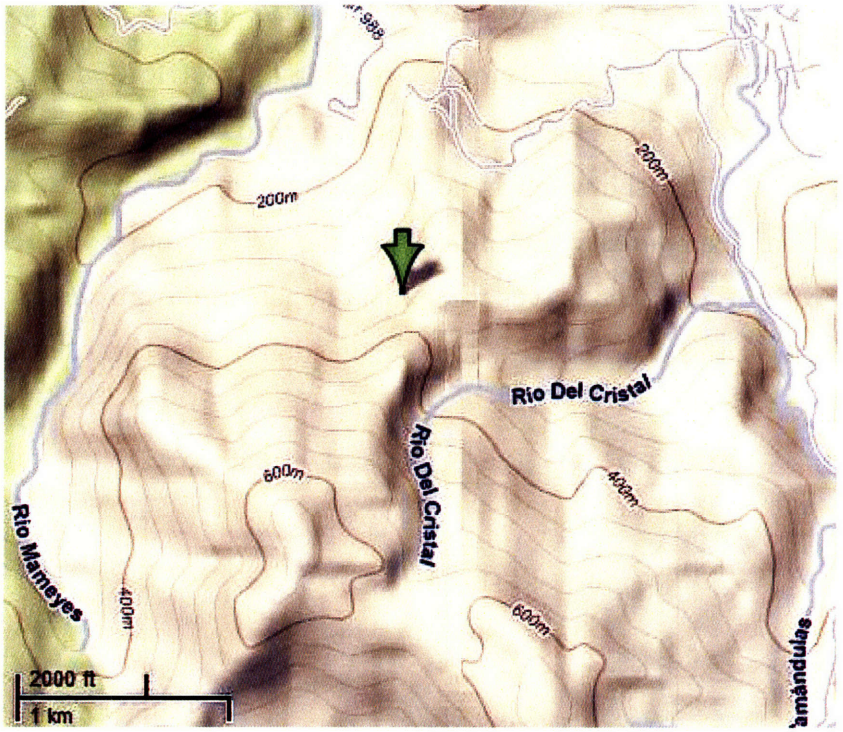

Figure 4-3: Topography around Lower Bisley Tower; north is up, and green arrow indicates the tower. Image from maps.google.com.

Canopy Characteristics

Four forest types exist in the Luquillo Mountains: Tabonuco, Colorado, palm, and dwarf. Tabonuco forest occupies the lowlands up to about 600 m and surrounds the lower Bisley tower. The lowland Tabonuco forest consists of several key trees: the Tabonuco is the slow-growing climax species and tops the canopy, growing to approximately 25 m (Schellekens et al. 2000). Its leaves are distributed over most of its height. The Cecropia, or Trumpet Tree, is a fast-growing pioneer species that dominates in recently disturbed areas (often disturbed by wind damage), and it reaches 20 m (Crow 1980). It tends not to coexist with the Tabonuco, and few, if any, were visible close to the tower. Finally, a type of palm tree also grows below both the Tabonuco and the trumpet tree, and below the Tabonuco it typically grows to heights between about 3 and 6 m. Below these trees, a variety of ferns, vines, and other small vegetation grows relatively sparsely on the forest floor.

The leaf area index (LAI) of the Tabonuco forest surrounding the tower was measured during this experimental campaign using a LI-COR Model LAI-2000 Plant Canopy Analyzer. Figure 4-4 shows vertical profiles of LAI values and leaf area density. The LAI for the whole canopy, measured at the ground level, was 5.33. Peaks in leaf area density (m^2 of leaf area per m^3 of canopy volume) occurred at ~18 m, where the Tabonuco leaves were most dense, and from the ground to ~8 m, where the palms and smaller trees and shrubs dominated the subcanopy space.

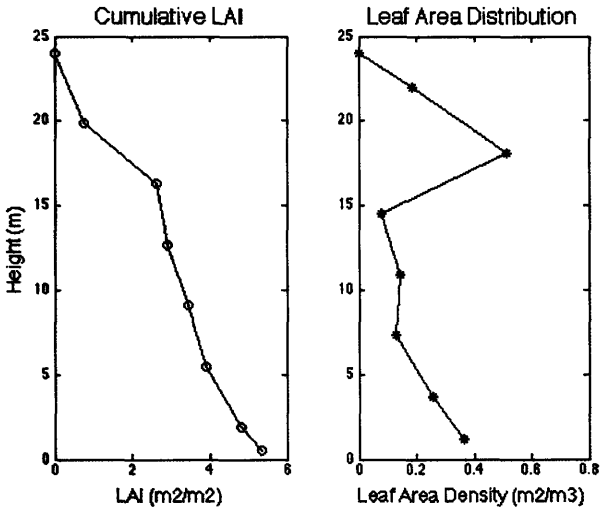

Figure 4-4: Vertical profiles of cumulative leaf area index (left) and leaf area distribution (right) at the Bisley tower.

4.1.3 Experimental Setup

The lower Bisley tower rises approximately 24 m above the forest floor, and its top sits about 1 m above the canopy top. It is constructed of aluminum scaffolding and has a walk-up staircase with 13 floor plates at intervals of about 1.8 m. The left panel of Figure 4-5 gives a view of the tower from the base, and the right panel shows the top of the tower. As described in Section 4.1.2, the tower sits on an intermediate ridge, with downward slopes to the north, west, and south. The slope to the north continues down to the ocean, while the slope to the south rises again towards the peaks of the Luquillo Mountains.

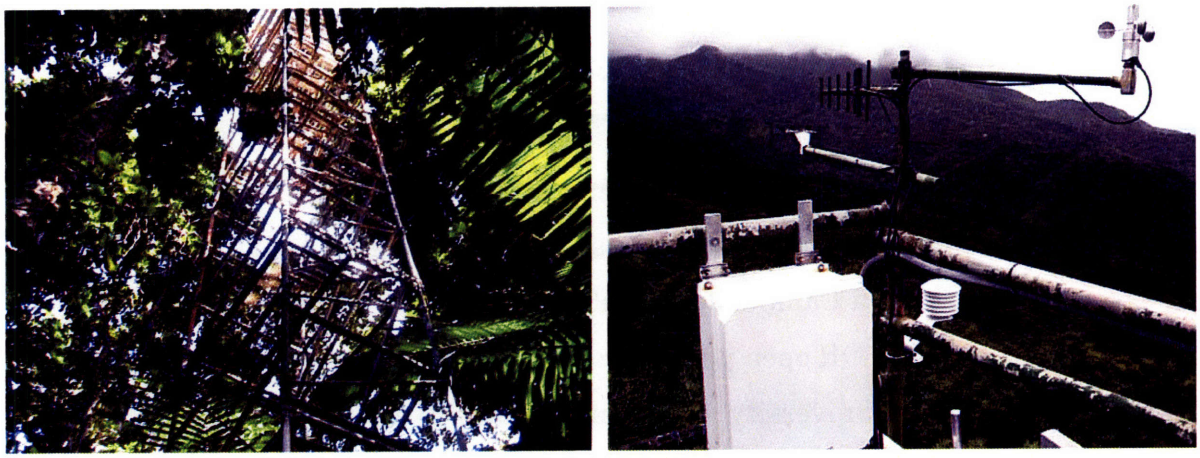

Figure 4-5: Left: view of Lower Bisley Tower from the ground; right: top of Bisley Tower, looking west. Instruments are US Forest Service meteorological sensors.

The US Forest Service maintains instruments at the top of the tower that take continuous meteorological data, including temperature, pressure, humidity, downward and net solar radiation, precipitation, and wind speed and direction. During the experimental campaign, the Forest Service recorded ten-minute averages of these data and shared them with us.

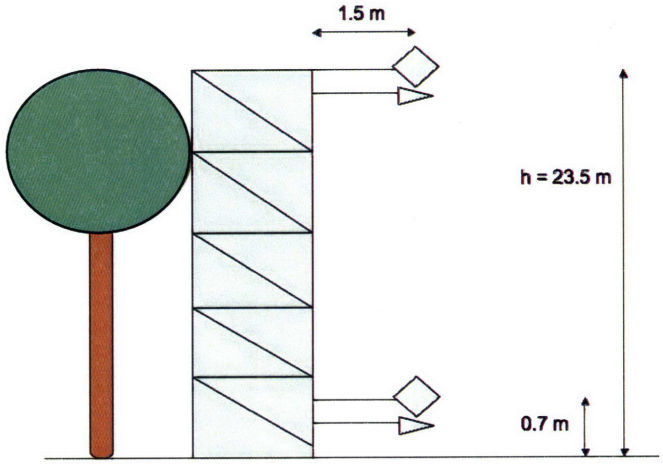

Figure 4-6: Schematic diagram of eddy covariance instrument orientation on the Bisley Tower. Diamonds represent sonic anemometers, and triangles represent gas analyzers.

Two eddy covariance devices were attached to the tower, one at the top (~23.5 m) and one at the bottom (~0.7 m). Figure 4-6 schematically represents the setup of the instruments on the tower. The device at the top consisted of an RM Young Model 81000 three-dimensional sonic anemometer and a LI-COR Model 7500 open path gas analyzer, both belonging to Professor Rafael L. Bras of MIT. The device at the bottom consisted of a Campbell Scientific CSAT-3 three-dimensional sonic anemometer and a LI-COR open path gas analyzer, both belonging to Professor Gabriel Katul of Duke University. Aluminum booms fixed the devices 1.5 m away from the tower. For each device, the anemometer and gas analyzer were positioned close enough to measure approximately the same parcel of air, but far enough to avoid interfering with the flow reaching the other sensor. Figure 4-7 shows the attachment apparatus and the positioning of the sensors.

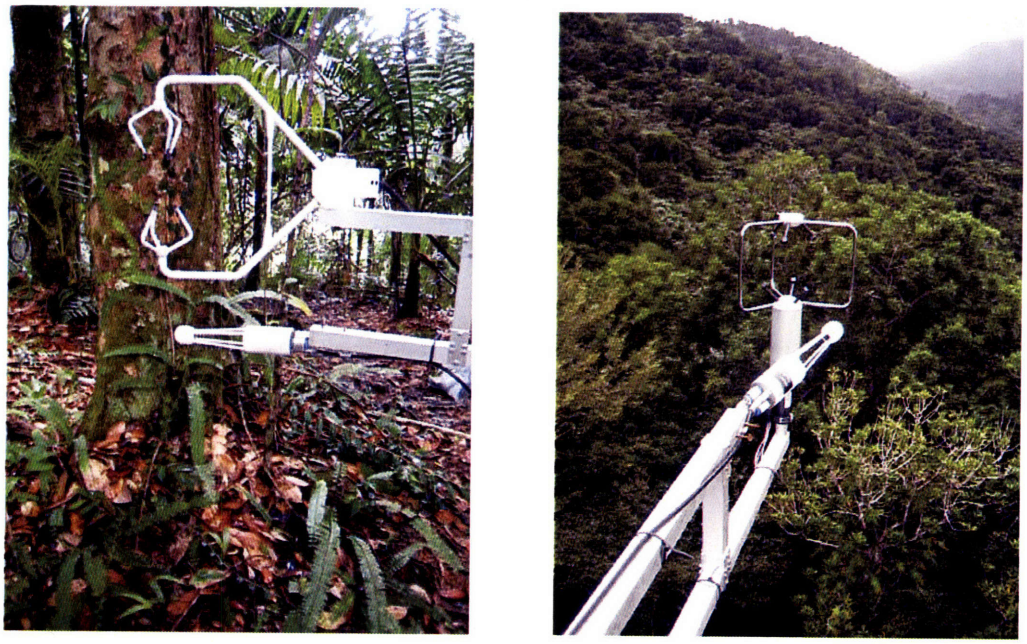

Figure 4-7: Eddy covariance device attachment and orientation. Left: CSAT3 anemometer and LICOR-7500 gas analyzer at ground level; right: RM Young 81000 anemometer and LICOR-7500 gas analyzer above canopy.

Both devices were connected to a Campbell Scientific CR5000 data logger positioned in the middle of the tower. The RM Young anemometer was connected to

the analog voltage differential ports of the data logger using ~15 m of Ethernet cable, while both gas analyzers and the CSAT anemometer were connected to the SDM port of the data logger, also using ~15 m of Ethernet cable each. Both gas analyzers had the same default SDM address, and the only way to change the address was by connecting them to a computer. Unfortunately, both gas analyzers failed to connect and communicate with the computer, so we were unable to change either of the SDM addresses. Because of this, only one gas analyzer could be connected to the data logger SDM port at a time, so we could only collect gas concentration data from one location (top or bottom) at a given time. On March 17 and 18, 2008, we sampled from the gas analyzer at the bottom of the tower, and on March 19 and 20, we sampled from the gas analyzer at the top of the tower. Appendix A contains diagrams of the wiring on the instrument and data logger boards and the connections between the instruments, logger, and batteries.

Each device and the data logger were powered with a separate 12-V, 120 amp-hr marine deep cycle battery. The batteries were placed on the floor plates next to each device and were connected to the devices using lamp cord. The battery voltages were monitored, and the batteries were recharged every two to three days.

Data were collected March 17-20, 2008. Different types and resolutions of data were collected each day as data storage problems were resolved and the data logger sampling program was improved. The initial intent was to store high frequency (10Hz) data on a PCMCIA card inserted into the data logger, but the logger did not recognize the card, and it was not possible to obtain a memory card that it would accept. The CR5000 logger has 1MB of memory, and space not used for the operating system and user programs can be used for data storage. Since this amount of memory is inadequate for storing high frequency data, on March 17, 5-minute averages of wind components, gas concentrations, and the product of vertical velocity and gas concentrations were sampled, because the logger's memory could store a day's worth of 5-minute averages. On March 18 and 19, the logger program was changed to sample the same averages at 2-second intervals, which required the data to be downloaded from the logger hourly to maintain space in the

memory. On March 20, a faster connection was established between the computer and the logger by increasing the baud rate, making it possible to download data continuously from logger to computer and thus to sample high frequency data without filling up the logger memory before it could be emptied. Table 4-1 outlines the data gathered on each day.

Table 4-1: Characteristics of collected data.

Day	Data Frequency	Position of Gas Analyzer
3/17/2008	5-min and 2-sec average	Bottom
3/18/2008	2-sec average	Bottom
3/19/2008	2-sec average	Top
3/20/2008	10 Hz	Top

Averages were recorded by summing 10 Hz data over the averaging period within the logger operating system and then storing only the average in the logger memory. For instance, to calculate 5-minute averaged vertical wind velocity (represented by the variable Uz), a counter and Uz sum were set to zero, and at each subsequent 10 Hz sampling point, the instantaneous value of Uz was added to the Uz sum variable. Once the counter reached 3000 (10 Hz * 60 s/min * 5 min), the Uz sum variable was divided by the number of samples in the period (3000) and stored, and the counter and sum were reset to zero. The same procedure was applied to the three wind components for both the RM Young and CSAT anemometers, the H_2O and CO_2 concentrations from the single operating gas analyzer, and the product of instantaneous vertical wind and gas concentrations. Thus, values of $\overline{u_{top}}$, $\overline{v_{top}}$, $\overline{w_{top}}$, $\overline{u_{bottom}}$, $\overline{v_{bottom}}$, $\overline{w_{bottom}}$, $\overline{wCO_2}$ (or $\overline{wc}$), and $\overline{wH_2O}$ (or $\overline{wr}$) were collected. From these values, turbulent fluxes of carbon dioxide, moisture, and momentum over the averaging period can be calculated, as described in Section 4.1.1, using

$$\overline{w'c'} = \overline{wc} - \overline{w} \cdot \overline{c} \quad \text{for } CO_2 \tag{4-7}$$

$$\overline{w'r'} = \overline{wr} - \overline{w} \cdot \overline{r} \quad \text{for } H_2O \tag{4-8}$$

$$\overline{u'w'} = \overline{uw} - \overline{u} \cdot \overline{w} \quad \text{for momentum.} \tag{4-9}$$

Appendix B contains the logger programs used to sample at each frequency. The high frequency data collected on March 20 contains these same three-component wind and gas concentration data but also contains the temperature at each anemometer. All calculations and averaging for the high frequency data were conducted in the post-processing phase, rather than in the logger program.

4.2 Modeling Methods

In addition to the field experiments to collect data on scalar transport in the canopy, we also conducted constrained numerical experiments with different mathematical formulations of scalar and momentum transport. The theories of scalar and momentum transport described in Chapter 3 were inserted into a section of the ED program code and used to calculate resistance to transfer within the canopy and latent heat flux from the soil.

The first formulation tested was the formulation currently found in the model and based on the rough-wall boundary layer and exponential decay of diffusivity through the canopy outlined in Section 2.6. Again, in this formulation, the resistance to scalar transfer from the ground to the canopy airspace is calculated by

$$r'_{aw} = \int_{z_{0w}}^{z_{0w}+d} \frac{dz}{K_w(z)} = \frac{z_{top}}{aK_w(z_{top})}\left[e^{a(1-z_{0h}/z_{top})} - e^{a(1-(z_{0h}+d)/z_{top})}\right] \tag{4-10}$$

which is the same as Equation 2-19, where a is an extinction coefficient currently set to 2.5 for all vegetation types, d is the displacement height defined as $0.63h$, and $K_w(z_{top}) = ku_*(z_{top} - d)$.

Second, a sensitivity test was conducted on the extinction coefficient, a. The current model formulation was used, but a was varied from 0.5 to 5.5.

Third, the Harman and Finnigan (2007) formulation of velocity profile was used to formulate an eddy diffusivity for momentum, and this momentum diffusivity was assumed to equal scalar diffusivity, an assumption also made in the

current ED model formulation. As described in Section 3.4, Harman and Finnigan (2007) define a constant mixing length, l_m, in the canopy as

$$l_m = 2\beta^3 L_c \tag{4-11}$$

where $\beta = u_*/\overline{u_{top}} \approx 0.3$ for stratifications relatively near neutral, and $L_c = (c_D a)^{-1} \approx 4h/LAI$ where $c_D \approx \frac{1}{4}$ is the drag coefficient at the leaf scale, and $a \approx LAI/h$ is the leaf area per unit volume. Thus,

$$l_m \approx \frac{8(0.3)^3 h}{LAI} \tag{4-12}$$

In mixing length theory (e.g. Poggi and Katul 2007, Equation 14), eddy diffusivity for momentum is defined as

$$K_m = l_m^2 \left| \frac{d\bar{u}}{dz} \right| \tag{4-13}$$

In order to maintain a continuous velocity gradient across the canopy top, Harman and Finnigan (2007) define the gradient of the mean wind using different equations above and within the canopy. Above the canopy,

$$\frac{d\bar{u}}{dz} = \frac{u_*}{\kappa(z-d)} \Phi_m \tag{4-14}$$

from MOST similarity theory above the canopy, where $\Phi_m = \frac{\kappa}{2\beta}$ accounts for the extra mixing generated by the mixing layer at the top and for stability (if β is made to vary with stability). Within the canopy,

$$\frac{d\bar{u}}{dz} = \frac{\beta}{l_m} \bar{u} \tag{4-15}$$

from the assumptions of constant mixing length and an exponential velocity profile within the canopy. Integrating Equation 4-14 from canopy top to atmospheric reference height gives

$$\overline{u_{top}} = \overline{u_{atm}} - \frac{u_*}{2\beta} \ln\left(\frac{z_{atm} - d}{z_{top} - d} \right) \tag{4-16}$$

Integrating Equation 4-15 from a height z in the canopy to the canopy top, z_{top}, gives

$$\bar{u}(z) = \overline{u_{top}} \exp\left\{\frac{\beta}{l_m}(z - z_{top})\right\} \tag{4-17}$$

Substituting the expression for $\bar{u}$ from Equation 4-17 into Equation 4-15 yields

$$\frac{d\bar{u}}{dz} = \frac{\beta}{l_m}\overline{u_{top}} \exp\left\{\frac{\beta}{l_m}(z - z_{top})\right\} \tag{4-18}$$

Substituting the expression for $\overline{u_{top}}$ in Equation 4-16 into Equation 4-18, and substituting the resulting expression for $\frac{d\bar{u}}{dz}$ into Equation 4-13 gives

$$K_m = l_m \beta \left[\overline{u_{atm}} - \frac{u_*}{2\beta}\ln\left(\frac{z_{atm} - d}{z_{top} - d}\right)\right] \exp\left\{\frac{\beta}{l_m}(z - z_{top})\right\} \tag{4-19}$$

Substituting the expression for K_m in Equation 4-19 into Equation 2-16 and integrating from the ground to the displacement height then gives resistance to momentum transfer from the ground to the canopy airspace.

$$r'_{am} = \int_{z_{om}}^{z_{om}+d} \frac{dz}{K_m} = -l_m^2 \left[\overline{u_{atm}} - \frac{u_*}{2\beta}\ln\left(\frac{z_{atm} - d}{z_{top} - d}\right)\right] \left[\exp\left\{\frac{\beta}{l_m}(z_{om} + d - z_{top})\right\} - \exp\left\{\frac{\beta}{l_m}(z_{om} - z_{top})\right\}\right] \tag{4-20}$$

where z_{om} is the roughness length for momentum. If we then make the significant assumption, as does the current model formulation, that the diffusivities and roughness lengths for momentum and scalars are equivalent, it follows that

$$r'_{aw} = r'_{am}.$$

The fourth model formulation tested derives from findings in Nepf et al. (2007) that mixing layer vortices penetrate the canopy to a fixed depth that can be calculated from canopy geometry. As discussed in Section 3.3, Nepf and colleagues found negligible transfer of scalars from the zones below the penetration depth of the large coherent vortices. Thus, this modeling experiment seeks to implement a threshold for scalar transport from subcanopy soil based on the canopy penetration depth. If the penetration depth is greater than or equal to the canopy height, then

transfer of scalars from the soil to the canopy airspace occurs according to one of the previously described resistance formulations. If, however, the penetration depth is less than the canopy height, transfer of scalars from the soil to the canopy airspace is turned off.

The Nepf study argues that, when shear production balances canopy dissipation, the coherent, canopy-top vortices reach a fixed size with a canopy penetration depth δ_e. The ratio of canopy penetration to canopy height scales on features of canopy geometry:

$$\frac{\delta_e}{h} \approx \frac{CSL}{(c_D a h)} \tag{4-21}$$

where *CSL* is the canopy shear layer parameter described in Section 3.3 and which has a value of 0.23, c_D is the drag coefficient of ~0.25 and a is the frontal area of vegetation per unit volume, which is assumed to be approximately equal to leaf area density, which in turn is about *LAI/h*. Thus,

$$\frac{\delta_e}{h} \approx \frac{0.92}{LAI} \tag{4-22}$$

When $\delta_e/h \geq 1$, soil evaporation is calculated according to one of the eddy diffusivity formulations. When $\delta_e/h < 1$, soil evaporation is turned off. Thus, with Equation 4-22, soil evaporation only occurs under canopies with LAI less than or equal to 0.92. If, however, we do not assume the relationship with the experimentally determined CSL parameter and instead use a scaling argument, such that

$$\frac{\delta_e}{h} \sim (c_D LAI)^{-1} \tag{4-23}$$

then soil evaporation occurs for canopies with LAI less than or equal to 4 (given a drag coefficient of 0.25).

Both of these options were tested. When soil evaporation was turned on, it was calculated using a resistance formulated with the rough wall boundary layer formulation (Equation 2-19, current ED model formulation). The Harman and Finnigan (2007) model (Equation 4-20) cannot be used because it does not apply to the case where vortices penetrate to the ground, as it was derived for "dense"

canopies where all drag is absorbed by the vegetation before penetrating to the ground. Canopies below the vortex-penetration cutoff may not be dense enough to trigger coherent mixing-layer vortices, so the rough wall boundary formulation of resistance may be more physically accurate.

All model formulations were tested by calculating the resistance, r'_{aw}, and the soil latent heat flux, λE_g, as functions of canopy height and LAI. As described in Section 2.6,

$$\lambda E_g = \lambda \rho_{atm} \frac{(q_s - q_*(T_g))}{r'_{aw} + r_{srf}} \tag{4-24}$$

where $\rho_{atm} \approx 1$ kg/m^3 and $r_{srf} = \frac{r'_{aw}(1-\beta_c)}{\beta_c}$, with β_c (the ratio of soil water content to saturation water content) arbitrarily set to 0.3. The latent heat of vaporization of water, λ, depends on temperature, but both the ED and NCAR LSM models take it as a constant with a value of 2.51×10^6 J/kg (Bonan 1996). For the tests, the values of canopy airspace specific humidity, q_s, and saturation specific humidity at the soil temperature, $q_*(T_g)$, were also chosen arbitrarily to be representative of a rainforest canopy, based on meteorological data from the Puerto Rico campaign.

$q_s = 0.0133$ kg water/kg air

$q_*(T_g) = 0.0144$ kg water/kg air

$T_g = 20^\circ C$

The MATLAB programs used for the modeling experiments can be found in Appendix C.

Chapter 5:

Results

5.1 Field Results

5.1.1 General Meteorological Conditions

Meteorological conditions during the data collection period (March 17-20, 2008) were fair and relatively cool. Figure 5-1 shows temperature, relative humidity, and specific humidity for the days that data were collected. Temperature remained between 20 and 24°C, and specific humidity was generally between 0.012 and 0.014 kg/kg. Sporadic light rain occurred on the data collection days, as shown in Figure 5-2, but it was only heavy enough to interrupt data collection by the eddy covariance devices for part of the day on March 18. Total downward radiation and net shortwave radiation are shown in Figure 5-3. As expected, both total and net solar radiation peak at midday and drop to zero at night. The low radiation levels on March 18 are the result of overcast conditions related to the higher precipitation on that day.

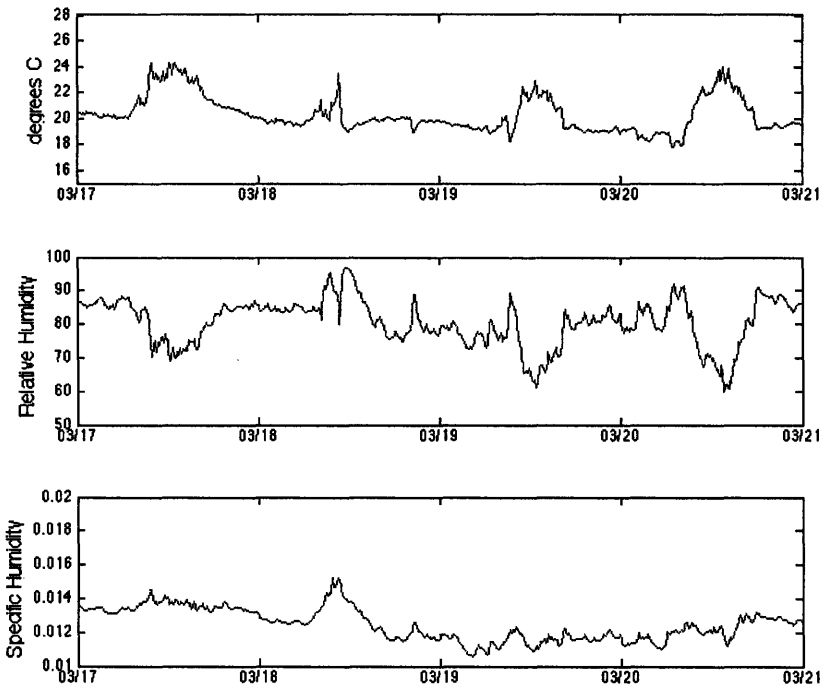

Figure 5-1: Temperature (top), relative humidity (%, center), and specific humidity (kg water/kg air, bottom) for data collection days. Meteorological data courtesy of USDA Forest Service.

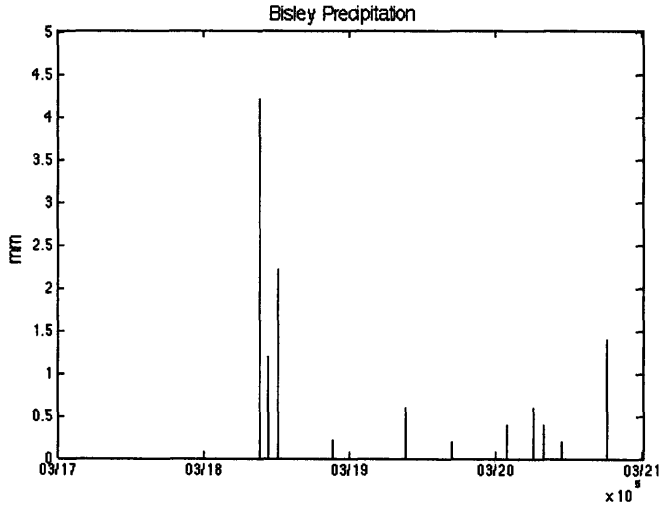

Figure 5-2: Precipitation on data collection days, in mm per 10 minute collection interval, courtesy of USDA Forest Service.

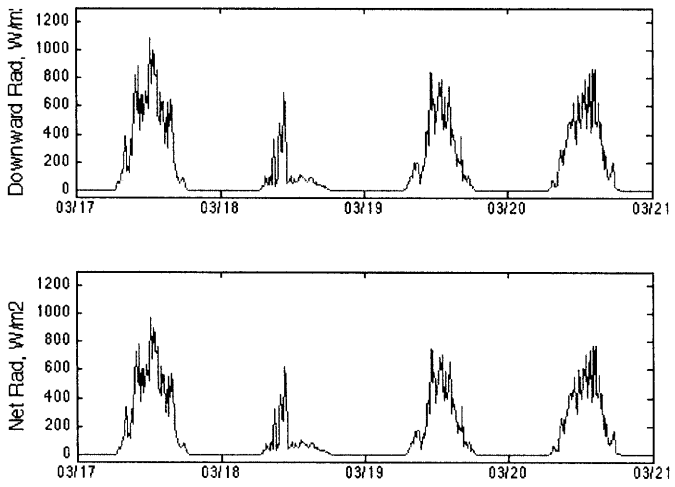

Figure 5-3: Downward shortwave radiation (top) and net shortwave radiation (bottom), both in W/m^2, courtesy of USDA Forest Service.

The temperatures and mean wind speeds recorded by the USDA Forest Service and the RM Young sonic anemometer at the top of the canopy agreed reasonably well, as shown in Figures 5-4 and 5-5. The differences are probably due to differences in instrument calibration and horizontal positioning, with a lateral distance of 1 to 3 meters between the RM Young sonic anemometer and the US Forest Service meteorological sensors.

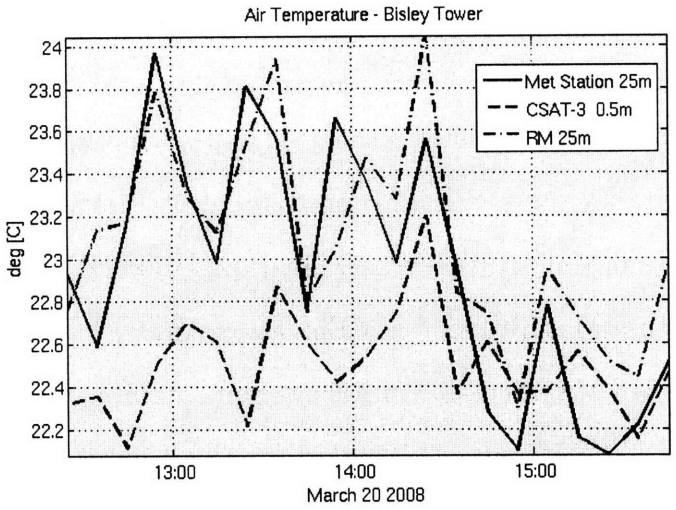

Figure 5-4: Agreement of temperature measurements made by meteorological station instrument ("met station") and both sonic anemometers, averaged over 10 minute periods.

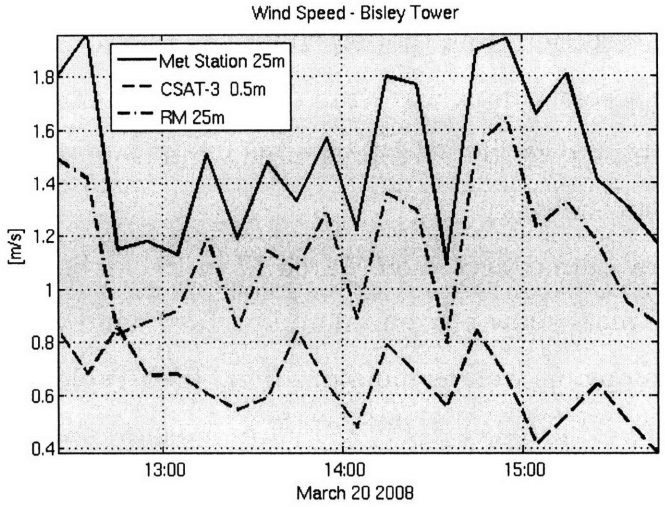

Figure 5-5: Agreement of wind speed measurements between meteorological station cup anemometer ("met station") and both sonic anemometers, averaged over 10 minute periods.

5.1.2 Eddy Covariance Results

For March 17, 18, and 19, wind components and fluxes were calculated within the data logger program for each instantaneous sampling point, then averaged over a period of either 5 minutes or 2 seconds, and only these average

values were stored (as described in Section 3.3). The RM Young anemometer sampled wind magnitude, azimuth, and elevation angle, and these values were converted in the data logger program to the *x*, *y*, and *z* wind velocity components:

$$\text{Horizontal Wind} = (\text{Wind Magnitude}) * \cos(\text{Elevation Angle}) \quad (5\text{-}1)$$

$$U_x = (\text{Wind Magnitude}) * \cos(\text{Elevation Angle}) * \cos(\text{Azimuth}) \quad (5\text{-}2)$$

$$U_y = (\text{Wind Magnitude}) * \cos(\text{Elevation Angle}) * \sin(\text{Azimuth}) \quad (5\text{-}3)$$

$$U_z = (\text{Wind Magnitude}) * \sin(\text{Elevation Angle}) \quad (5\text{-}4)$$

Horizontal wind for the CSAT (which sampled the three wind velocity components) was calculated as follows:

$$\text{Horizontal Wind} = (U_x^2 + U_y^2)^{1/2} \quad (5\text{-}5)$$

Instantaneous fluxes were calculated as the product of instantaneous scalar (H_2O, CO_2, heat) concentration and instantaneous vertical velocity (U_z).

The raw wind direction from the RM Young and CSAT anemometers was not aligned. For the purpose of comparing wind direction, the angles for both anemometers were rotated so that 0° represented wind from the south and 90° represented wind from the west.

Plots of the raw data collected on March 17 to 19 can be found in Figures 5-6 through 5-10. These plots show horizontal and vertical wind velocities at the top and bottom of the canopy, as well as moisture flux. (See Table 4-1 for characteristics of data collected each day). Figure 5-6 shows a ground latent heat flux fluctuating around 10 W/m^2 using a five-minute averaging period on March 17, and Figure 5-8 confirms this range of values using a two-second averaging period on the same day. Figure 5-7 shows that both vertical and horizontal velocity components were significantly smaller at ground level than above the canopy on March 17, using a two-second averaging period. Figure 5-9 shows that, on March 19, horizontal velocity at ground level was more comparable to, though still smaller than, horizontal velocity above the canopy. Vertical velocity at ground level was still considerably smaller than vertical velocity above the canopy. Figure 5-10 shows that, on March 19 and using a two-second averaging period, the magnitude of

latent heat flux above the canopy reached peaks up to 1000 W/m^2 and consistently had a value of several hundred W/m^2. Thus, latent heat flux measured on March 19 above the canopy was at least an order of magnitude larger than latent heat flux measured on March 17 at ground level.

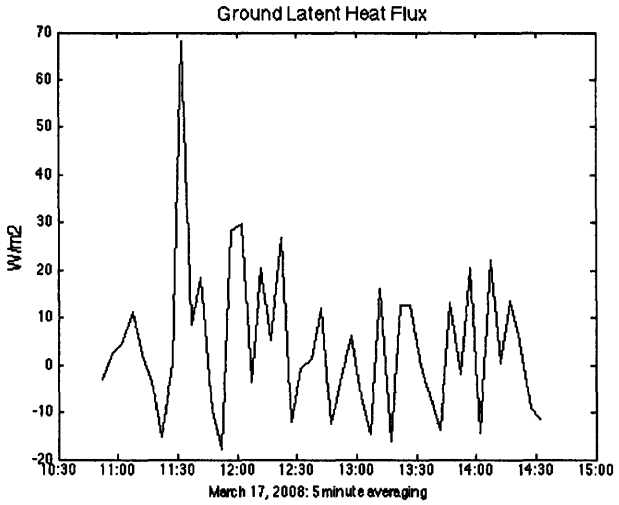

Figure 5-6: Five-minute-averaged ground-level latent heat flux for 3/17/08.

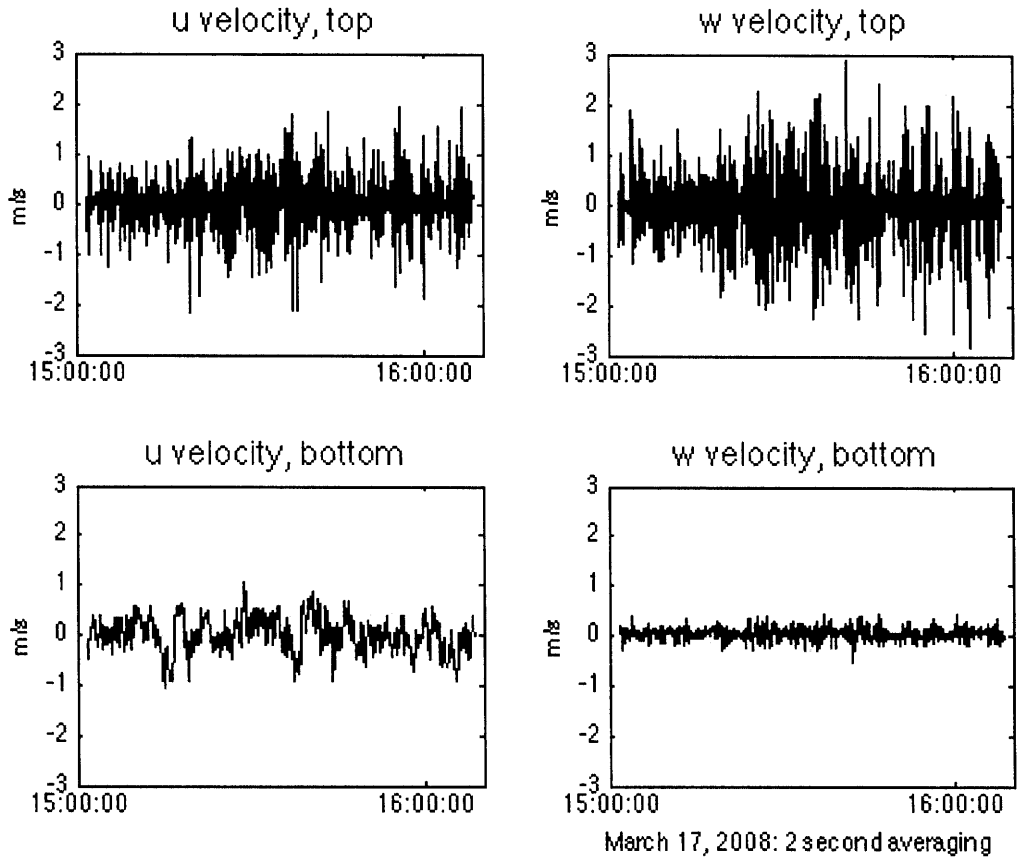

Figure 5-7: Two-second-averaged wind components above the canopy ("top") and ground level ("bottom") for 3/17/08.

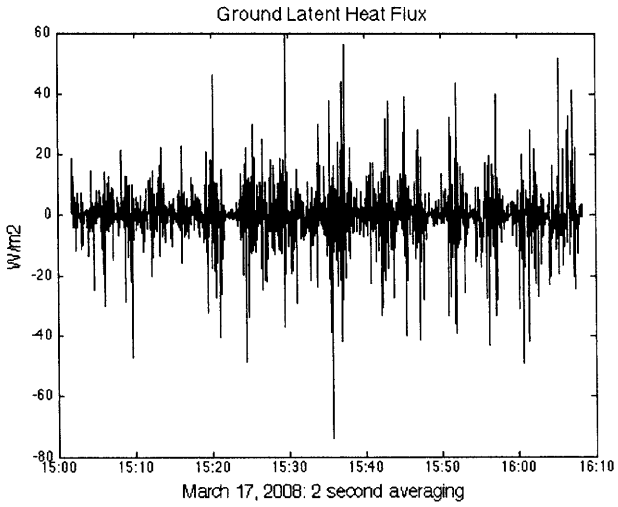

Figure 5-8: Two-second-averaged ground-level latent heat flux for 3/17/08.

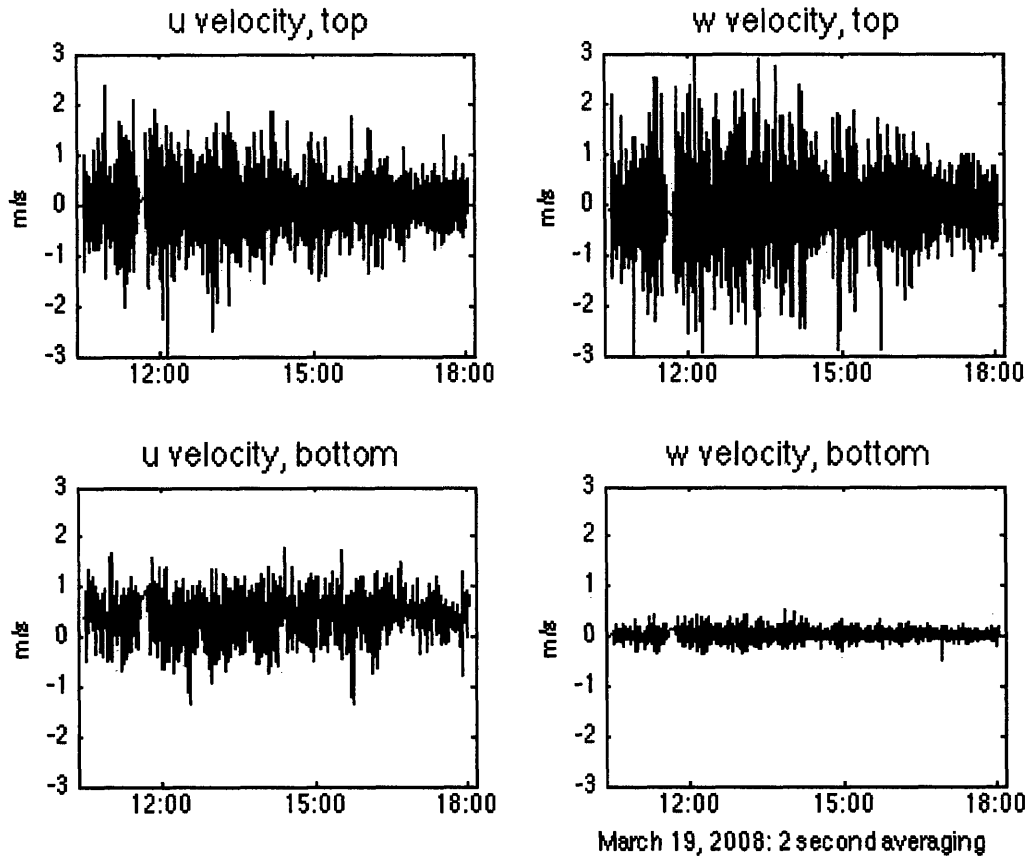

Figure 5-9: Two-second-averaged wind components above the canopy ("top") and ground level ("bottom") for 3/19/08.

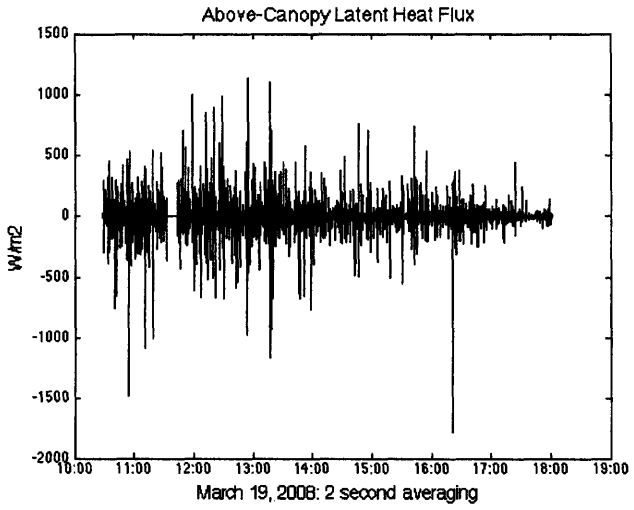

Figure 5-10: Two-second-average above-canopy latent heat flux for 3/19/08.

The high frequency (10Hz) eddy covariance data without averaging were collected on March 20, 2008. Values of wind velocity components and temperature were sampled both above the canopy and at ground level, and concentrations of H_2O and CO_2 were sampled above the canopy only. The raw data are plotted in Figures 5-11 through 5-15. As in the plots of averaged data from March 17-19, Figure 5-11 shows that horizontal wind velocity above the canopy is considerably larger than that at ground level, although ground-level horizontal velocity is still significant. Also as above, vertical velocity above the canopy is significantly larger than vertical velocity at ground level (Figure 5-12), although more variation can be seen in the unaveraged 10Hz values than in the averaged values from Figures 5-7 and 5-9. Latent heat flux above the canopy shows instantaneous ($\overline{wr}\frac{\lambda}{\rho_w}$) peaks of magnitude up to 10^5 W/m^2 (Figure 5-13), and instantaneous sensible heat flux ($\overline{wT}\rho_{atm}C_p$) above the canopy shows peaks on the order of 10^4 W/m^2, while sensible heat flux below the canopy is much smaller, on the order of 10 W/m^2 (Figure 5-14). Instantaneous momentum flux ($\overline{uw}$) is also larger above the canopy than at ground level (Figure 5-15), although the difference is much smaller than for the latent and sensible heat fluxes.

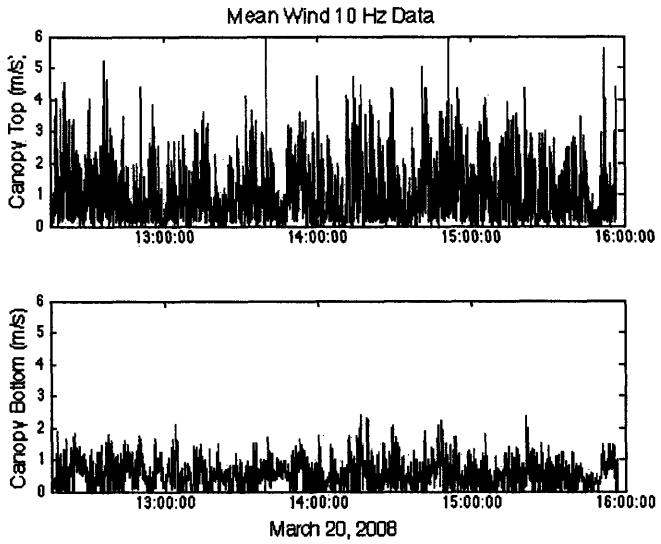

Figure 5-11: Raw 10Hz values of horizontal wind above canopy ("top") and at ground level ("bottom").

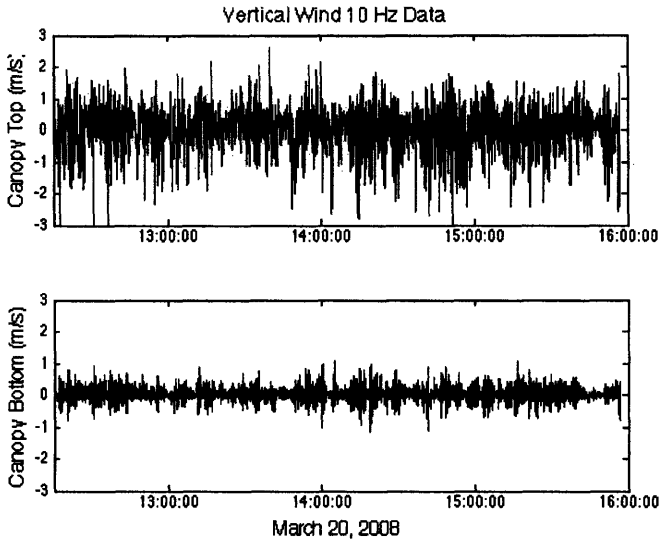

Figure 5-12: Raw 10Hz values for vertical wind velocity at top and bottom of canopy.

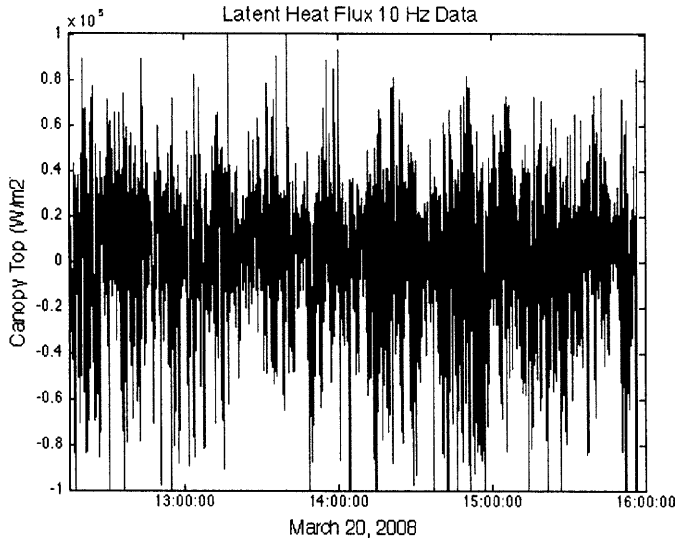

Figure 5-13: Raw 10Hz values of latent heat flux at top of canopy.

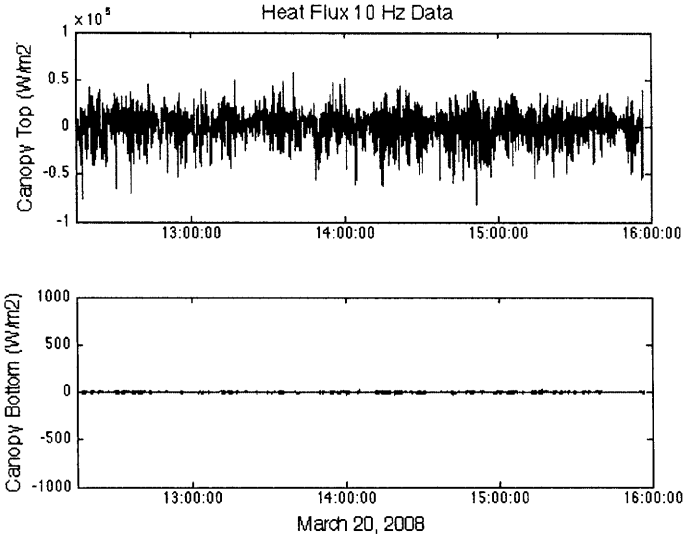

Figure 5-14: Raw 10Hz values of sensible heat flux at top and bottom of canopy. Note the different y-axis scales.

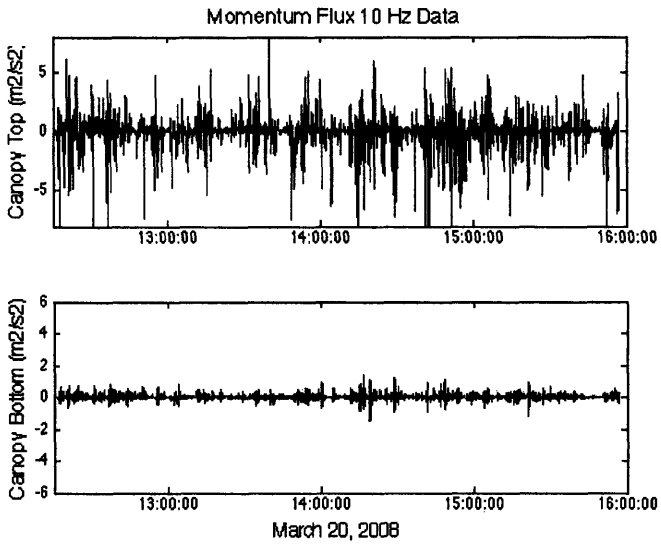

Figure 5-15: Raw 10Hz values of momentum flux at top and bottom of canopy.

The high frequency values of wind components, temperature, and fluxes from March 20 were also averaged over a variety of periods in order to assess the effect of averaging period choice. Means and deviations from the mean were calculated for periods of two seconds, thirty seconds, one minute, two minutes, five minutes, ten minutes, and thirty minutes. Figure 5-16 shows the averaged values of mean horizontal wind for these different periods, and Figure 5-17 shows the averaged vertical turbulent fluxes ($\overline{w'r'}\frac{\lambda}{\rho_w}$, $\overline{w'T'}\rho_{atm}C_p$, and $\overline{u'w'}$) using the different periods. The progressively longer averaging periods remove the oscillations around a mean value but do not shift the magnitude of that mean value.

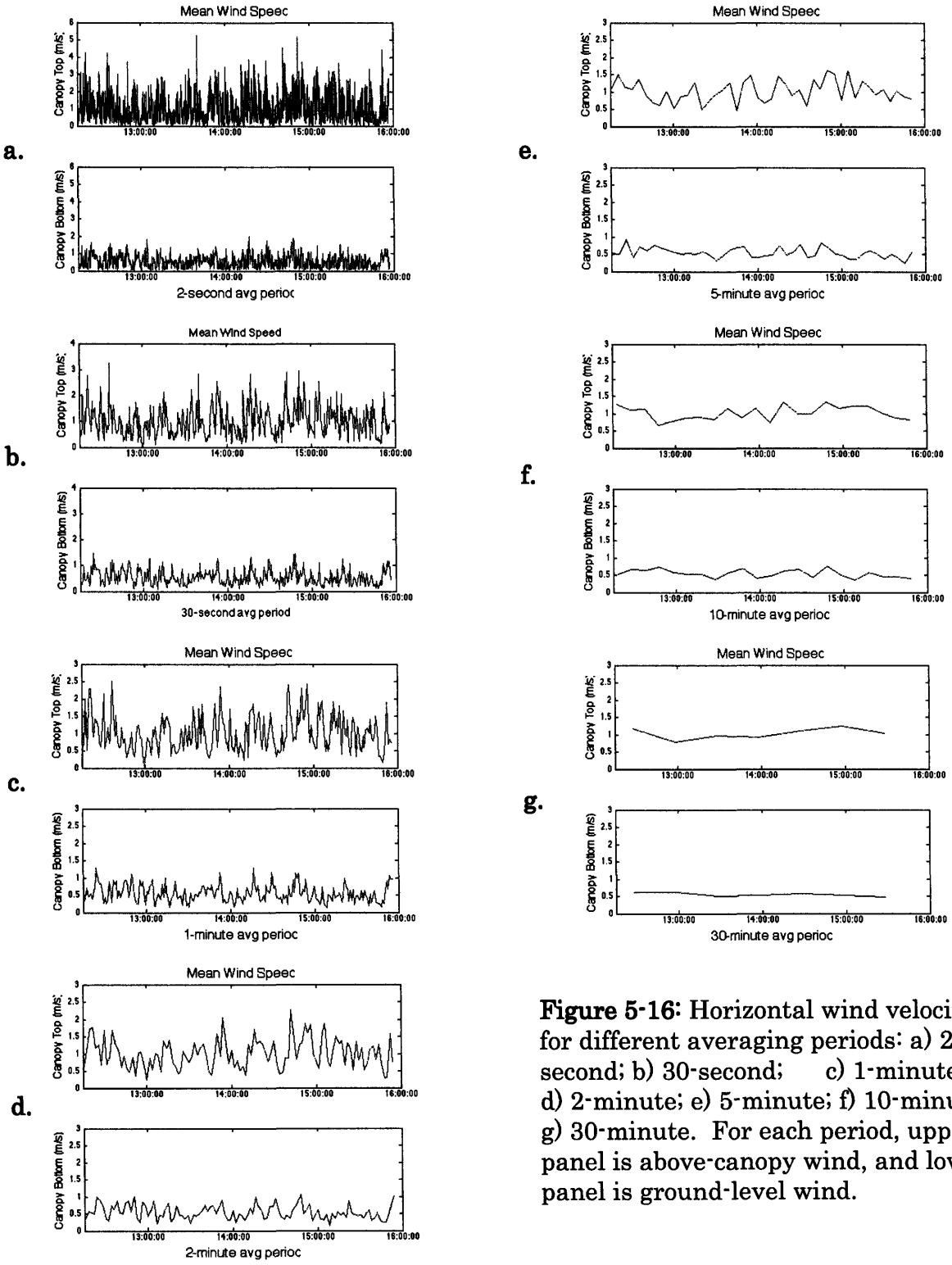

Figure 5-16: Horizontal wind velocity for different averaging periods: a) 2-second; b) 30-second; c) 1-minute; d) 2-minute; e) 5-minute; f) 10-minute; g) 30-minute. For each period, upper panel is above-canopy wind, and lower panel is ground-level wind.

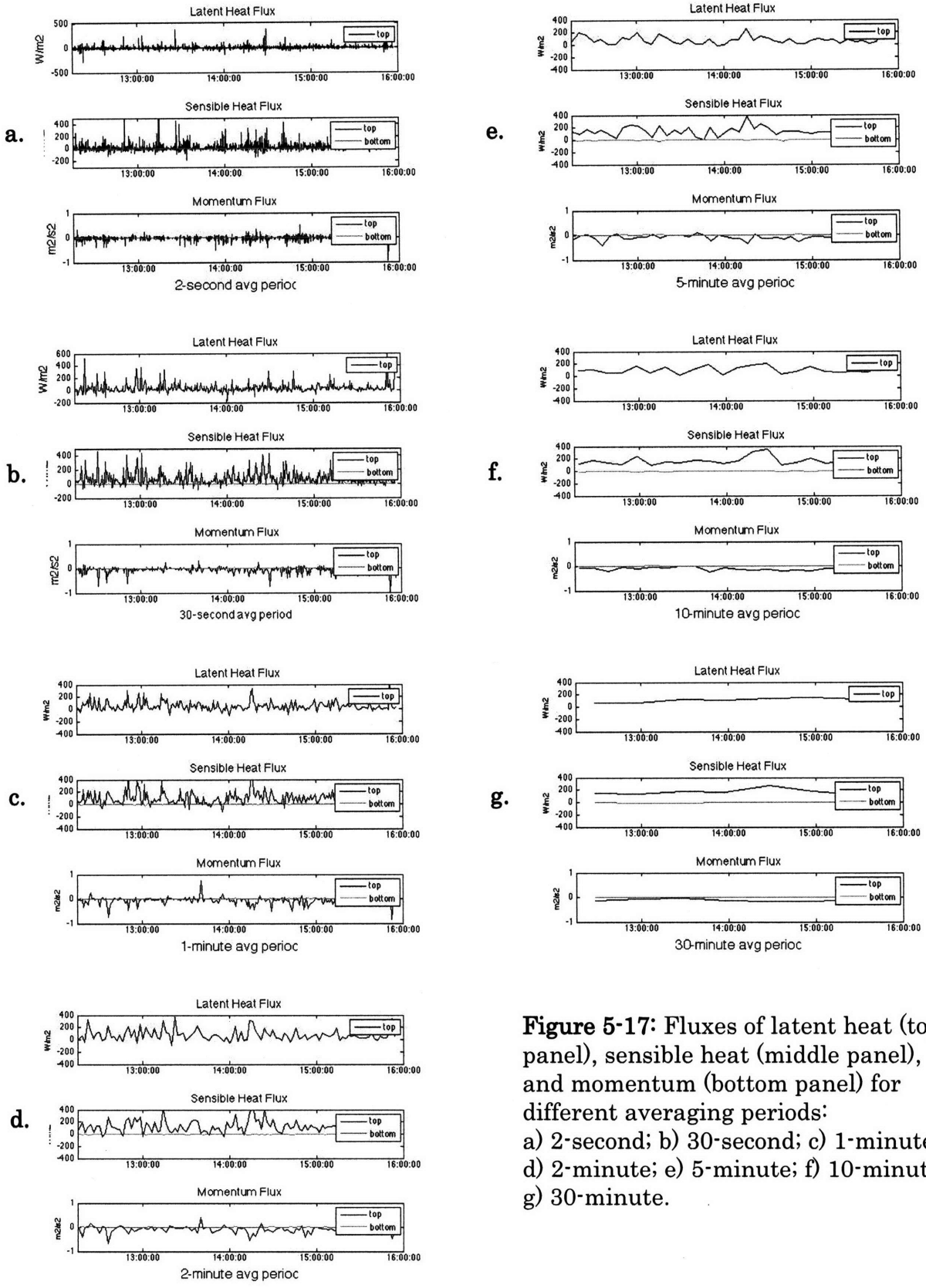

Figure 5-17: Fluxes of latent heat (top panel), sensible heat (middle panel), and momentum (bottom panel) for different averaging periods:
a) 2-second; b) 30-second; c) 1-minute; d) 2-minute; e) 5-minute; f) 10-minute; g) 30-minute.

Figure 5-18 compares the cumulative latent heat transported during the measurement period as calculated using different the averaging periods. Cumulative latent heat energy (E, in joules) transported per m^2 is

$$E = (LE)(\Delta t) \tag{5-6}$$

where LE is latent heat flux (W/m^2) and Δt is the measurement time period(s). Figure 5-18 shows that the cumulative latent heat energy transferred per unit area is fairly constant for all averaging periods tested. This result indicates that the choice of averaging period for eddy covariance analysis, while somewhat arbitrary, may not affect calculated values of total mass and energy transfer greatly.

The difference between $\overline{wr}$ (dash-dotted line) and $\overline{w'r'}$ (solid line) in Figure 5-18 is significant and indicates that $\overline{wr}$ is not zero, as eddy covariance theory assumes (see Section 4.1.1 and Equation 4-4), but rather is quite large. This large value of $\overline{wr}$ probably comes from a relatively constant, non-zero average vertical wind induced by the complex topography.

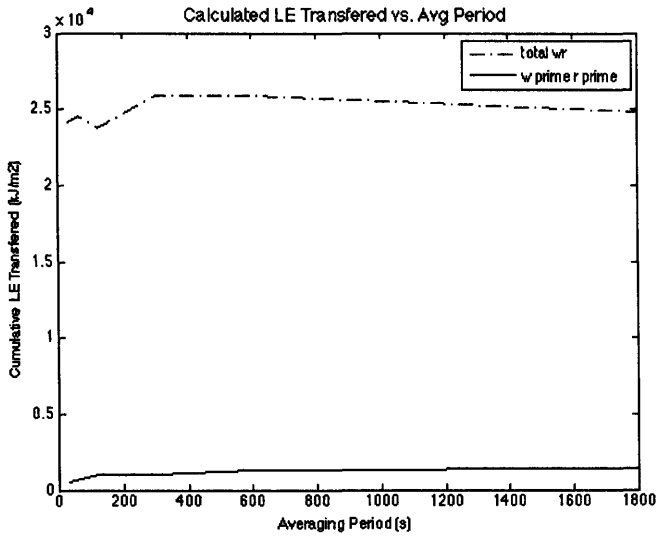

Figure 5-18: Latent heat flux integrated over time versus averaging period used to calculate flux.

5.2 Modeling Results

Resistance and ground latent heat flux were calculated for the four model formulations tested and are plotted as functions of canopy height and density in Figures 5-19 to 5-26. The first conceptual model tested was the rough wall boundary layer eddy diffusivity currently found in the ED model (Equation 2-19). With this formulation, aerodynamic resistance to soil evaporation (Figure 5-19) decreases with increasing canopy height, and latent heat flux from the ground correspondingly increases with canopy height (Figure 5-20). Figures 5-19 and 5-20 are the same as Figures 2-6 and 2-7.

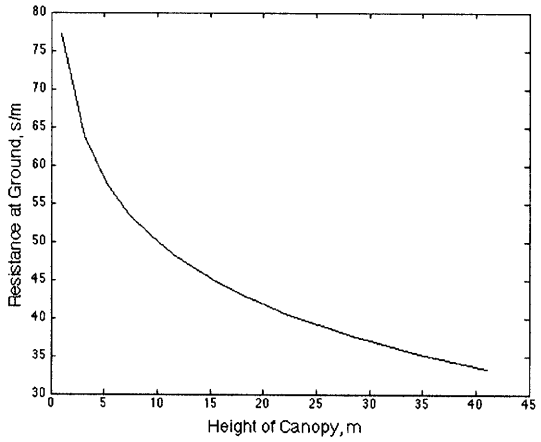

Figure 5-19: Resistance as a function of canopy height, calculated by current ED formulation.

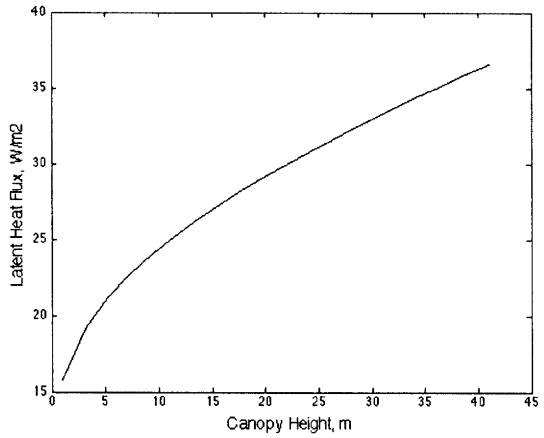

Figure 5-20: Ground latent heat flux as a function of canopy height, calculated with current ED formulation.

In the second modeling test, the same rough wall boundary layer formulation of resistance (Equation 2-19) was used, and the eddy diffusivity extinction coefficient, *a*, was varied. The current ED model uses an *a* value of 2.5, but in this test, resistance and ground latent heat flux were calculated for *a* values of 0.5, 1.5, 2.5, 3.5, 4.5, and 5.5. Higher values of *a* give higher values of resistance (Figure 5-21) and lower values of ground latent heat flux (Figure 5-22). Resistance and latent heat flux as a function of canopy height follow the same form as in Figures 5-19 and 5-20 because they use the same resistance formulation (Equation 2-19), and only the extinction coefficient varies.

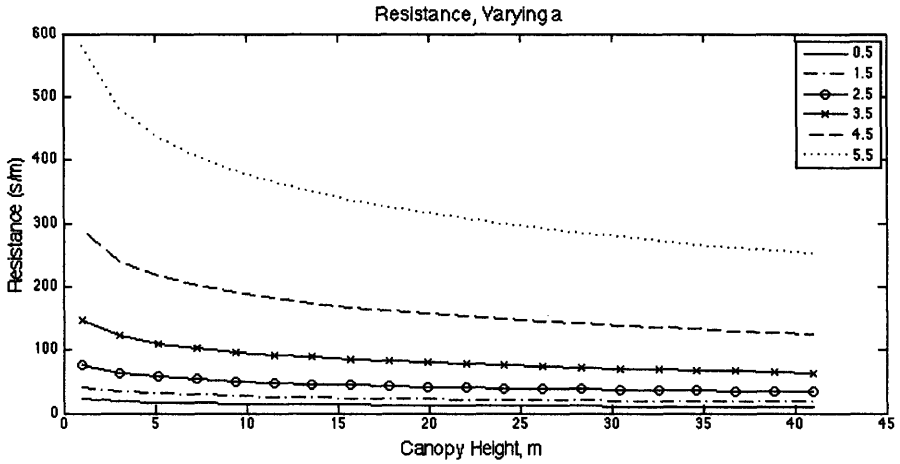

Figure 5-21: Resistance as a function of canopy height, calculated with Equation 2-19 and varying the extinction coefficient, *a*, from 0.5 to 5.5.

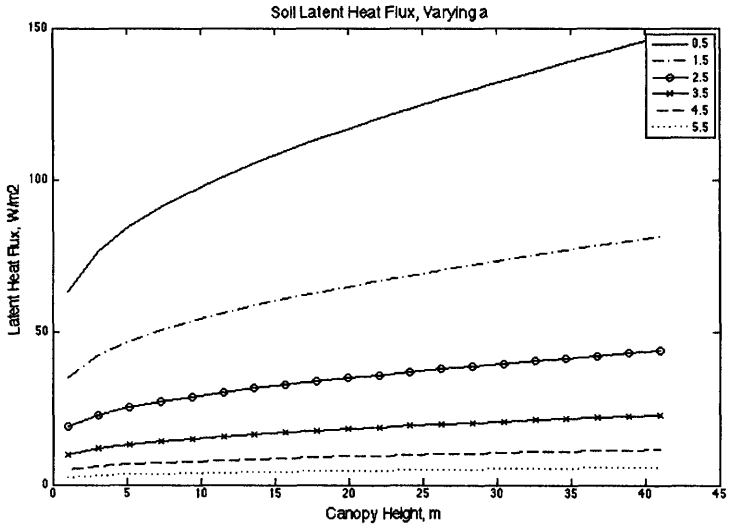

Figure 5-22: Ground latent heat flux as a function of canopy height, calculated with Equation 2-19 and varying the extinction coefficient, *a*, from 0.5 to 5.5.

In the third modeling test, resistance and ground latent heat flux were calculated using the mixing-layer-diffusivity resistance derived from Harman and Finnigan (2007) and defined in Equation 4-20. Resistance and latent heat flux are plotted as functions of canopy height and LAI in Figures 5-23 and 5-24. Resistance increases with increasing LAI (and thus with increasing canopy density) (Figure 5-23), and ground latent heat flux decreases with increasing LAI (Figure 5-24).

Ground latent heat flux becomes unreasonably high for tall canopies (over 10m) with low LAI (less than 2), but canopies with such low LAI are generally either short, such as grass, or are extremely sparse, to such a degree that the model's formulation of bare ground evaporation would take over.

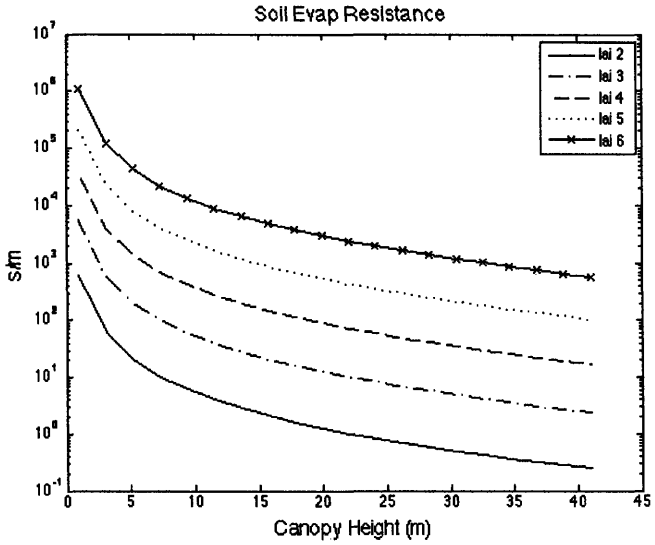

Figure 5-23: Resistance as a function of canopy height and LAI, calculated with the Harman and Finnigan formulation (Equation 4-20). Note: y-axis in log scale.

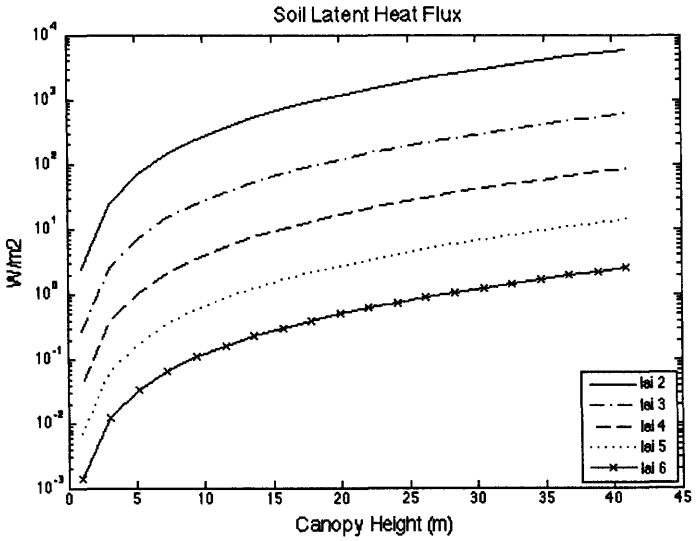

Figure 5-24: Ground latent heat flux as a function of canopy height and LAI, calculated with the Harman and Finnigan formulation (Equation 4-20). Note: y-axis in log scale.

The fourth modeling test employs the cutoff for vortex penetration to ground, setting soil evaporation equal to zero when the ratio of vortex penetration to canopy height is less than one. When the ratio of vortex penetration depth to canopy height is greater than or equal to one, ground latent heat flux is turned on and is calculated using the resistance formulation based on the current ED model formulation (Equation 2-19). Two versions of this model were tested: one where soil evaporation is turned off for canopies with LAI greater than ~1 (Equation 4-22), and one where the cutoff occurred for canopies with LAI greater than 4 (Equation 4-23). The results from Equation 4-22 are plotted in Figure 5-25, and the results from Equation 4-23 are plotted in Figure 5-26.

Figure 5-26 shows that the behavior of the rough wall boundary resistance formulation differs for values of LAI on either side of 1.92. Above LAI of 1.92, the resistance to soil evaporation equals the vegetation resistance. Below LAI of 1.92, the total resistance to soil evaporation becomes a linear combination of the vegetation resistance and a bare soil resistance, in proportion to the ground cover ratio, which depends on LAI.

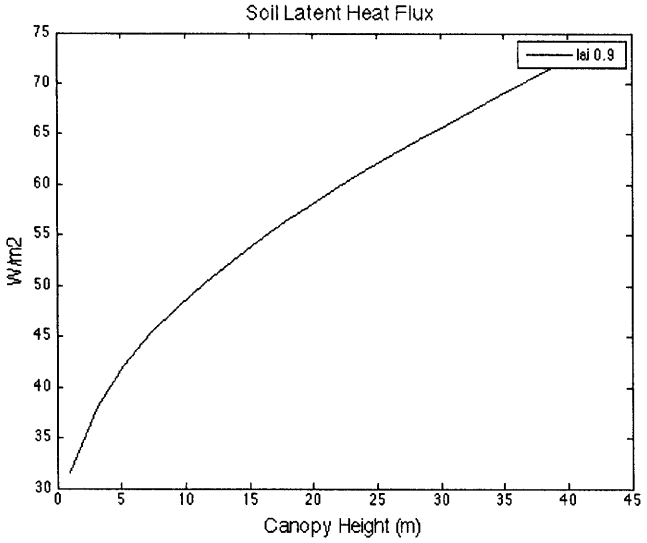

Figure 5-25: Ground latent heat flux as a function of canopy height with LAI = 0.9, using the vortex-penetration cutoff model with cutoff at LAI=0.92. For LAI less than or equal to 0.92, ground latent heat flux is calculated with the rough wall boundary resistance formulation (Equation 2-19); for LAI greater than 0.92, ground latent heat flux is set to zero.

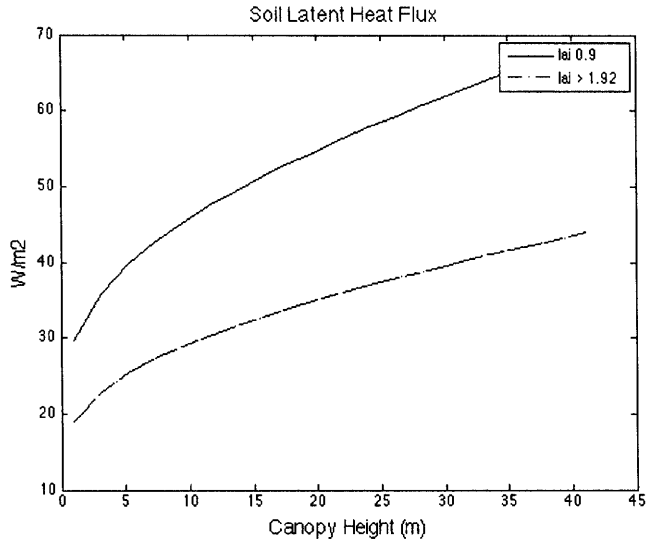

Figure 5-26: Ground latent heat flux as a function of canopy height and LAI, using the vortex-penetration cutoff model with cutoff at LAI=4. For LAI less than or equal to 4, ground latent heat flux is calculated with the rough wall boundary resistance formulation (Equation 2-19); for LAI greater than 4, ground latent heat flux is set to zero. See text for explanation of behavior around LAI=1.92.

Chapter 6:
Discussion and Conclusions

This study integrates a review of the literature with results from field and modeling experiments in order to investigate scalar transport in vegetation canopies and assess options for its parameterization in a computationally demanding land surface model.

A review of literature on turbulent flow and transport through canopies showed that canopy flow more closely resembles a plane mixing layer than a rough wall boundary layer. As in mixing layers, intermittent coherent structures of canopy scale characterize canopy flows and dominate the transport of scalars and momentum. Because these structures are of the same scale as the canopy, counter-gradient flows can occur locally within the canopy, and the eddy diffusivity turbulence closure, or K-theory, fails.

Both previous field studies and this study's eddy covariance field results indicate that evaporation from the soil is negligible below tall, dense canopies. Hydrologic observations of evaporation from rainforests using the Penman-Monteith-Rutter model found that the sum of measured transpiration and interception loss is very close to estimates of total evaporation estimated from independent water balance measurements (Shuttleworth 1988, Schellekens et al. 2000). The agreement of these independent estimates of total evaporation supports the assumption by both Shuttleworth and Schellekens et al. that evaporation from the soil below dense forests is negligible.

In the present study, eddy covariance measurements made in a dense rainforest show that turbulent velocities and fluxes at the ground level were at least an order of magnitude lower than those at the top of the canopy. These results further indicate that evaporation from soil below a tall dense canopy is only a very small component of total evapotranspiration. Unfortunately, the field measurements of latent heat flux cannot be compared quantitatively to modeled latent heat flux because of the complex topography. The varied terrain at the field

site introduces advection terms that violate the assumptions of the eddy covariance method, which say that lateral advection is zero because of horizontal homogeneity and vertical advection is zero because the mean vertical velocity is zero. The terrain of this field site is quite inhomogeneous horizontally, and time-integrated fluxes (Figure 5-18) demonstrate that the mean vertical velocity is nonzero and indeed is quite large. Nonetheless, the measured wind velocities and fluxes illustrate qualitatively that transport of momentum and scalars at the ground below a tall, dense canopy is much smaller than at the top of the canopy.

Empirical observations indicate, then, that the model formulation for water vapor transport through canopies should take into account both height and density of the canopy. The formulation should predict negligible soil evaporation for high, dense canopies and significant soil evaporation for low, sparse canopies. At the same time, for the purpose of computational efficiency in the large ED model, the evaporation formulation should be mathematically straightforward and solvable algebraically without iterative numerical techniques. Several mathematical formulations of canopy scalar transport were evaluated according to these criteria.

Scalar transport through vegetation can be predicted with Lagrangian models such as those discussed in Raupach (1988) and Siqueira et al. (2000). These models track the motions of particles of mass and superimpose the concentrations due to multiple near-field and far-field sources. They resolve transport on a fine scale without the assumption of fine-grained turbulence that K-theory makes. However, Lagrangian models require the calculation of the particle transition probability, which is very computationally demanding and thus infeasible for the ED model.

Second-order Eulerian closures, such as that discussed in Siqueira et al. (2000), provide another method for predicting scalar transport. This control-volume approach uses classical equations for momentum and mass conservation and transport, giving a second-order partial differential equation with unknown terms that are parameterized with a closure approximation. While second-order Eulerian closures are less computationally demanding than the stochastic probability

distributions in Lagrangian models, they still require iterative numerical methods to solve the second-order PDE, making them also infeasible for large-scale modeling applications such as the ED model.

Eddy diffusivity formulations provide a first-order closure to the momentum and mass conservation equations. While Raupach (1988) and others have shown that K-theory fails to describe local transport within the canopy, it does provide a simple analytical closure that meets the computational requirements of the ED model. Thus, different formulations for evaporation resistance using eddy diffusivity were tested in constrained numerical experiments.

The first and second modeling experiments tested the current ED resistance formulation, which is based on rough wall boundary layer flow. The second modeling experiment varied *a*, the eddy diffusivity extinction coefficient. Higher values of *a* gave higher values of resistance and thus lower values of soil evaporation. The value of *a* could thus be made to vary with canopy density or vegetation type in order to give low soil evaporation below dense canopies and high soil evaporation below sparse canopies. However, the choice of *a* values for each canopy density or vegetation type would be arbitrary, because of lack of data for calibration, and not physically-based. This option for modeling subcanopy evaporation is thus not ideal.

The third modeling experiment incorporated the mixing layer formulation of canopy flow into the calculation of eddy diffusivity. The unified model of canopy flow developed by Harman and Finnigan (2000) predicts a vertical profile of mean velocity that includes the influence of the canopy on the flow. Their theory takes both the height and the density of the canopy into account in the calculations of the mixing length and velocity profile. Harman and Finnigan do caution that their theory cannot describe profiles of scalars without considering the local distribution of sources and sinks within the canopy, and while they do not themselves calculate eddy diffusivity, their equations for mean wind and mixing length can be substituted into a standard definition of eddy diffusivity. The modeling experiment results give values of resistance that increase with increasing canopy density and

decrease with increasing canopy height. Accordingly, ground latent heat flux decreases with increasing canopy density and increases with increasing canopy height. For tall canopies with low LAI, the ground latent heat flux becomes unreasonably high, but since canopies of such tall height and low LAI do not exist in the ED model, those unreasonable values will not actually come into play. For vegetation types relevant to the ED model (grass pasture with height of 1 to 2 meters and LAI of ~2; rainforest with height of ~40 meters and LAI of 6 or greater), this formulation gives reasonable results: about 10 W/m^2 for grass pasture and about 1 W/m^2 for tall forest. The mixing layer eddy diffusivity formulation of evaporation resistance, then, is computationally straightforward and predicts evaporation rates that align with field observations, increasing with decreasing canopy density and height. This formulation, while somewhat physically inaccurate, meets many of the criteria for inclusion in the ED model.

Finally, the fourth modeling experiment tested a threshold cutoff for soil evaporation based on the penetration depth of the coherent mixing layer vortices. Since these vortices are responsible for the vast majority of scalar and momentum transport, it is argued that if they do not penetrate to the ground, scalar transport from the ground can be ignored. Following Nepf et al. (2007), the leaf area index, drag coefficient, and a constant of turbulence statistics define the ratio of vortex penetration depth to canopy height. Equations 4-22 and 4-23 are two different versions of the vortex penetration cutoff. For values of LAI greater than the cutoff, the ratio of penetration depth to canopy height is less than one, so vortices do not penetrate to the ground, and soil evaporation is turned off in this model formulation. For LAI values less than or equal to the cutoff, vortices do penetrate to the ground, and evaporation resistance is calculated using the mixing layer eddy diffusivity formulation.

It remains unclear which version of the vortex penetration cutoff model is more accurate for terrestrial canopies. Profiles of momentum fluxes in different types of canopies, from short grass-like crops to tall forests (see Figure 3-1), show that the momentum flux goes to zero before reaching the ground level. This

suggests that coherent vortices may not penetrate to the ground for any of the canopies profiled. If this is true for grass pasture in the Amazon as well, it supports the use of a vortex cutoff of LAI=0.92, above which no ground latent heat flux occurs. On the other hand, some experimental data, such as Moreira et al. (1997), suggests that soil evaporation contributes significantly to total evapotranspiration over short, grass-like vegetation. Similarly, a study by Johnsson and Jansson (1991) that found that soil evaporation contributed between 23 and 60 percent of total evapotranspiration for barley and grass fields. Nevertheless, conclusive data on the magnitude of soil evaporation from grass pastures is lacking, making validation of one or the other of the vortex penetration cutoff models difficult.

Of the models tested, the vortex penetration threshold model is the most faithful to the physical processes occurring in canopy flows. When coupled with an eddy diffusivity resistance formulation based on the rough wall boundary layer model (Equation 2-19), it predicts the desired relationship between canopy density and soil evaporation, giving significant soil evaporation for sparse canopies and negligible soil evaporation for dense canopies. Moreover, this formulation can feasibly be incorporated into a regional-scale model like ED because it is computationally simple. As such, it is a good option for adjusting the formulation of soil evaporation in the ED model. This author recommends incorporating into ED the vortex penetration model, using a soil evaporation cutoff of LAI=0.92 in keeping with the (albeit limited) direct measurements of soil evaporation from grass. Future work should seek to quantify soil evaporation from canopies of various densities and heights, and these measurements should be used to validate this evaporation formulation in terrestrial canopies.

References:

Achard, F., H.D. Eva, H.-J. Stibig, P. Mayaux, J. Gallego, T. Richards, J.-P. Malingreau. 2002. Determination of deforestation rates of the world's humid tropical forests. *Science* 297(5583):999-1002.

Baldocchi, D.D. 2003. Assessing the eddy covariance technique for evaluating carbon dioxide exchange rates of ecosystems: past, present and future. *Global Change Biology* 9:479-492.

Bonan, G.B. 1996. A Land Surface Model (LSM version 1.0) for Ecological, Hydrological, and Atmospheric Studies: Technical Description and User's Guide. NCAR Technical Note, NCAR/TN-417+STR. Climate and Global Dynamics Division, National Center for Atmospheric Research, Boulder, CO.

Chagnon, F.J.F., R.L. Bras, J. Wang. 2004. Climatic shift in patterns of shallow clouds over the Amazon. *Geophysical Research Letters* 31, L24212.

Chagnon, F.J.F., R.L. Bras. 2005. Contemporary climate change in the Amazon. *Geophysical Research Letters* 32, L13703.

Chagnon, F.J.F., R.L. Bras, J. Wang, E. Williams, A.K. Betts, N.O. Renno, L.A.T. Machado, R. Knox, G. Bisht. 2007 (submitted). Do clouds follow deforestation over the Amazon? *Science*.

Crow, T.R. 1980. A rainforest chronicle: a 30 year record of change in structure and composition at El Verde, Puerto Rico. *Biotropica* 12(1):42-55.

Eltahir, E.A.B., R.L. Bras. 1993. On the response of the tropical atmosphere to large-scale deforestation. *Quarterly Journal of the Royal Meteorological Society* 119(512):779-793.

Eltahir, E.A.B., R.L. Bras. 1994a. Precipitation recycling in the Amazon basin. *Quarterly Journal of the Royal Meteorological Society* 120(518):861-880.

Eltahir, E.A.B., R.L. Bras. 1994b. Sensitivity of regional climate to deforestation in the Amazon Basin. *Advances in Water Resources* 17(1-2):101-115.

Finnigan, J. 2000. Turbulence in plant canopies. *Annual Review of Fluid Mechanics* 32:519-571.

Harman, I.N., J.J. Finnigan. 2007. A simple unified theory for flow in the canopy and roughness sublayer. *Boundary-Layer Meteorology* 123:339-363.

Instituto Nacional de Pesquisas Espaciais (INPE). 2003. Monitoring of the Brazilian Amazon forest by satellite 2001-2002. Tech. rep., São José Dos Campos. http://sputnik.dpi.inpe.br:1910/col/dpi.inpe.br/lise/2002/06.12.13.16/doc/Pag-07.htm

Johnsson, H., R.E. Janssen. 1991. Water balance and soil moisture dynamics of field plots with barley and grass ley. *Journal of Hydrology* 129(1/4):149-173.

Katul, G. 1998. An investigation of higher-order closure models for a forested canopy. *Boundary-Layer Meteorology* 89(1):47-74.

Katul, G.G., J.J. Finnigan, D. Poggi, R. Leuning, S.E. Belcher. 2006. The influence of hilly terrain on canopy-atmosphere carbon dioxide exchange. *Boundary-Layer Meteorology* 118:189-216.

LTER. 2008. Luquillo Long Term Ecological Research Data Sets Documentation Form. http://luq.lternet.edu/data/lterdb90/metadata/lterdb90.htm. Accessed May 3, 2008.

Medvigy, D.M. The state of the regional carbon cycle: Results from a constrained coupled ecosystem atmosphere model. PhD dissertation. Division of Engineering and Applied Science, Harvard University, 2006.

Monteith, J.L. 1965. Evaporation and environment. *Symposia of the Society of Experimental Biology* 19:205-234.

Moorcroft, P.R., G.C. Hurtt, S.W. Pacala. 2001. A method for scaling vegetation dynamics: the ecosystem demography model (ED). *Ecological Monographs* 71(4):557-585.

Moreira, M.Z., L.D.S.L. Sternberg, L.A. Martinelli, R.L. Victoria, E.M. Barbosa, L.C.M. Bonates, D.C. Nepstad. 1997. Contribution of transpiration to forest ambient vapor based on isotopic measurements. *Global Change Biology* 3:439-450.

Nepf, H., M. Ghisalberti, B. White, E. Murphy. 2007. Retention time and dispersion associated with submerged aquatic canopies. *Water Resources Research* 43:W04422.

Nobre, C.A., P.J. Sellers, J. Shukla. 1991. Amazonian deforestation and regional climate change. *Journal of Climate* 4:957-988.

Pielke, R.A., W.R. Cotton, R.L. Walko, C.J. Tremback, W.A. Lyons, L.D. Grasso, M.E. Nicholls, M.D. Moran, D.A. Wesley, T.J. Lee, J.H. Copeland. 1992. A comprehensive meteorological modeling system – RAMS. *Meteorology and Atmospheric Physics* 49:69-91.

Pielke Sr., R.A. 2001. Influence of the spatial distribution of vegetation and soils on the prediction of cumulus convective rainfall. *Reviews of Geophysics* 39(2):151-177.

Poggi, D., G.G. Katul. 2007. Turbulent flows on forested hilly terrain: the recirculation region. *Quarterly Journal of the Royal Meteorological Society* 133:1027-1039.

RAMS. 2007. An Introduction. http://rams.atmos.colostate.edu/rams-description.edu. Accessed May 3, 2008.

Raupach, M.R. Canopy transport processes. In *Flow and Transport in the Natural Environment: Advances and Applications*, ed. W.L. Steffen and O.T. Denmead. Berlin: Springer-Verlag, 1988.

Roberts, J.M., J.H.C. Gash, M. Tani, L.A. Bruijnzeel. 2005. Controls on evaporation in lowland tropical forest. In *Forests, Water and People in the Humid Tropics*, ed. M. Bonell and L.A. Bruijnzeel. Cambridge University Press.

Rutter, A.J., A.J. Morton, P.C. Robbins. 1975. A predictive model of rainfall interception in forests. II. Generalization of the model and comparison with observations in some coniferous and hardwood stands. *Journal of Applied Ecology* 12(1):367-380.

Schellekens, J., L.A. Bruijnzeel, F.N. Scatena, N.J. Bink, F. Holwerda. 2000. Evaporation from a tropical rain forest, Luquillo Experimental Forest, eastern Puerto Rico. *Water Resources Research* 36(8):2183-2196.

Shukla, J., C. Nobre, P. Sellers. 1990. Amazon deforestation and climate change. *Science* 247(4948):1322-1325.

Shuttleworth, W.J. 1988. Evaporation from Amazonian rainforest. *Proceedings of the Royal Society of London* B 233:321-346.

Stull, R.B. *Meteorology for Scientists and Engineers, Second Edition.* Brooks/Cole Thomson Learning, 2000.

Wang J., R.L. Bras, E.A.B. Eltahir. 2000. The impact of observed deforestation on the mesoscale distribution of rainfall and clouds in Amazonia. *Journal of Hydrometeorology* 1:267-286.

Weaver, C.P., R. Avissar. 2001. Atmospheric disturbances caused by human modification of the landscape. *Bulletin of the American Meteorological Society* 82(2):269-281.

Werth, D., R. Avissar. 2002. The local and global effects of Amazonian deforestation. *Journal of Geophysical Research* 107(D20).

Wilson, J.D. 1988. A second-order closure model for flow through vegetation. *Boundary-Layer Meteorology* 42(4):371-392.

Appendix A:

Wiring Diagrams for Field Instrumentation

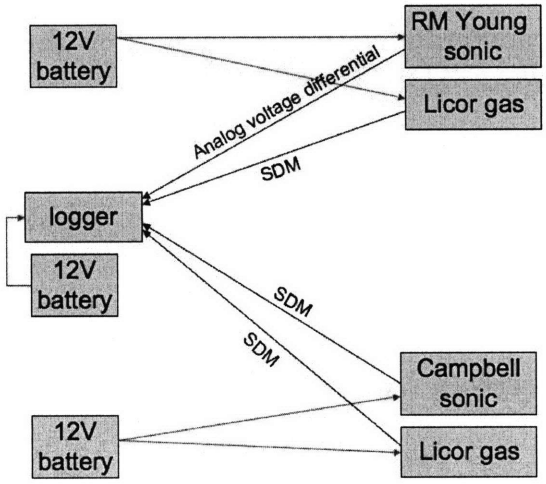

A-1: Wiring connections between instruments, logger, and batteries.

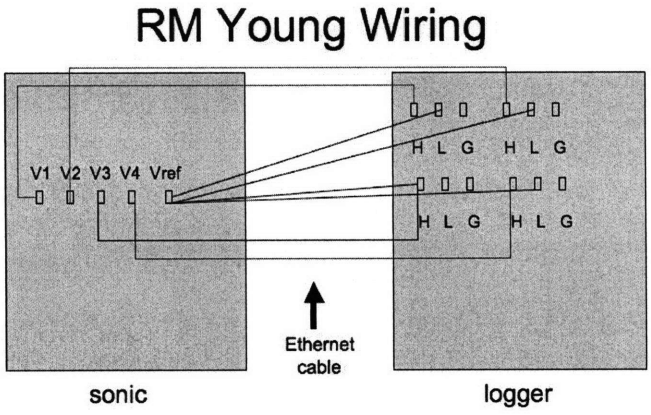

A-2: Wiring between RM Young 81000 sonic anemometer and data logger. The V1, V2, V3, and V4 on the RM Young were each connected to "high" on a different voltage differential port on the logger. Vref was connected to "low" on each of the voltage differential ports.

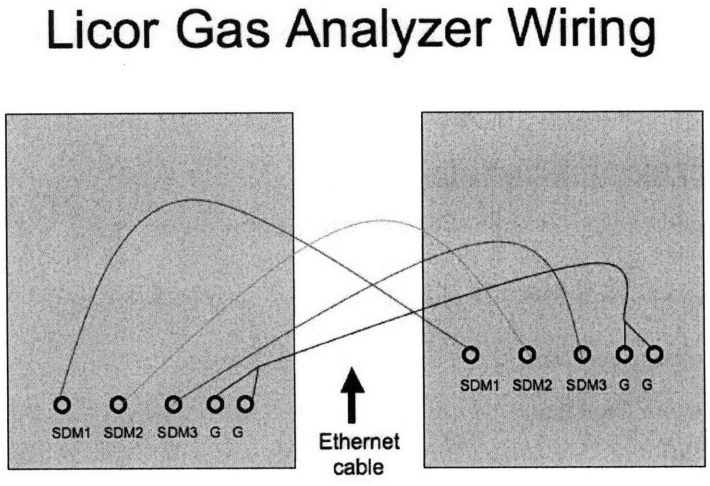

A-3: Wiring between Licor 7500 gas analyzer and data logger. The SDM1 port on the Licor control board was connected to the SDM1 port on the data logger, and so on for SDM2, SDM3, and ground.

Appendix B:

Data Logger Programs

Two-second averaging program:

```
'CR5000 Series Datalogger
'program author: Percy Link

'Declare Public Variables

Public wind_cs(5)   'Ux,Uy,Uz,Tson,Diag
Public licor_cs(3)  'CO2,H2O,Press
Public wind_rm(5)   'Ux,Uy,Uz,Tson,Diag
Public licor_rm(3)  'CO2,H2O,Press

Public rthetime
Public rtime(9)
Public Batt_Volt
Public DSec


Public wc_inst_rm
Public wc_inst_cs
Public wr_inst_rm
Public wr_inst_cs


Public wc_integ_rm
Public wc_integ_cs
Public wr_integ_rm
Public wr_integ_cs
Public w_integ_rm
Public w_integ_cs
Public u_integ_rm
Public u_integ_cs
Public v_integ_rm
Public v_integ_cs
Public c_integ_rm
Public c_integ_cs
Public r_integ_rm
Public r_integ_cs

Public w_avg_rm
Public w_avg_cs
Public u_avg_rm
Public u_avg_cs
Public v_avg_rm
Public v_avg_cs
Public c_avg_rm
Public c_avg_cs
Public r_avg_rm
Public r_avg_cs
Public wr_avg_rm
Public wr_avg_cs
Public wc_avg_rm
Public wc_avg_cs
```

```
Public count

Public ninteg

'RM Young Temporary Variables
Public wspeed
Public wdirection
Public welevation
Public stempK
Public stempC

Public Ux_rm
Public Uy_rm
Public Uz_rm

Units wspeed = m/s
Units wdirection = deg
Units welevation = deg
Units stempK = K
Units stempC = C

'Define Aliases

Alias wind_cs(1) = Ux_cs
Alias wind_cs(2) = Uy_cs
Alias wind_cs(3) = Uz_cs
Alias wind_cs(4) = T_sonic_cs
Alias wind_cs(5) = diagnostic_cs

Alias licor_cs(1) = co2_mg_m3_cs
Alias licor_cs(2) = h2o_g_m3_cs
Alias licor_cs(3) = pressure_cs

Alias licor_rm(1) = co2_mg_m3_rm
Alias licor_rm(2) = h2o_g_m3_rm
Alias licor_rm(3) = pressure_rm

Alias rTime(1) = Year       'assign the alias Year to rTime(1)
Alias rTime(2) = Month      'assign the alias Month to rTime(2)
Alias rTime(3) = Day        'assign the alias Day to rTime(3)
Alias rTime(4) = Hour       'assign the alias Hour to rTime(4)
Alias rTime(5) = Minute     'assign the alias Minute to rTime(5)
Alias rTime(6) = Second     'assign the alias Second to rTime(6)
Alias rTime(7) = uSecond    'assign the alias uSecond to rTime(7)
Alias rTime(8) = WeekDay    'assign the alias WeekDay to rTime(8)
Alias rTime(9) = Day_of_Year        'assign the alias Day_of_Year to rTime(9)

'CardOut( StopRing, Size )
'EndTable

DataTable(Metdata,TRUE,-1)

  Sample (1, Day_of_Year, IEEE4)
  Sample (1, Hour, IEEE4)
  Sample (1, Minute, IEEE4)
  Sample (1, DSec, IEEE4)
        Average(1,Batt_Volt,FP2,False)
EndTable

'Data tables for 2 second averages
DataTable (avg_2s_cs,TRUE,-1)
  Sample (1, Day_of_Year, IEEE4)
```

```
  Sample (1, Hour, IEEE4)
  Sample (1, Minute, IEEE4)
  Sample (1, DSec, IEEE4)
          Sample (1,u_avg_cs,IEEE4)
          Sample (1,v_avg_cs,IEEE4)
          Sample (1,w_avg_cs,IEEE4)
          Sample (1,c_avg_cs,IEEE4)
          Sample (1,r_avg_cs,IEEE4)
          Sample (1,wc_avg_cs,IEEE4)
          Sample (1,wr_avg_cs,IEEE4)
          'CardOut( StopRing, Size )
EndTable

DataTable (avg_2s_rm,TRUE,-1)
  Sample (1, Day_of_Year, IEEE4)
  Sample (1, Hour, IEEE4)
  Sample (1, Minute, IEEE4)
  Sample (1, DSec, IEEE4)
          Sample (1,u_avg_rm,IEEE4)
          Sample (1,v_avg_rm,IEEE4)
          Sample (1,w_avg_rm,IEEE4)
          Sample (1,c_avg_rm,IEEE4)
          Sample (1,r_avg_rm,IEEE4)
          Sample (1,wc_avg_rm,IEEE4)
          Sample (1,wr_avg_rm,IEEE4)
          'CardOut( StopRing, Size )
EndTable

'DataTable (inst_vars,TRUE,-1)
 ' Sample (1, Day_of_Year, IEEE4)
  'Sample (1, Hour, IEEE4)
  'Sample (1, Minute, IEEE4)
  'Sample (1, DSec, IEEE4)
          'Sample (1,Ux_rm,IEEE4)
          'Sample (1,Uy_rm,IEEE4)
          'Sample (1,Uz_rm,IEEE4)
          'Sample (1,Ux_cs,IEEE4)
          'Sample (1,Uy_cs,IEEE4)
          'Sample (1,Uz_cs,IEEE4)
          'Sample (1,wc_inst_rm,IEEE4)
          'Sample (1,wr_inst_rm,IEEE4)
          'Sample (1,wc_inst_cs,IEEE4)
  'Sample (1,wr_inst_cs,IEEE4)
          'CardOut( StopRing, Size )
'EndTable


'Main Program


BeginProg
                    'Start integrated flux, w, r, and c at zero
                    wc_integ_rm = 0.0
                    wc_integ_cs = 0.0
                    w_integ_rm = 0.0
                    w_integ_cs = 0.0
                    u_integ_rm = 0.0
                    u_integ_cs = 0.0
                    v_integ_rm = 0.0
                    v_integ_cs = 0.0
                    c_integ_rm = 0.0
```

```
		c_integ_cs = 0.0
		wr_integ_rm = 0.0
		wr_integ_cs = 0.0
		r_integ_rm = 0.0
		r_integ_cs = 0.0

		count = 0	'counter for averaging period.

	SDMSpeed (30)
	'Measure a CSAT3 and LI-7500 at 20 Hz.
'Timer(1,4,0)

Scan(200,msec,3,0)


	RealTime(rtime())

		'Get the CSAT3 data.
		CSAT3 (wind_cs(1),1,5,91,10)

		'Get the CS7500 (LI-7500) data that is connected
		'with the CSAT3
		'THE SDM ADDRESS OF THIS MUST BE CHANGED!!
		'CS7500 (licor_cs(1),1,7,5)
		'44 [g/mol] - molecular weight of carbon dioxide
		'0.018 [g/mmol] - molecular weight of water vapor
		'co2_mg_m3_cs = co2_mg_m3_cs * 44
		'h2o_g_m3_cs = h2o_g_m3_cs * .018

		'RM YOUNG 81000
		VoltDiff (wspeed,1,mV5000,1,True,0,0,0.01,0)'fourth parameter is the diff channel number
		VoltDiff (wdirection,1,mV5000,2,True,0,0,0.108,0)
		VoltDiff (welevation,1,mV5000,3,True,0,0,0.024,-60.0)
 VoltDiff (stempK,1,mV5000,4,True,0,0,0.02,220)
		stempC=stempK-273.15	'Converts sonic temp from Kelvin to Celsius
		'Call Output Tables


		'Get the CS7500 (LI-7500) data that is connected
		'with the RM YOUNG 81000
		'!!!!!!! THE SDM ADDRESS OF THE INSTRUMENT MUST BE CHANGED !!!!!!!!!!!!!
		CS7500 (licor_rm(1),1,7,5)
		'44 [g/mol] - molecular weight of carbon dioxide
		'0.018 [g/mmol] - molecular weight of water vapor
		co2_mg_m3_rm = co2_mg_m3_rm * 44
		h2o_g_m3_rm = h2o_g_m3_rm * .018


		RealTime(rtime())
		DSec=Second + uSecond/1000000
		rthetime=Timer(1,4,4)

		count = count + 1

				'CHECK VIA CSAT COMPARISON TEST WHICH WAY IS POSITIVE
		Ux_rm = wspeed * COS(welevation) * SIN(wdirection)
		Uy_rm = wspeed * COS(welevation) * COS(wdirection)
		Uz_rm = wspeed * SIN(welevation)

		'Calculate instantaneous flux
		wc_inst_rm = Uz_rm * co2_mg_m3_rm
		wc_inst_cs = Uz_cs * co2_mg_m3_cs
```

```
wr_inst_rm = Uz_rm * h2o_g_m3_rm
wr_inst_cs = Uz_cs * h2o_g_m3_cs

'Add to integrated w, c, r, and wc:
w_integ_rm = w_integ_rm + Uz_rm
w_integ_cs = w_integ_cs + Uz_cs
u_integ_rm = u_integ_rm + Ux_rm
u_integ_cs = u_integ_cs + Ux_cs
v_integ_rm = v_integ_rm + Uy_rm
v_integ_cs = v_integ_cs + Uy_cs

r_integ_rm = r_integ_rm + h2o_g_m3_rm
r_integ_cs = r_integ_cs + h2o_g_m3_cs
c_integ_rm = c_integ_rm + co2_mg_m3_rm
c_integ_cs = c_integ_cs + co2_mg_m3_cs
wc_integ_rm = wc_integ_rm + wc_inst_rm
wc_integ_cs = wc_integ_cs + wc_inst_cs
wr_integ_rm = wr_integ_rm + wr_inst_rm
wr_integ_cs = wr_integ_cs + wr_inst_cs

'CallTable inst_vars

'Average once time is 5 min (count = 1500):

' Determine the number of 200 ms cycles to average

ninteg = 10  '200ms -> 2sec

If count > ninteg-1 Then

  count = 0

        w_avg_rm = w_integ_rm / 10.0
        w_avg_cs = w_integ_cs / 10.0
        u_avg_rm = u_integ_rm / 10.0
        u_avg_cs = u_integ_cs / 10.0
        v_avg_rm = v_integ_rm / 10.0
        v_avg_cs = v_integ_cs / 10.0
        c_avg_rm = c_integ_rm / 10.0
        c_avg_cs = c_integ_cs / 10.0
        r_avg_rm = r_integ_rm / 10.0
        r_avg_cs = r_integ_cs / 10.0
        wc_avg_rm = wc_integ_rm / 10.0
        wc_avg_cs = wc_integ_cs / 10.0
        wr_avg_rm = wr_integ_rm / 10.0
        wr_avg_cs = wr_integ_cs / 10.0

        'Zero the integration variables
        w_integ_rm = 0.0
        w_integ_cs = 0.0
        u_integ_rm = 0.0
        u_integ_cs = 0.0
        v_integ_rm = 0.0
        v_integ_cs = 0.0
        c_integ_rm = 0.0
        c_integ_cs = 0.0
        r_integ_rm = 0.0
        r_integ_cs = 0.0
        wc_integ_rm = 0.0
        wc_integ_cs = 0.0
        wr_integ_rm = 0.0
```

```
                    wr_integ_cs = 0.0

                    CallTable avg_2s_cs
                    CallTable avg_2s_rm

                EndIf

                NextScan
SlowSequence

Scan(10,sec,3,0)
        Battery(Batt_Volt)

        'call data table
        CallTable(Metdata)
        NextScan


EndProg
```

High frequency (10Hz) program:

```
'CR5000 Series Datalogger
'program author: Percy Link

'Declare Public Variables

Public wind_cs(5)    'Ux,Uy,Uz,Tson,Diag
Public licor_cs(3)   'CO2,H2O,Press
Public wind_rm(5)    'Ux,Uy,Uz,Tson,Diag
Public licor_rm(3)   'CO2,H2O,Press

Public rthetime
Public rtime(9)
Public Batt_Volt
Public DSec


Public wc_inst_rm
Public wc_inst_cs
Public wr_inst_rm
Public wr_inst_cs


Public wc_integ_rm
Public wc_integ_cs
Public wr_integ_rm
Public wr_integ_cs
Public w_integ_rm
Public w_integ_cs
Public u_integ_rm
Public u_integ_cs
Public v_integ_rm
Public v_integ_cs
Public c_integ_rm
Public c_integ_cs
Public r_integ_rm
Public r_integ_cs
```

```
Public w_avg_rm
Public w_avg_cs
Public u_avg_rm
Public u_avg_cs
Public v_avg_rm
Public v_avg_cs
Public c_avg_rm
Public c_avg_cs
Public r_avg_rm
Public r_avg_cs
Public wr_avg_rm
Public wr_avg_cs
Public wc_avg_rm
Public wc_avg_cs

Public count

Public ninteg

'RM Young Temporary Variables
Public wspeed
Public wdirection
Public welevation
Public stempK
Public stempC

Public Ux_rm
Public Uy_rm
Public Uz_rm

Units wspeed = m/s
Units wdirection = deg
Units welevation = deg
Units stempK = K
Units stempC = C

'Define Aliases

Alias wind_cs(1) = Ux_cs
Alias wind_cs(2) = Uy_cs
Alias wind_cs(3) = Uz_cs
Alias wind_cs(4) = T_sonic_cs
Alias wind_cs(5) = diagnostic_cs

Alias licor_cs(1) = co2_mg_m3_cs
Alias licor_cs(2) = h2o_g_m3_cs
Alias licor_cs(3) = pressure_cs

Alias licor_rm(1) = co2_mg_m3_rm
Alias licor_rm(2) = h2o_g_m3_rm
Alias licor_rm(3) = pressure_rm

Alias rTime(1) = Year       'assign the alias Year to rTime(1)
Alias rTime(2) = Month      'assign the alias Month to rTime(2)
Alias rTime(3) = Day        'assign the alias Day to rTime(3)
Alias rTime(4) = Hour       'assign the alias Hour to rTime(4)
Alias rTime(5) = Minute     'assign the alias Minute to rTime(5)
Alias rTime(6) = Second     'assign the alias Second to rTime(6)
Alias rTime(7) = uSecond    'assign the alias uSecond to rTime(7)
Alias rTime(8) = WeekDay    'assign the alias WeekDay to rTime(8)
Alias rTime(9) = Day_of_Year        'assign the alias Day_of_Year to rTime(9)
```

```
DataTable(Metdata,TRUE,-1)

  Sample (1, Day_of_Year, IEEE4)
  Sample (1, Hour, IEEE4)
  Sample (1, Minute, IEEE4)
  Sample (1, DSec, IEEE4)
        Average(1,Batt_Volt,FP2,False)
EndTable


DataTable (ten_hz,TRUE,-1)
  Sample (1, Day_of_Year, IEEE4)
  Sample (1, Hour, IEEE4)
  Sample (1, Minute, IEEE4)
  Sample (1, DSec, IEEE4)
        Sample (1,Ux_rm,IEEE4)
        Sample (1,Uy_rm,IEEE4)
        Sample (1,Uz_rm,IEEE4)
        Sample (1,wspeed,IEEE4)
        Sample (1,wdirection,IEEE4)
        Sample (1,welevation,IEEE4)
        Sample (1,stempK,IEEE4)
        Sample (1,Ux_cs,IEEE4)
        Sample (1,Uy_cs,IEEE4)
        Sample (1,Uz_cs,IEEE4)
        Sample (1,T_sonic_cs,IEEE4)
        Sample (1,diagnostic_cs,IEEE4)
        Sample (1,co2_mg_m3_rm,IEEE4)
        Sample (1,h2o_g_m3_rm,IEEE4)
        Sample (1,pressure_rm,IEEE4)
        'CardOut( StopRing, Size )
EndTable


'Main Program


BeginProg
                'Start integrated flux, w, r, and c at zero
                wc_integ_rm = 0.0
                wc_integ_cs = 0.0
                w_integ_rm = 0.0
                w_integ_cs = 0.0
                u_integ_rm = 0.0
                u_integ_cs = 0.0
                v_integ_rm = 0.0
                v_integ_cs = 0.0
                c_integ_rm = 0.0
                c_integ_cs = 0.0
                wr_integ_rm = 0.0
                wr_integ_cs = 0.0
                r_integ_rm = 0.0
                r_integ_cs = 0.0

                count = 0     'counter for averaging period.

        SDMSpeed (30)
        'Measure a CSAT3 and LI-7500 at 20 Hz.
 'Timer(1,4,0)
```

```
Scan(100,msec,3,0)

        RealTime(rtime())

                'Get the CSAT3 data.
                CSAT3 (wind_cs(1),1,5,91,10)

                'Get the CS7500 (LI-7500) data that is connected
                'with the CSAT3
                'THE SDM ADDRESS OF THIS MUST BE CHANGED!!
                'CS7500 (licor_cs(1),1,7,5)
                '44 [g/mol] - molecular weight of carbon dioxide
                '0.018 [g/mmol] - molecular weight of water vapor
                'co2_mg_m3_cs = co2_mg_m3_cs * 44
                'h2o_g_m3_cs = h2o_g_m3_cs * .018

                'RM YOUNG 81000
                VoltDiff (wspeed,1,mV5000,1,True,0,0,0.01,0)'fourth parameter is the diff channel number
                VoltDiff (wdirection,1,mV5000,2,True,0,0,0.108,0)
                VoltDiff (welevation,1,mV5000,3,True,0,0,0.024,-60.0)
 VoltDiff (stempK,1,mV5000,4,True,0,0,0.02,220)
                stempC=stempK-273.15    'Converts sonic temp from Kelvin to Celsius
                'Call Output Tables


                'Get the CS7500 (LI-7500) data that is connected
                'with the RM YOUNG 81000
                '!!!!!!! THE SDM ADDRESS OF THE INSTRUMENT MUST BE CHANGED !!!!!!!!!!!!
                CS7500 (licor_rm(1),1,7,5)
                '44 [g/mol] - molecular weight of carbon dioxide
                '0.018 [g/mmol] - molecular weight of water vapor
                co2_mg_m3_rm = co2_mg_m3_rm * 44
                h2o_g_m3_rm = h2o_g_m3_rm * .018


                RealTime(rtime())
                DSec=Second + uSecond/1000000
                rthetime=Timer(1,4,4)


                CallTable ten_hz

        NextScan
 SlowSequence

 Scan(10,sec,3,0)
        Battery(Batt_Volt)

        'call data table
        CallTable(Metdata)
        NextScan


EndProg
```

Appendix C:
MATLAB Scripts for Modeling Tests

General Organization of Files:

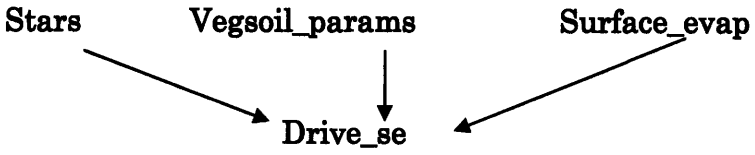

Stars.m (same for all tests):

```
%%%%%%%%%%%%%%%%%%%%%%%%%%%%%%%%%%%%%%%%%%%%%%%%%%%%%%%%%%%%%%%%%%%%%%%%%%%%%%%
%
%  Formulation of friction velocities of momentum, vapor and heat.
%  Also known as ustar, rstar and tstar respectively.
%
%  These lines of code were taken from subroutine stars() in
%  leaf3.f90 from the LEAF3 LSM packaged in the BRAMS4.0 modelling
%  package.
%
%  Again, Brutsaert and Garratt are fine references. Stull may also
%  be a good reference for this as well.
%
%  The leaf3 code cites Louis (1981).
%
%  Note that all values are scalar.
%
%  Output variables
%
%   ustar     - friction velocity
%   tstar     - friction velocity of heat transfer
%   rstar     - friction velocity of vapor transfer
%   vels_pat  - wind speed that ensures minimum condition
%
%  Input variables
%
%   ths       - potential temperature of the ambient atmosphere at
%               reference height zts ("s" is for surface layer,
%               between 30 - 100m) [deg K]
%   rvs       - water vapor mixing ratio of the ambient atmosphere in the
%               surface layer at reference height zts [kg/kg]
%   thetacan  - potential temperature of the canopy air space [K]
%   can_rvap  - water vapor mixing ratio of the canopy air space
%               [kg/kg]
%   zts       - The refernce height, or height of observations.
%               Should be in the surface layer, see Stull
%   patch_rough - The aggregate roughness length of the surface
%               element below the turbulent boundary layer of interest
%   vels      - The wind speed magnitude, ie the wind speed along its
%               vector of motion
%%%%%%%%%%%%%%%%%%%%%%%%%%%%%%%%%%%%%%%%%%%%%%%%%%%%%%%%%%%%%%%%%%%%%%%%%%%%%%%

function [ustar,tstar,rstar,vels_pat] = stars(ths,rvs,thetacan, ...
    can_rvap,zts,patch_rough,vels)


% parameters
```

```
g     = 9.81;          % Gravity [m/s2]
ubmin = 0.25;          % Minimum wind velocity
ustmin= 0.10;          % Minumum ustar
vonk  = 0.40;

vels_pat = max(vels,ubmin);

b = 5.0;

csm = 7.5;

csh = 5.0;

d = 5.0;

% a2 is the drag coefficient in neutral conditions, here same for h/m
% ri is the bulk richardson numer, eq. 3.45 in Garratt

a2 = (vonk / log(zts./patch_rough)).^2;
c1 = a2*vels_pat;
ri = g * zts * (ths - thetacan) ./ (.5 * (ths + thetacan) * vels_pat ...
                    * vels_pat);

if (ths - thetacan > 0.0 )   % STABLE CASE

   fm = 1. / (1. + (2 * b * ri / sqrt(1 + d * ri)));
   fh = 1. / (1. + (3 * b * ri * sqrt(1 + d * ri)));

else                         % UNSTABLE CASE

   c2 = b * a2 * sqrt(zts / patch_rough * (abs(ri)));
   cm = csm * c2;
   ch = csh * c2;
   fm = (1. - 2 * b * ri / (1. + 2 * cm));
   fh = (1. - 3 * b * ri / (1. + 3 * ch));

end

ustar = max(ustmin,sqrt(c1 * vels_pat * fm));
c3 = c1 * fh / ustar;
rstar = c3 * (rvs - can_rvap);
tstar = c3 * (ths - thetacan);
```

Vegsoil_params.m (same for all tests):

```
%%%%%%%%%%%%%%%%%%%%%%%%%%%%%%%%%%%%%%%%%%%%%%%%%%%%%%%%%%%%%%%%%%%%%%%%%%%%%%%%
%
%  Data tables for vegetation and soil classifications
%
%
%%%%%%%%%%%%%%%%%%%%%%%%%%%%%%%%%%%%%%%%%%%%%%%%%%%%%%%%%%%%%%%%%%%%%%%%%%%%%%%%



%-----------------------------------------------------------------------------
% slpots        slbs          slcons0         slden       USDA SOIL CLASS
%       slmsts         slcons          slcpd         fc     # AND NAME
%-----------------------------------------------------------------------------

soilparms = ...
[-.121, .395,  4.05, .18e-3, .50e-3, 1465.e3, 1600.,.135   %  1 sand
,-.090, .410,  4.38, .16e-3, .60e-3, 1407.e3, 1600.,.150   %  2 loamy sand
,-.218, .435,  4.9 , .34e-4, .77e-3, 1344.e3, 1600.,.195   %  3 sandy loam
,-.786, .485,  5.3 , .72e-5, .11e-4, 1273.e3, 1600.,.255   %  4 silt loam
,-.478, .451,  5.39, .69e-5, .22e-2, 1214.e3, 1600.,.240   %  5 loam
,-.299, .420,  7.12, .63e-5, .15e-2, 1177.e3, 1600.,.255   %  6 sandy clay loam
,-.356, .477,  7.75, .17e-5, .11e-3, 1319.e3, 1600.,.322   %  7 silty clay loam
```

```
,-.630, .476,  8.52, .24e-5, .22e-2, 1227.e3, 1600.,.325   %  8 clay loam
,-.153, .426, 10.4 , .22e-5, .22e-5, 1177.e3, 1600.,.310   %  9 sandy clay
,-.490,..492, 10.4 , .10e-5, .10e-5, 1151.e3, 1600.,.370   % 10 silty clay
,-.405, .482, 11.4 , .13e-5, .13e-5, 1088.e3, 1600.,.367   % 11 clay
,-.356, .863,  7.75, .80e-5, .80e-5,  874.e3,  300.,.535]; % 12 peat

%  Flip the matrix to array form
soilparms = soilparms';

 sz = size(soilparms);
 nstyp = sz(2);


 xsand  = [.97,.92,.80,.57,.60,.65,.35,.48,.50,.30,.25,.20];
 xclay  = [.03,.07,.18,.40,.35,.31,.59,.45,.42,.61,.65,.20];
 xorgan = [.00,.01,.02,.03,.05,.04,.06,.07,.08,.09,.10,.60];

 xrobulk= [1200.,1250.,1300.,1400.,1350., ...
       1350.,1500.,1450.,  1450.,1650.,1700., 500.];

%         LEAF-3 BIOPHYSICAL PARAMETERS BY LANDUSE CLASS NUMBER


%-------------------------------------------------------------------------
%albv_green     sr_max         veg_clump       rootdep            LEAF-3 CLASS #
%     albv_brown     tai_max         veg_frac        dead_frac      AND DESCRIPTION
%          emisv          sai            veg_ht          rcmin
%-------------------------------------------------------------------------
bioparms = ...
[ .00, .00, .00,  .0, 0.0,  .0,  .0, .00,   .0,  .0, .0,   0., %  1  Ocean
  .00, .00, .00,  .0, 0.0,  .0,  .0, .00,   .0,  .0, .0,   0., %  2  Lakes, rivers,
streams
  .00, .00, .00,  .0, 0.0,  .0,  .0, .00,   .0,  .0, .0,   0., %  3  Ice cap/glacier
  .00, .00, .00,  .0, 0.0,  .0,  .0, .00,   .0,  .0, .0,   0., %  4  Desert, bare soil
  .14, .24, .97, 5.4, 8.0, 1.0, 1.0, .80, 20.0, 1.5, .0, 500., %  5  Evergreen
needleleaf tree
  .14, .24, .95, 5.4, 8.0, 1.0, 1.0, .80, 22.0, 1.5, .0, 500., %  6  Deciduous
needleleaf tree
  .20, .24, .95, 6.2, 7.0, 1.0,  .0, .80, 22.0, 1.5, .0, 500., %  7  Deciduous
broadleaf tree
  .12, .18, .95, 4.1, 6.5, 1.0,  .0, .90, 32.0, 2.5, .0, 285., %  8  Evergreen
broadleaf tree
  .13, .30, .96, 5.1, 4.0, 1.0,  .0, .75,   .3,  .7, .7, 100., %  9  Short grass
  .24, .43, .96, 5.1, 5.0, 1.0,  .0, .80,  1.2, 1.0, .7, 100., % 10  Tall grass
  .24, .24, .96, 5.1, 1.0,  .2, 1.0, .20,   .7, 1.0, .0, 500., % 11  Semi-desert
  .20, .24, .95, 5.1, 4.5,  .5, 1.0, .60,   .2, 1.0, .0,  50., % 12  Tundra
  .14, .24, .97, 5.1, 5.5, 1.0, 1.0, .70,  1.0, 1.0, .0, 500., % 13  Evergreen shrub
  .20, .28, .97, 5.1, 5.5, 1.0, 1.0, .70,  1.0, 1.0, .0, 500., % 14  Deciduous shrub
  .16, .24, .96, 6.2, 7.0, 1.0,  .5, .80, 22.0, 1.5, .0, 500., % 15  Mixed woodland
  .22, .40, .95, 5.1, 5.0,  .5,  .0, .85,  1.0, 1.0, .0, 100., % 16  Crop/mixed
farming, C3 grassland
  .18, .40, .95, 5.1, 5.0,  .5,  .0, .80,  1.1, 1.0, .0, 500., % 17  Irrigated crop
  .12, .43, .98, 5.1, 7.0, 1.0,  .0, .80,  1.6, 1.0, .0, 500., % 18  Bog or marsh
  .13, .30, .96, 5.1, 6.0, 1.0,  .0, .80,  7.0, 1.5, .0, 100., % 19  Wooded grassland
  .20, .36, .90, 5.1, 3.6, 1.0,  .0, .74,  6.0,  .8, .0, 500., % 20  Urban and built
up
  .17, .24, .95, 4.1, 7.0, 1.0,  .0, .90, 32.0, 1.5, .0, 500., % 21  Wetland evergreen
broadleaf tree
  .16, .24, .96, 5.1, 2.0, 1.5, 1.0, .10, 20.0, 1.5, .0, 500.]; % 22  Very urban

 bioparms = bioparms';

 sz = size(bioparms);
 nvtyp = sz(2);

% Soil constants

% Thermal conductivity in J/msK
cka = 0.418684 * 0.0615;
ckw = 0.418684 * 1.45;
romin = 2655.0;
roorg = 1300.0;
```

```
slfcap = -10. / 3.;
refdepth = -2.0;

for nnn = 1:nstyp
   slcons0(nnn) = soilparms(5,nnn);
   fhydraul(nnn) = log (soilparms(4,nnn) / soilparms(5,nnn)) / refdepth;

   slpots(nnn) = soilparms(1,nnn);
   slmsts(nnn) = soilparms(2,nnn);
   slbs(nnn)   = soilparms(3,nnn);
   slcons(nnn) = soilparms(4,nnn);
   slcons00(nnn) = soilparms(5,nnn);
   slcpd(nnn)  = soilparms(6,nnn);
   slden(nnn)  = soilparms(7,nnn);
   sfldcap(nnn)  = soilparms(8,nnn);

   emisg(nnn) = .98;
   slfc(nnn) = slmsts(nnn) * (slfcap / slpots(nnn)) .^ (-1. / slbs(nnn));
   soilcp(nnn) = 0.1 - 0.07 * xsand(nnn);

end

for nnn = 1:nvtyp
   albv_green(nnn) = bioparms(1,nnn);
   albv_brown(nnn) = bioparms(2,nnn);
   emisv(nnn)      = bioparms(3,nnn);
   sr_max(nnn)     = bioparms(4,nnn);
   tai_max(nnn)    = bioparms(5,nnn);
   sai(nnn)        = bioparms(6,nnn);
   veg_clump(nnn)  = bioparms(7,nnn);
   veg_frac(nnn)   = bioparms(8,nnn);
   veg_ht(nnn)     = bioparms(9,nnn);
   dead_frac(nnn)  = bioparms(11,nnn);
   rcmin(nnn)      = bioparms(12,nnn);
   glai_max(nnn)   = tai_max(nnn) - sai(nnn);

end
```

Test 1: Current Model Formulation

Surface_evap.m

```
%%%%%%%%%%%%%%%%%%%%%%%%%%%%%%%%%%%%%%%%%%%%%%%%%%%%%%%%%%%%%%%%%%%%%%%%%%%%%%%%
%
%  Formulation of vapor flux resistance from soil to the canopy sublayer
%
%  For a streamlined description, which is consistent with the
%    formulation in the CLM model, see Gordan Bonan's Technical
%    Manual (NCAR/TN-417+STR)
%
%  These lines of code were taken from leaf3.f90 as presented in
%  the BRAMS4.0 coupled model package.  Updates may have occured
%  since then.
%
%  For a more illustrious treatment of subcanopy resistance
%  functions, recommended reading is Brutsaert, Wilfred (1984),
%  Evaporation into the Atmosphere and also Garratt,JR (1992), The
%  Atmospheric Boundary Layer.  The prior has a slightly more
%  focused treatment on sub-canopy layer turbulence and diffusivities.
%
%%%%%%%%%%%%%%%%%%%%%%%%%%%%%%%%%%%%%%%%%%%%%%%%%%%%%%%%%%%%%%%%%%%%%%%%%%%%%%%%

function [rasgnd,rasveg,rd] = surface_evap(soil_rough,veg_rough, ...
    snowfac,veg_height,ustar,zts,vels,veg_tai  )


  %   Parameters
```

```
  exar = 2.5;     %  This is the canopy diffusivity extinction coef.
  vonk = 0.4;     %  VonKarman's constant, shown in literature
                  %  anywhere from 0.38 to 0.41
  covr = 2.16;    %  Resistance partitioning coefficient
  c1=116.6;       %  Maybe not necessary

  zognd = soil_rough;       %  The surface roughness length
  zoveg = veg_rough * (1.-snowfac) + zognd * snowfac;      %  The vegetation roughness
length
  % zdisp = veg_height * (1.-snowfac);                      %  The zero-plane
displacement height
  zveg = veg_height;
  % zveg = zdisp / 0.63;      % The effective height of the vegetation
                            % This is really the root of the problem
                            % in my opinion
  zdisp = 0.63 * zveg;

  %   The old formulation commented out in the LEAF3 code
  %bob      rasgnd = log(zts / zognd) * log((zdisp + zoveg) / zognd)
  %bob     +       / (vonk * vonk * vels)


   rasgnd = 5.0 / ustar;    % The flux resistance of bare soil

   % factv = log(zts / zoveg) / (vonk * vonk * vels);
   aux = exp(exar * (1. - (zdisp + zoveg) / zveg));
   % rasveg = factv * zveg / (exar * (zveg - zdisp)) * (exp(exar) - aux);
   rasveg = zveg * (exp(exar * (1 - zoveg/zveg)) - aux) / (exar * vonk * ustar * (zveg
- zdisp));
   c2 = max(0.,min(1., 1.1 * veg_tai / covr));
   rd = rasgnd * (1. - c2) + rasveg * c2;
```

Drive_se.m:

```
%%%%%%%%%%%%%%%%%%%%%%%%%%%%%%%%%%%%%%%%%%%%%%%%%%%%%%%%%%%%%%%%%%%%%%%%
%
% Driver for soil eveporation calculator
%
%%%%%%%%%%%%%%%%%%%%%%%%%%%%%%%%%%%%%%%%%%%%%%%%%%%%%%%%%%%%%%%%%%%%%%%%

clear all;

% Set up the vegetation and soil parameters

vegsoil_params;

% Parameters

zrough = 0.05;


% Choose a vegetation type and soil type

veg_type  = 8;    % Evergreen Broadleaf Tree
soil_type = 8;    % Clay Loam

zts     = 90;
vels    = 4.0;
vonk    = 0.41;

ths     = 295;
thetacan = 295;
snowfac  = 0.0;

rvs     = 25 * 0.001;
can_rvap = 30 * 0.001;

% veg_height  = veg_ht(veg_type);
```

```
soil_rough  = 0.05;

veg_height_vec = linspace(1,41,20);

wind = [0.5,1.0,2.0,4.0,8.0];

wind_legend = {'0.5 m/s','1.0 m/s','2.0 m/s','4.0 m/s','8.0 m/s'};

for i=1:20

    veg_height = veg_height_vec(i);

    %vels = wind(j);

    % Calculate the LAI of the vegetation
    veg_tai = 4.0;

    % veg_rough   = veg_height * (1. - bz * exp(-hz * veg_tai))
    veg_rough   = .13 * veg_height;

    % topzo       = ;
    % patch_rough = max(topzo,soil_rough,veg_rough);
    % get some average values of topzo from BRAMS
    patch_rough = max(soil_rough,veg_rough);

    [ustar,tstar,rstar,vels_pat] = stars(ths,rvs,thetacan, ...
        can_rvap,zts,patch_rough,vels);

    Ktop = vonk*(veg_height-veg_height*0.63)*ustar;

    [rasgnd,rasveg,rd] = surface_evap(soil_rough,veg_rough, ...
        snowfac,veg_height,ustar,zts,vels,veg_tai  );

    res(i) = rd;

end
```

Test 2: Varying Eddy Diffusivity Extinction Coefficient

Drive_se_exar_LE.m

```
clear all;


% Set up the vegetation and soil parameters

vegsoil_params;

% Parameters

zrough = 0.05;


% Choose a vegetation type and soil type

veg_type  = 8;   % Evergreen Broadleaf Tree
soil_type = 8;   % Clay Loam

zts      = 90;
vels     = 4.0;
vonk     = 0.4;

ths      = 295;
thetacan = 295;
snowfac  = 0.0;

rvs      = 25 * 0.001;
can_rvap = 30 * 0.001;
```

```
% veg_height = veg_ht(veg_type);
veg_tai = tai_max(veg_type);
veg_height_vec = linspace(1,41,20);

soil_rough  = 0.05;
beta_c = 0.6;           % soil moisture: ratio of actual to saturation water content

lambda = 2.25e6;        % latent heat of vaporization, in J/kg
rho_atm = 1;            % density of atmosphere in kg/m3
q_can = 0.016/1.2;      % canopy specific humidity, kg water/kg air; typical value
from Puerto Rico subcan data
q_sat_g = 0.0173/1.2;   % saturated specific humidity at ground temp (T=20 oC, taken
from typical
                            % PR data for subcanopy temp)

LE = zeros(6,20);
exar_vec = [.5,1.5,2.5,3.5,4.5,5.5];

for k=1:6

    exar = exar_vec(k);

    for i=1:20

        veg_height  = veg_height_vec(i);

        veg_rough   = .13 * veg_height;

        patch_rough = max(soil_rough,veg_rough);

        [ustar,tstar,rstar,vels_pat] = stars(ths,rvs,thetacan, ...
            can_rvap,zts,patch_rough,vels);

        [rasgnd,rasveg,rd] = surface_evap_exar(soil_rough,veg_rough, ...
            snowfac,veg_height,ustar,exar,veg_tai);

        r_srf = 150 * snowfac + (1 - snowfac)*rd*(1 - beta_c) / beta_c;    %
resistance to vapor flux from soil

        LE(k,i) = -rho_atm * lambda * (q_can - q_sat_g) / (rd + r_srf);
        res(k,i) = rd;
    end
end
```

Surface_evap_exar.m

```
function [rasgnd,rasveg,rd] = surface_evap_exar(soil_rough,veg_rough, ...
    snowfac,veg_height,ustar,exar,veg_tai)


  %   Parameters
  %exar = 2.5;     %  This is the canopy diffusivity extinction coef.
  vonk = 0.4;     %  VonKarman's constant, shown in literature
                  %  anywhere from 0.38 to 0.41
  covr = 2.16;    %  Resistance partitioning coefficient
  c1=116.6;       %  Maybe not necessary

  zognd = soil_rough;       %  The surface roughness length
  zoveg = veg_rough * (1.-snowfac) + zognd * snowfac;      %  The vegetation roughness
length
  % zdisp = veg_height * (1.-snowfac);                      %  The zero-plane
displacement height
  zveg = veg_height;
  % zveg = zdisp / 0.63;      % The effective height of the vegetation
                            % This is really the root of the problem
                            % in my opinion
  zdisp = 0.63 * zveg;
```

```
  %   The old formulation commented out in the LEAF3 code
  %bob      rasgnd = log(zts / zognd) * log((zdisp + zoveg) / zognd)
  %bob     +      / (vonk * vonk * vels)


   rasgnd = 5.0 / ustar;   % The flux resistance of bare soil

   % factv = log(zts / zoveg) / (vonk * vonk * vels);
   aux = exp(exar * (1. - (zdisp + zoveg) / zveg));
   % rasveg = factv * zveg / (exar * (zveg - zdisp)) * (exp(exar) - aux);
   rasveg = zveg * (exp(exar * (1 - zoveg/zveg)) - aux) / (exar * vonk * ustar * (zveg
- zdisp));
   c2 = max(0.,min(1., 1.1 * veg_tai / covr));
   rd = rasgnd * (1. - c2) + rasveg * c2;
```

Test 3: Harman & Finnigan (2007) Model

Drive_se_HF_LE.m

```
%%%%%%%%%%%%%%%%%%%%%%%%%%%%%%%%%%%%%%%%%%%%%%%%%%%%%%%%%%%%%%%%%%%%%%%%%%%%%%%%
%
% Driver for soil evaporation calculator:
%   Harman & Finnigan (2007) formulation for eddy diffusivity
%
%%%%%%%%%%%%%%%%%%%%%%%%%%%%%%%%%%%%%%%%%%%%%%%%%%%%%%%%%%%%%%%%%%%%%%%%%%%%%%%%

clear all;


% Set up the vegetation and soil parameters

vegsoil_params;

% Parameters

zrough = 0.05;


% Choose a vegetation type and soil type

veg_type  = 8;    % Evergreen Broadleaf Tree
soil_type = 8;    % Clay Loam

zts       = 90;
vels      = 4.0;
vonk      = 0.4;

ths       = 295;
thetacan  = 295;
snowfac   = 0.0;

rvs       = 25 * 0.001;
can_rvap  = 30 * 0.001;

% veg_height = veg_ht(veg_type);
% veg_tai = tai_max(veg_type);
lai_vec = [2,3,4,5,6];
veg_height_vec = linspace(1,41,20);

soil_rough  = 0.05;
beta_c = 0.6;             % soil moisture: ratio of actual to saturation water content

lambda = 2.25e6;          % latent heat of vaporization, in J/kg
rho_atm = 1;              % density of atmosphere in kg/m3
q_can = 0.016/1.2;        % canopy specific humidity, kg water/kg air; typical value
from Puerto Rico subcan data
q_sat_g = 0.0173/1.2;     % saturated specific humidity at ground temp (T=20 oC, taken
from typical
```

```
                                % PR data for subcanopy temp)

% Harman & Finnigan beta in neutral conditions (p.348):
beta_n = 0.3;


LE = zeros(2,20);

for k=1:5

    veg_tai = lai_vec(k);

    for i=1:20

        veg_height = veg_height_vec(i);

        veg_rough   = .13 * veg_height;

        patch_rough = max(soil_rough,veg_rough);

        [ustar,tstar,rstar,vels_pat] = stars(ths,rvs,thetacan, ...
            can_rvap,zts,patch_rough,vels);

        % Harman & Finnigan (2007) penetration depth:
        Lc = 4 * veg_height / veg_tai;

        % H&F mixing length:
        lm = 2 * (beta_n)^3 * Lc;

        % H&F displacement depth:
        dt = (beta_n)^2 * Lc;

        % H&F similarity function at canopy top:
        phi_top = vonk / (2 * beta_n);

        % H&F wind gradient at canopy top:
        dudz_top = (ustar * phi_top) / (vonk * dt);

        [rasgnd,rasveg,rd,term1,term2,term3] =
surface_evap_test2(soil_rough,veg_rough, ...
            snowfac,veg_height,ustar,veg_tai,beta_n,lm,vels,zts,Lc);

        r_srf = 150 * snowfac + (1 - snowfac)*rd*(1 - beta_c) / beta_c;     %
resistance to vapor flux from soil

        LE(k,i) = -rho_atm * lambda * (q_can - q_sat_g) / (rd + r_srf);
%         if veg_tai > 2
%             LE(k,i) = 0;
%         end
        res(k,i) = rd;
        rveg(k,i) = rasveg;
        term1_vec(k,i) = term1;
        term2_vec(k,i) = term2;
        term3_vec(k,i) = term3;
        Lc_vec(k,i) = Lc;

    end
end
```

Surface_evap_test2.m

```
function [rasgnd,rasveg,rd,term1,term2,term3] =
surface_evap_test2(soil_rough,veg_rough, ...
    snowfac,veg_height,ustar,veg_tai,beta_n,lm,vels,zts,Lc)


  %   Parameters
  covr = 2.16;   %  Resistance partitioning coefficient
```

```
  zognd = soil_rough;        % The surface roughness length
  zoveg = veg_rough * (1.-snowfac) + zognd * snowfac;      %  The vegetation roughness
length
  zveg = veg_height;         % canopy height
  zdisp = zveg - (beta_n)^2 * Lc;  % displacement height calculated from H&F disp.
depth


   rasgnd = 5.0 / ustar;   % The flux resistance of bare soil

   term1 = exp(beta_n/lm*(zveg - zoveg - zdisp));
   term2 = exp(beta_n/lm*(zveg - zoveg));
   term3 = lm^2 * (vels - ustar/(2*beta_n) * log((zts-zdisp)/(zveg-zdisp)));
   rasveg = -term3^(-1)*(term1 - term2);
   c2 = max(0.,min(1., 1.1 * veg_tai / covr));
   rd = rasgnd * (1. - c2) + rasveg * c2;
```

Test 4: Nepf et al. (2007) Vortex Penetration Cutoff

Drive_se_Nepf_LE.m

```
%%%%%%%%%%%%%%%%%%%%%%%%%%%%%%%%%%%%%%%%%%%%%%%%%%%%%%%%%%%%%%%%%%%%%%%%
%
% Driver for soil evaporation calculator:
%   rough wall boundary formulation for eddy diffusivity, Nepf
%   penetration cutoff
%
%%%%%%%%%%%%%%%%%%%%%%%%%%%%%%%%%%%%%%%%%%%%%%%%%%%%%%%%%%%%%%%%%%%%%%%%

clear all;


% Set up the vegetation and soil parameters

vegsoil_params;

% Parameters

zrough = 0.05;


% Choose a vegetation type and soil type

veg_type  = 8;    % Evergreen Broadleaf Tree
soil_type = 8;    % Clay Loam

zts       = 90;
vels      = 4.0;
vonk      = 0.4;

ths       = 295;
thetacan  = 295;
snowfac   = 0.0;

rvs       = 25 * 0.001;
can_rvap  = 30 * 0.001;

% veg_height = veg_ht(veg_type);
% veg_tai = tai_max(veg_type);
lai_vec = [0.9];
veg_height_vec = linspace(1,41,20);

soil_rough  = 0.05;
beta_c = 0.6;            % soil moisture: ratio of actual to saturation water content

lambda = 2.25e6;         % latent heat of vaporization, in J/kg
rho_atm = 1;             % density of atmosphere in kg/m3
```

```
q_can = 0.016/1.2;      % canopy specific humidity, kg water/kg air; typical value
from Puerto Rico subcan data
q_sat_g = 0.0173/1.2;   % saturated specific humidity at ground temp (T=20 oC, taken
from typical
                            % PR data for subcanopy temp)

% Harman & Finnigan beta in neutral conditions (p.348):
beta_n = 0.3;


LE = zeros(1,20);

for k=1:1

    veg_tai = lai_vec(k);

    for i=1:20

        veg_height = veg_height_vec(i);

        veg_rough   = .13 * veg_height;

        patch_rough = max(soil_rough,veg_rough);

        [ustar,tstar,rstar,vels_pat] = stars(ths,rvs,thetacan, ...
            can_rvap,zts,patch_rough,vels);

        % Harman & Finnigan (2007) penetration depth:
        Lc = 4 * veg_height / veg_tai;

        % H&F mixing length:
        lm = 2 * (beta_n)^3 * Lc;

        % H&F displacement depth:
        dt = (beta_n)^2 * Lc;

        % H&F similarity function at canopy top:
        phi_top = vonk / (2 * beta_n);

        % H&F wind gradient at canopy top:
        dudz_top = (ustar * phi_top) / (vonk * dt);

        [rasgnd,rasveg,rd] = surface_evap(soil_rough,veg_rough, ...
            snowfac,veg_height,ustar,zts,vels,veg_tai  );

        r_srf = 150 * snowfac + (1 - snowfac)*rd*(1 - beta_c) / beta_c;    %
resistance to vapor flux from soil

        LE(k,i) = -rho_atm * lambda * (q_can - q_sat_g) / (rd + r_srf);
%         if veg_tai > 2
%             LE(k,i) = 0;
%         end
        res(k,i) = rd;
        rveg(k,i) = rasveg;
%         term1_vec(k,i) = term1;
%         term2_vec(k,i) = term2;
%         term3_vec(k,i) = term3;
%         Lc_vec(k,i) = Lc;

    end
end
```

Appendix D:

MATLAB Scripts for Field Data Analysis

March 17, 2008 data: twosecavgbottom77.m

```
% Program to load 2 second averaged data from day 77 with Licor at bottom.

clear all
close all

% load CSAT/Licor data

load csat_lic_2s_77.csv

% load RM Young data

load rm_2s_77.csv

% label CSAT/Licor columns

record_cs = csat_lic_2s_77(:,1);                % record number
day_cs = csat_lic_2s_77(:,2);                   % day
hour_cs = csat_lic_2s_77(:,3);                  % hour
minute_cs = csat_lic_2s_77(:,4);                % minute
DSec_cs = csat_lic_2s_77(:,5);                  % second with decimal
u_avg_cs = csat_lic_2s_77(:,6);                 % x-velocity 2 sec avg
v_avg_cs = csat_lic_2s_77(:,7);                 % y-velocity 2 sec avg
w_avg_cs = csat_lic_2s_77(:,8);                 % z-velocity 2 sec avg
c_avg_cs = csat_lic_2s_77(:,9);                 % CO2 conc 2 sec avg
r_avg_cs = csat_lic_2s_77(:,10);                % H2O conc 2 sec avg
wc_avg_cs = csat_lic_2s_77(:,11);               % vertical CO2 flux 2 sec avg
wr_avg_cs = csat_lic_2s_77(:,12);               % vertical H2O flux 2 sec avg

dn = datenum(2008,1,day_cs,hour_cs,minute_cs,DSec_cs);


% label RM Young columns

record_rm = rm_2s_77(:,1);                      % record number
day_rm = rm_2s_77(:,2);                         % day
hour_rm = rm_2s_77(:,3);                        % hour
minute_rm = rm_2s_77(:,4);                      % minute
DSec_rm = rm_2s_77(:,5);                        % second with decimal
u_avg_rm = rm_2s_77(:,6);                       % x-velocity 2 sec avg
v_avg_rm = rm_2s_77(:,7);                       % y-velocity 2 sec avg
w_avg_rm = rm_2s_77(:,8);                       % z-velocity 2 sec avg


% Convert units for CO2 from mg/m3 to g/m3

c_avg_cs = c_avg_cs ./ 1000;
wc_avg_cs = wc_avg_cs ./ 1000;


% calculate w_bar times c_bar for CSAT/Licor

w_r_avg_cs = w_avg_cs .* r_avg_cs;              % avg vertical velocity times avg H2O
conc
w_c_avg_cs = w_avg_cs .* c_avg_cs;              % avg vertical velocity times avg CO2
conc

% calculate covariances (wc_bar minus w_bar*c_bar)

wc_prime_cs = wc_avg_cs - w_c_avg_cs;           % covariance of vertical velocity and
CO2
wr_prime_cs = wr_avg_cs - w_r_avg_cs;           % covariance of vertical velocity and
```

```
H2O

% convert g/m2s to W/m2

wr_prime_cs_W = wr_prime_cs .* 2.25e3;      % times lambda, divided by 1000g/kg
```

March 18, 2008 data: twosecavgbottom78.m

```
% Program to load 2 second averaged data from day 78 with Licor at bottom.

clear all
close all

% load CSAT/Licor data

load csat_lic_2s_78.csv

% load RM Young data

load rm_2s_78.csv

% label CSAT/Licor columns

record_cs = csat_lic_2s_78(:,1);                    % record number
day_cs = csat_lic_2s_78(:,2);                       % day
hour_cs = csat_lic_2s_78(:,3);                      % hour
minute_cs = csat_lic_2s_78(:,4);                    % minute
DSec_cs = csat_lic_2s_78(:,5);                      % second with decimal
u_avg_cs = csat_lic_2s_78(:,6);                     % x-velocity 2 sec avg
v_avg_cs = csat_lic_2s_78(:,7);                     % y-velocity 2 sec avg
w_avg_cs = csat_lic_2s_78(:,8);                     % z-velocity 2 sec avg
c_avg_cs = csat_lic_2s_78(:,9);                     % CO2 conc 2 sec avg
r_avg_cs = csat_lic_2s_78(:,10);                    % H2O conc 2 sec avg
wc_avg_cs = csat_lic_2s_78(:,11);                   % vertical CO2 flux 2 sec avg
wr_avg_cs = csat_lic_2s_78(:,12);                   % vertical H2O flux 2 sec avg

dn = datenum(2008,1,day_cs,hour_cs,minute_cs,DSec_cs);


% label RM Young columns

record_rm = rm_2s_78(:,1);                          % record number
day_rm = rm_2s_78(:,2);                             % day
hour_rm = rm_2s_78(:,3);                            % hour
minute_rm = rm_2s_78(:,4);                          % minute
DSec_rm = rm_2s_78(:,5);                            % second with decimal
u_avg_rm = rm_2s_78(:,6);                           % x-velocity 2 sec avg
v_avg_rm = rm_2s_78(:,7);                           % y-velocity 2 sec avg
w_avg_rm = rm_2s_78(:,8);                           % z-velocity 2 sec avg

% Convert units for CO2 from mg/m3 to g/m3

c_avg_cs = c_avg_cs ./ 1000;
wc_avg_cs = wc_avg_cs ./ 1000;


% calculate w_bar times c_bar for CSAT/Licor

w_r_avg_cs = w_avg_cs .* r_avg_cs;              % avg vertical velocity times avg H2O
conc
w_c_avg_cs = w_avg_cs .* c_avg_cs;              % avg vertical velocity times avg CO2
conc

% calculate covariances (wc_bar minus w_bar*c_bar)

wc_prime_cs = wc_avg_cs - w_c_avg_cs;           % covariance of vertical velocity and
CO2
wr_prime_cs = wr_avg_cs - w_r_avg_cs;           % covariance of vertical velocity and
H2O
```

March 19, 2008 data: twosecavgtop79.m

```
% Program to load 2 second averaged data from day 79 with Licor at top

clear all
close all

% load CSAT/Licor data

load csat_only_2s_79.csv

% load RM Young data

load rm_lic_2s_79.csv

% label RM/Licor columns

record_rm = rm_lic_2s_79(:,1);                  % record number
day_rm = rm_lic_2s_79(:,2);                     % day
hour_rm = rm_lic_2s_79(:,3);                    % hour
minute_rm = rm_lic_2s_79(:,4);                  % minute
DSec_rm = rm_lic_2s_79(:,5);                    % second with decimal
u_avg_rm = rm_lic_2s_79(:,6);                   % x-velocity 2 sec avg
v_avg_rm = rm_lic_2s_79(:,7);                   % y-velocity 2 sec avg
w_avg_rm = rm_lic_2s_79(:,8);                   % z-velocity 2 sec avg
c_avg_rm = rm_lic_2s_79(:,9);                   % CO2 conc 2 sec avg
r_avg_rm = rm_lic_2s_79(:,10);                  % H2O conc 2 sec avg
wc_avg_rm = rm_lic_2s_79(:,11);                 % vertical CO2 flux 2 sec avg
wr_avg_rm = rm_lic_2s_79(:,12);                 % vertical H2O flux 2 sec avg

% Convert units for CO2 from mg/m3 to g/m3

c_avg_rm = c_avg_rm ./ 1000;
wc_avg_rm = wc_avg_rm ./ 1000;


% label CSAT columns

record_cs = csat_only_2s_79(:,1);                       % record number
day_cs = csat_only_2s_79(:,2);                          % day
hour_cs = csat_only_2s_79(:,3);                         % hour
minute_cs = csat_only_2s_79(:,4);                       % minute
DSec_cs = csat_only_2s_79(:,5);                         % second with decimal
u_avg_cs = csat_only_2s_79(:,6);                        % x-velocity 2 sec avg
v_avg_cs = csat_only_2s_79(:,7);                        % y-velocity 2 sec avg
w_avg_cs = csat_only_2s_79(:,8);                        % z-velocity 2 sec avg

dn = datenum(2008,1,day_cs,hour_cs,minute_cs,DSec_cs);

% calculate w_bar times c_bar for RM/Licor

w_r_avg_rm = w_avg_rm .* r_avg_rm;              % avg vertical velocity times avg H2O
conc
w_c_avg_rm = w_avg_rm .* c_avg_rm;              % avg vertical velocity times avg CO2
conc

% calculate covariances (wc_bar minus w_bar*c_bar)

wc_prime_rm = wc_avg_rm - w_c_avg_rm;           % covariance of vertical velocity and
CO2
wr_prime_rm = wr_avg_rm - w_r_avg_rm;           % covariance of vertical velocity and
H2O

% convert g/m2s to W/m2

wr_prime_rm_W = wr_prime_rm .* 2.25e3;      % times lambda, divided by 1000g/kg
```

March 20, 2008 2-sec averaged data: twosecavgtop80.m

```
% Program to load 2 second averaged data from day 80 with Licor at top

clear all
close all

% load CSAT/Licor data

load csat_only_2s_80.csv

% load RM Young data

load rm_lic_2s_80.csv

% label RM/Licor columns

record_rm = rm_lic_2s_80(:,1);                  % record number
day_rm = rm_lic_2s_80(:,2);                     % day
hour_rm = rm_lic_2s_80(:,3);                    % hour
minute_rm = rm_lic_2s_80(:,4);                  % minute
DSec_rm = rm_lic_2s_80(:,5);                    % second with decimal
u_avg_rm = rm_lic_2s_80(:,6);                   % x-velocity 2 sec avg
v_avg_rm = rm_lic_2s_80(:,7);                   % y-velocity 2 sec avg
w_avg_rm = rm_lic_2s_80(:,8);                   % z-velocity 2 sec avg
c_avg_rm = rm_lic_2s_80(:,9);                   % CO2 conc 2 sec avg
r_avg_rm = rm_lic_2s_80(:,10);                  % H2O conc 2 sec avg
wc_avg_rm = rm_lic_2s_80(:,11);                 % vertical CO2 flux 2 sec avg
wr_avg_rm = rm_lic_2s_80(:,12);                 % vertical H2O flux 2 sec avg

% Convert units for CO2 from mg/m3 to g/m3

c_avg_rm = c_avg_rm ./ 1000;
wc_avg_rm = wc_avg_rm ./ 1000;


% label CSAT columns

record_cs = csat_only_2s_80(:,1);                   % record number
day_cs = csat_only_2s_80(:,2);                      % day
hour_cs = csat_only_2s_80(:,3);                     % hour
minute_cs = csat_only_2s_80(:,4);                   % minute
DSec_cs = csat_only_2s_80(:,5);                     % second with decimal
u_avg_cs = csat_only_2s_80(:,6);                    % x-velocity 2 sec avg
v_avg_cs = csat_only_2s_80(:,7);                    % y-velocity 2 sec avg
w_avg_cs = csat_only_2s_80(:,8);                    % z-velocity 2 sec avg

dn = datenum(2008,1,day_cs,hour_cs,minute_cs,DSec_cs);

% calculate w_bar times c_bar for RM/Licor

w_r_avg_rm = w_avg_rm .* r_avg_rm;              % avg vertical velocity times avg H2O
conc
w_c_avg_rm = w_avg_rm .* c_avg_rm;              % avg vertical velocity times avg CO2
conc

% calculate covariances (wc_bar minus w_bar*c_bar)

wc_prime_rm = wc_avg_rm - w_c_avg_rm;           % covariance of vertical velocity and
CO2
wr_prime_rm = wr_avg_rm - w_r_avg_rm;           % covariance of vertical velocity and
H2O
```

March 20, 2008 high frequency (10Hz) data: high_freq_avg_5min.m

```
% Program to load high frequency data from PR eddy covariance experiment, julian day
80.

clear all;
```

```
close all;


data = load('tenHz.csv');

record = data(:,1);             % Record number
day = data(:,2);                % Day of year
hour = data(:,3);               % Hour
minute = data(:,4);             % minute
DSec = data(:,5);               % seconds, with decimal
% Ux_rm = data(:,6);            % recorded as zeros
% Uy_rm = data(:,7);            % recorded as zeros
% Uz_rm = data(:,8);            % recorded as zeros
wspeed_ec = data(:,9);             % magnitude of wind from RM Young (top)
wdirection_ec = data(:,10);        % direction of wind from RM Young, in degrees
                                     % 0 degrees is from north, 90 is from east
welevation_ec = data(:,11);        % elevation angle of wind from RM Young (degrees)
stempK_ec = data(:,12);            % temperature from RM Young, in Kelvin
stempC_ec = stempK_ec - 273.15;       % convert RM temp to Celsius
Ux_cs_ec = data(:,13);             % x-velocity from CSAT (bottom of canopy)
Uy_cs_ec = data(:,14);             % y-velocity from CSAT
Uz_cs_ec = data(:,15);             % z-velocity from CSAT
T_sonic_cs_ec = data(:,16);        % temperature from CSAT, in Celsius
co2_mg_m3_rm_ec = data(:,18);      % CO2 concentration at top of canopy
                                     % ****is this in mg/m3, or mol/m3?****
h2o_g_m3_rm_ec = data(:,19);       % water vapor conc at top of canopy
pressure_rm_ec = data(:,20);       % Licor pressure from top of canopy

dn_ec = datenum(2008,1,day,hour,minute,DSec);
numrows = 134271;

% Convert rm wdirection from 0-540 to 0-360
for k=1:numrows
    if wdirection_ec(k) > 360
        wdirection_ec(k) = wdirection_ec(k) - 360;
    end
end

% Calculate components of RM Young wind vector

Uz_rm_ec = wspeed_ec.*sind(welevation_ec);
Ux_rm_ec = wspeed_ec.*cosd(welevation_ec).*cosd(wdirection_ec);
Uy_rm_ec = wspeed_ec.*cosd(welevation_ec).*sind(wdirection_ec);

% Calculate magnitude of horizontal mean wind for CSAT

horizwind_cs_ec = (Ux_cs_ec.^2 + Uy_cs_ec.^2).^(0.5);

% Calculate magnitude of horizontal mean wind for RM Young

horizwind_rm_ec = abs(wspeed_ec .* cosd(welevation_ec));

% Calculate uncorrected azimuth for CSAT

azimuth_cs_ec = asind(-Ux_cs_ec ./ horizwind_cs_ec);

% Correct CSAT azimuth (0 degrees is from north, 90 from east - to match RMYoung)

for k=1:numrows

    if Ux_cs_ec(k) < 0 && Uy_cs_ec(k) > 0

        azimuth_cs_ec(k) = azimuth_cs_ec(k) + 90;

    elseif Ux_cs_ec(k) > 0 && Uy_cs_ec(k) > 0

        azimuth_cs_ec(k) = azimuth_cs_ec(k) + 270;

    elseif Ux_cs_ec(k) > 0 && Uy_cs_ec(k) < 0

        azimuth_cs_ec(k) = azimuth_cs_ec(k) + 360;
```

```
    elseif Ux_cs_ec(k) == 0 && Uy_cs_ec(k) > 0

        azimuth_cs_ec(k) = 180;

    end

end

% Rotate azimuths so 0 degrees is from south, 90 is from west

for k=1:numrows

    azimuth_cs_ec(k) = azimuth_cs_ec(k) + 180;
    wdirection_ec(k) = wdirection_ec(k) + 180;

    if wdirection_ec(k) > 360
        wdirection_ec(k) = wdirection_ec(k) - 360;
    end

    if azimuth_cs_ec(k) > 360
        azimuth_cs_ec(k) = azimuth_cs_ec(k) - 360;
    end

end

% Calculate instantaneous fluxes:

wr_rm_ec = Uz_rm_ec .* h2o_g_m3_rm_ec;          % moisture at top
uw_rm_ec = Uz_rm_ec .* horizwind_rm_ec;         % momentum at top
uw_cs_ec = Uz_cs_ec .* horizwind_cs_ec;         % momentum at bottom
wT_rm_ec = Uz_rm_ec .* stempC_ec;               % temperature at top
wT_cs_ec = Uz_cs_ec .* T_sonic_cs_ec;           % temperature at bottom


% Average high frequency data.
% _ecp stands for eddy-covariance processed
% _ec  stands for ec unproccessed

% if you want to average 600 points, in_ec_met = 600

in_ec_met = 3000;
n_ecp = floor(numrows/in_ec_met);

% Preallocate memory
dn_ecp = zeros(n_ecp,1);
wspeed_ecp = zeros(n_ecp,1);
wdirection_ecp = zeros(n_ecp,1);
welevation_ecp = zeros(n_ecp,1);
stempC_ecp = zeros(n_ecp,1);
Ux_cs_ecp = zeros(n_ecp,1);
Uy_cs_ecp = zeros(n_ecp,1);
Uz_cs_ecp = zeros(n_ecp,1);
T_sonic_cs_ecp = zeros(n_ecp,1);
co2_mg_m3_rm_ecp = zeros(n_ecp,1);
h2o_g_m3_rm_ecp = zeros(n_ecp,1);
pressure_rm_ecp = zeros(n_ecp,1);
Uz_rm_ecp = zeros(n_ecp,1);
Ux_rm_ecp = zeros(n_ecp,1);
Uy_rm_ecp = zeros(n_ecp,1);
horizwind_cs_ecp = zeros(n_ecp,1);
horizwind_rm_ecp = zeros(n_ecp,1);
wr_rm_ecp = zeros(n_ecp,1);
uw_rm_ecp = zeros(n_ecp,1);
uw_cs_ecp = zeros(n_ecp,1);
wT_rm_ecp = zeros(n_ecp,1);
wT_cs_ecp = zeros(n_ecp,1);
azimuth_cs_ecp = zeros(n_ecp,1);

k=1;
for i=1: n_ecp

   dn_ecp(i) = mean(dn_ec(k:k+in_ec_met-1));                    % Date vector average
```

```
   wspeed_ecp(i) = mean(wspeed_ec(k:k+in_ec_met-1));              % RM wind magnitude
   wdirection_ecp(i) = mean(wdirection_ec(k:k+in_ec_met-1));      % RM wind azimuth
   welevation_ecp(i) = mean(welevation_ec(k:k+in_ec_met-1));      % RM wind elevation
angle
   stempC_ecp(i) = mean(stempC_ec(k:k+in_ec_met-1));              % RM temp in kelvin
   Ux_cs_ecp(i) = mean(Ux_cs_ec(k:k+in_ec_met-1));                % CSAT x velocity
   Uy_cs_ecp(i) = mean(Uy_cs_ec(k:k+in_ec_met-1));                % CSAT y velocity
   Uz_cs_ecp(i) = mean(Uz_cs_ec(k:k+in_ec_met-1));                % CSAT z velocity
   T_sonic_cs_ecp(i) = mean(T_sonic_cs_ec(k:k+in_ec_met-1));      % CSAT temp in celsius
   co2_mg_m3_rm_ecp(i) = mean(co2_mg_m3_rm_ec(k:k+in_ec_met-1));    % CO2 at top
   h2o_g_m3_rm_ecp(i) = mean(h2o_g_m3_rm_ec(k:k+in_ec_met-1));      % H2O at top
   pressure_rm_ecp(i) = mean(pressure_rm_ec(k:k+in_ec_met-1));      % pressure at top
   Uz_rm_ecp(i) = mean(Uz_rm_ec(k:k+in_ec_met-1));                  % RM z velocity
   Ux_rm_ecp(i) = mean(Ux_rm_ec(k:k+in_ec_met-1));                  % RM x velocity
   Uy_rm_ecp(i) = mean(Uy_rm_ec(k:k+in_ec_met-1));                  % RM y velocity
   horizwind_rm_ecp(i) = mean(horizwind_rm_ec(k:k+in_ec_met-1));    % RM horiz velocity
mag
   horizwind_cs_ecp(i) = mean(horizwind_cs_ec(k:k+in_ec_met-1));    % CSAT horiz
velocity mag
   azimuth_cs_ecp(i) = mean(azimuth_cs_ec(k:k+in_ec_met-1));        % CSAT wind azimuth
   wr_rm_ecp(i) = mean(wr_rm_ec(k:k+in_ec_met-1));                  % RM avg of
(w*[h2o])
   uw_rm_ecp(i) = mean(uw_rm_ec(k:k+in_ec_met-1));                  % RM avg of (u*w)
   uw_cs_ecp(i) = mean(uw_cs_ec(k:k+in_ec_met-1));                  % CSAT avg of (u*w)
   wT_rm_ecp(i) = mean(wT_rm_ec(k:k+in_ec_met-1));                  % RM avg of (w*T)
   wT_cs_ecp(i) = mean(wT_cs_ec(k:k+in_ec_met-1));                  % CSAT avg of (w*T)

   k=k+in_ec_met;

end

% Calculate vertical fluxes

wr_prime_rm_ecp = wr_rm_ecp - Uz_rm_ecp .* h2o_g_m3_rm_ecp;      % RM moisture:
(w'r')bar
uw_prime_rm_ecp = uw_rm_ecp - Uz_rm_ecp .* horizwind_rm_ecp;     % RM momentum:
(u'w')bar
uw_prime_cs_ecp = uw_cs_ecp - Uz_cs_ecp .* horizwind_cs_ecp;     % CSAT momentum:
(u'w')bar
wT_prime_rm_ecp = wT_rm_ecp - Uz_rm_ecp .* stempC_ecp;           % RM heat: (w'T')bar
wT_prime_cs_ecp = wT_cs_ecp - Uz_cs_ecp .* T_sonic_cs_ecp;       % CSAT heat: (w'T')bar

% Convert h2o and heat fluxes to W/m2

wr_p_rm_ecp_W = wr_prime_rm_ecp .* 2.25e3;       % times lambda, divided by 1000g/kg
wT_p_rm_ecp_W = wT_prime_rm_ecp .* 1004;         % times rho (1kg/m3), times Cp
(1004J/kgK)
wT_p_cs_ecp_W = wT_prime_cs_ecp .* 1004;         % times rho (1kg/m3), times Cp
(1004J/kgK)

in_ec_met
int_wr_rm = sum(wr_rm_ecp .* 2.25e3 .* (in_ec_met/10))
int_wr_p_rm = sum(wr_p_rm_ecp_W .* (in_ec_met/10))
int_wT_rm = sum(wT_rm_ecp .* 1004 .* (in_ec_met/10))
int_wT_p_rm = sum(wT_p_rm_ecp_W .* (in_ec_met/10))
int_wT_cs = sum(wT_cs_ecp .* 1004 .* (in_ec_met/10))
int_wT_p_cs = sum(wT_p_cs_ecp_W .* (in_ec_met/10))
```

Meteorological data: Bisley_met.m

```
% Program to load Forest Service meteorological data from Bisley Tower

clear all

load('Bisley_10mt.csv');

year = Bisley_10mt(:,1);
day = Bisley_10mt(:,2);          % julian day
hour = Bisley_10mt(:,3);         % 4 digits, military time, no colon
Dsec = Bisley_10mt(:,4);         % seconds with one decimal place
```

```
precip = Bisley_10mt(:,5);       % precipitation (mm)
tot_rad = Bisley_10mt(:,6);      % total radiation (units? "kwatts m"-?)
tot_pfd = Bisley_10mt(:,7);      % total PFD (?) units - photons/m2s
inst_rad = Bisley_10mt(:,8);     % instantaneous radiation (units?)
instan_pfd = Bisley_10mt(:,9);   % instantaneous PFD? units?
temp = Bisley_10mt(:,10);        % degrees Celsius
RH = Bisley_10mt(:,11);          % relative humidity
av_rad = Bisley_10mt(:,12);      % average radiation (units?)
av_pfd = Bisley_10mt(:,13);      % average PFD (units?)
av_temp = Bisley_10mt(:,14);     % average temp, deg C
av_RH = Bisley_10mt(:,15);       % average rel humidity
global_rad = Bisley_10mt(:,16); % Global radiation - W/m2
ref_rad = Bisley_10mt(:,17);     % reflected radiation - W/m2
sd_rad = Bisley_10mt(:,18);      % radiation std dev?
sd_pfd = Bisley_10mt(:,19);      % PFD std dev?
sd_temp = Bisley_10mt(:,20);     % temp std dev?
sd_RH = Bisley_10mt(:,21);       % rel hum st dev?
sd_glo_rad = Bisley_10mt(:,22); % global rad st dev?
sd_ref_rad = Bisley_10mt(:,23); % ref rad st dev?
meanwind = Bisley_10mt(:,24);    % mean wind speed (m/s?)
wdirection = Bisley_10mt(:,25); % wind direction (*where is zero?)

% Convert temps to K
tempK = temp + 273.15;
av_tempK = av_temp + 273.15;

% Calculate net solar radiation
net_srad = global_rad - ref_rad;

% There are other columns in the data file that include wind std dev and
% wind histograms for ranges of degrees.  See excel file.

hour_c = floor(hour./100);
minute = hour - hour_c.*100;

dn = datenum(year,1,day,hour_c,minute,Dsec);
numrows = 1321;

esat = 0.611 .* exp(5423 .* (1/273 - 1./av_tempK));      % sat vap press (kPa)
                                                         % from Clausius Clapeyron, see
Stull(2000) p96

spechum = 0.622 .* av_RH .* esat ./ (98.*100);           % specific humidity (kg w/kg
a)
```